Master of Science Thesis

Trailing Edge Noise Simulations
using IDDES in OpenFOAM

Olivier Verhoeven

August 17, 2011

Faculty of Aerospace Engineering

Delft University of Technology

Trailing Edge Noise Simulations
using IDDES in OpenFOAM

Master of Science Thesis

For obtaining the degree of Master of Science in Aerospace Engineering
at Delft University of Technology

Olivier Verhoeven

August 17, 2011

Faculty of Aerospace Engineering · Delft University of Technology

Delft University of Technology

DELFT UNIVERSITY OF TECHNOLOGY
DEPARTMENT OF AERODYNAMICS

The undersigned hereby certify that they have read and recommend to the Faculty of Aerospace Engineering for acceptance the thesis entitled **"Trailing Edge Noise Simulations"** by **Olivier Verhoeven** in fulfillment of the requirements for the degree of **Master of Science**.

Dated: August 17, 2011

Supervisors:

Prof. dr. ir. drs. H. Bijl

dr. S.J. Hulshoff

dr. ir. A. H. van Zuijlen

ir. A. de Jong

Preface

This work is the final part of obtaining a Master's degree in the Aerodynamics department at the faculty of Aerospace Engineering at the Delft University of Technology. This report presents and demonstrates the work of my thesis study performed under the supervision of Prof. dr. ir. drs. Hester Bijl.

The research in the field of aeroacoustics is a hot topic in the industrial and academic world nowadays. Current human standards and comfort require silent machines and applications. Aeroacoustics is very interesting in a sense that it combines aerodynamics, more specifically turbulence and acoustics. Although theories exist for a long time, there is still room for improvements. Hence, with this work I hope to somehow contribute in the numerical simulation of aeroacoustics.

I wish to thank my supervisors Prof. dr. ir. drs. Hester Bijl, dr. Steven Hulshoff, Arjen de Jong and Alex Loeven for their constructive discussions and interesting ideas. Thanks to everyone else with whom I shared the basement: the collaboration and support as well as the pingpong games with my colleagues was invaluable for completing this thesis. Moreover I would like to thank my flatmate's for these incredible past six years. To my girlfriend Claire I am grateful for the many years of support and patience. Finally, to my parents, grand mother and brother: thank you to make it all possible.

Abstract

Flow induced noise is one of the major contributors in the noise generation of various industrial applications. For instance trailing edge noise is an important component of aircraft airframe noise, in particular during landing and approach. Moreover trailing edge noise is also a noise generation mechanism for wind turbine rotor blades and helicopter blades. Due to stronger regulations with respect to noise pollution, the implementation of wind turbines will tend to hamper. To ensure its further development, it is important to reduce this noise mechanism and therefore requires better modeling. Computing trailing edge noise is complex since it is inherently connected with turbulence. The trailing edge noise is caused by the interaction of turbulent structures with the trailing edge.

LES has proven to be a reliable method for the calculation of aeroacoustic problems. Although it provides sufficient accuracy and is less expensive than DNS, the higher computational cost compared to RANS makes it less attractive. A combination of sufficient accuracy and cost savings is found in the hybrid RANS-LES approaches. Herein the boundary layers are solved in full RANS mode, whereas the exterior flow is solved in LES mode. The price to pay with such models are found in the uncertainties in the transition zone between both modes. In this thesis the IDDES method was chosen to determine the aerodynamic quantities.

From the pressure fluctuations along the surface the far-field acoustics were computed with Curle's acoustic analogy and were compared with the reference data of Brooks et al. (1989).

First the NACA 0012 profile was considered under zero and seven degrees angle of attack. Acceptable results were found for the zero degrees case for which a mesh study was performed. For the seven degrees a clean and tripped configuration was considered. The clean configuration showed acceptable results whereas the tripped case found higher frequencies and a tendency towards tonal noise. In the last case, a NACA 0012 with blunt trailing edge producing tonal noise was considered. No validation concerning this case was performed.

In this thesis the ability of the hybrid approach to predict trailing edge noise was demonstrated. Although the results were encouraging validation still remains an issue. Therefore the turbulence model should be more extensively tested, with simpler cases. The influence of the transition zone on the noise production remains also unanswered.

Table of Contents

List of Figures

List of Tables

Nomenclature

Abbrevations

$SPL_{1/3}$	Sound Pressure Level in one third octave band [dB]
APE	Acoustic Perturbation Equations
BD	Backward Differencing
CAA	Computational Aeroacoustics
CFD	Computational Fluid Dynamics
CFL	Courant Number
Cl	Lift coefficient
CV	Control Volumes
DDES	Delayed Detached Eddy Simulation
DES	Detached Eddy Simulation
DILU	Diagonal incomplete-LU method
DNS	Direct Numerical Simulation
FFT	Fast Fourier Transform
FV	Finite Volume
FW-H	Fowcs-Williams Hawkings
GAMG	geometeric-algebraic multi-grid solver
GIS	Grid Induced Separation
IDDES	Improved Delayed Detached Eddy Simulation
LEE	Linearized Euler Equations
LES	Large Eddy Simulation
LLM	Log-Layer Mismatch
MSD	Modeled Stress Depletion
NS	Navier-Stokes
OASPL	Overall Sound Pressure Level
PBiCG	Preconditioned Bi-Conjugate Gradient
PCG	Preconditioned Conjugate Gradient
PISO	Pressure Implicit with Splitting of Operators
RANS	Reynolds-Averaged Navier-Stokes

S-A	Spalart-Allmaras turbulence model	
SGS	Sub-Grid-Scales	
SPL	Sound Pressure Level	dB
URANS	Unsteady Reynolds-Averaged Navier-Stokes	
WMLES	Wall Modeled Large Eddy Simulation	

Greek symbols

Δ	filter width	[m]
δ	Boundary Layer Thickness	[m]
δ_{ij}	Kronecker delta	[−]
ϵ	energy dissipation rate	$[m^2s{-}3]$
κ	von Karmann constant-]	[
λ	wavelength	[m]
μ	dynamic viscosity	$[m^2s^{-1}]$
$\nabla\tau$	viscous stress	$[Nm^2]$
ν	kinematic viscosity	$[m^2s^{-1}]$
ν_t	turbulent viscosity	$[m^2s^{-1}]$
ω	angular frequency	$[rads^{-1}]$
Φ	Shield function-]	[
ϕ	generic scalar quantity	
ρ	density	[m]
τ_{ij}^R	unresolved stress tensor	$[kg/ms^2]$
τ_w	wall shear stress	$[Nm^{-2}]$
θ	boundary layer momentum thickness	[m]
$\tilde{\nu}$	modified turbulent kinematic viscosity	$[m^2s^{-1}]$

Mathematical symbols

$\bar{\mathbf{u}}$	filtered velocity	[m]
∇	nabla operator	
l_{DES}	DES model length scale	[m]
d	Distance vector between neigbouring cells	[m]
f	body force vector	
u	velocity vector	$[ms^{-1}]$
u’	velocity fluctuations	[m]
A	Face Area Vector	$[m^2]$
e	total specific energy	$[m^2s^{-1}]$
p	pressure	$[Nm^{-2}]$
q	energy source term	
Re	Reynolds number	
t	time	[s]

Roman symbols

x	position vector of observer	[m]

$\mathbf{y}$	position vector of source	[m]
$\tilde{d}$	DES length	[m]
c_0	speed of sound	$[ms^{-1}]$
C_k	Kolmogorov constant	
d_w	wall distance	[m]
f_b	Step function (IDDES)	[-]
f_e	Elevating function (IDDES)	[-]
h_{te}	height trailing edge	[m]
I_{ac}	acoustic power density	$[Wm^{-2}]$
l_{hyb}	hybrid RANS-LES length scale	[m]
P_{ij}	surface stress tensor	$[Nm^{-2}]$
p_{ref}	reference pressure	Pa
r_e	observer distance	[dB]
t_e	retarded time	[s]
T_{ij}	Lighthill stress tensor	$[Nm^{-2}]$
u^+	non dimensionalised velocity in wall units	[-]
U_0	freestream velocity	$[ms^{-1}]$
u_τ	friction velocity	$[ms^{-1}]$
$v_i\, v_j$	velocity components	$[ms^{-1}]$
V_P	Volume Cell with centroid P	
y^+	distance in wall units	[-]
$\mathbf{n}$	Unit normal vector	[m]
$\mathbf{P}$	Cell centroid	
$\mathbf{R}$	Neighbouring Cell centroid	
$\mathbf{S}$	rate of strain tensor	$[s^{-1}]$
b	Spanwise length	[m]
c	chord length	[m]
Cd	drag coefficient	
Cf	skin friction	
Cl	lift coefficient	
Cp	pressure coefficient	
F	Face flux	$[m^3/s]$
f	frequency	$[s^{-1}]$
f	frequency	$[s^{-1}]$
k	wave number	$[m^{-1}]$
k	wavenumber	
L	Length scale of acoustic solid boundaries	[m]
M	Mach number	[-]
Q	Second invariant tensor	
r	distance between source and observer	[m]

Chapter 1

Introduction

This introduction gives an overview of a master thesis which is focused on the numerical simulation of trailing edge noise. In the first part of this introduction the various conceptual approaches are investigated. Next, the test cases are briefly addressed. Then the objective and the chosen approach will be explained and motivated. The last part provides an overview of the structure of this report.

1.1 Literature Research

During the last decades, aeroacoustics gained a lot of importance and increased its fields of industrial applications. Current human life standards require noiseless and quiet machines. Aeroacoustics is applied in various industries. Amongst them is the aerospace industry, where airframe noise - emanating from high-lift devices, landing gears and engines - is of great importance. Also reducing the noise generated by wind turbines is a hot topic nowadays. Moreover, aeroacoustics is applied in the automotive industry.

However in this thesis, the focus is on noise generated by wind turbines. Unfortunately, enough computer power is not available for the near future to carry out simulations on a full scale wind turbine. Therefore, it is important to identify and predict the most important noise sources. It is found (Oerlemans et al., 2006) that flow induced noise is the most important contributor in the noise generation mechanism of wind turbines.

1.1.1 Noise generation

Flow induced noise arises from the interaction between an airfoil blade and the turbulence produced in its own boundary layer and near wake. Flow induced noise could be tonal

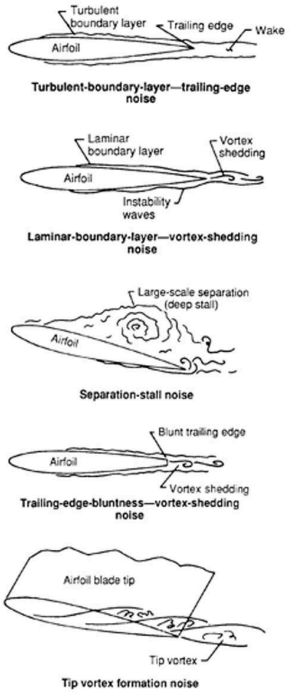

Figure 1.1: Different noise mechanisms as represented by Brooks et al. (1989)

or broadband noise in character, and may be caused by several mechanisms. According to (Brooks et al., 1989), they can be divided in five types and are correspondingly represented in Figure 1.1:

1. Turbulent boundary layer - trailing edge noise
2. Laminar boundary layer - vortex shedding noise
3. Separation-stall noise
4. Trailing edge bluntness -vortex shedding noise
5. Tip vortex shedding noise

For a wind turbine blade profile in 2D, the first, second and fourth items have the greatest influence. For a full scaled wind turbine including 3D effects, it will be necessary to include the tip vortex shedding noise.

1.1.2 Conceptual Approaches

There are various conceptual approaches to predict noise generation corresponding to the above mentioned items. A schematic overview is given in Figure 1.2 (Wagner et al., 2007).

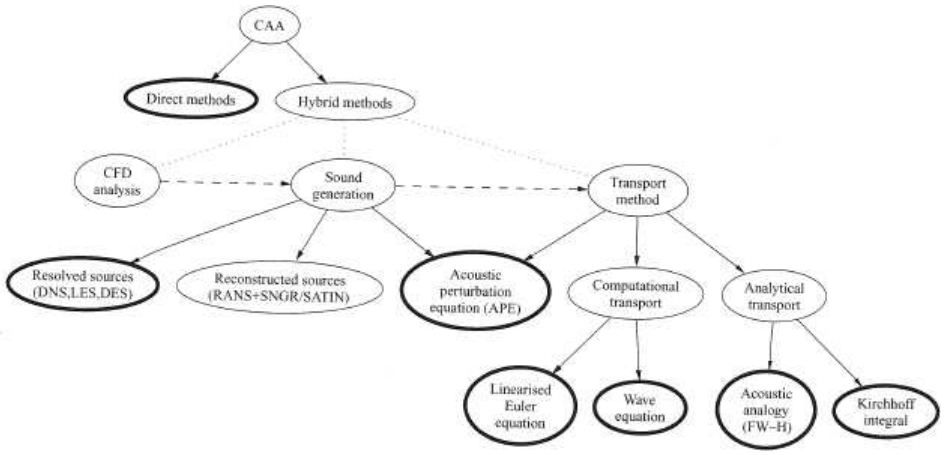

Figure 1.2: overview of conceptual approaches in computational aeroacoustics Wagner et al. (2007)

One can clearly distinguish 2 approaches:

1. Direct methods solve the acoustic problems immediately, from which the sound can be computed directly. Possible methods include a **D**irect **N**umerical **S**imulation (DNS) or a compressible **L**arge **E**ddy **S**imulation (LES). A DNS can be considered as the the most exact approach. The complete fully coupled Navier-Stokes are solved. No extra modeling is required for such a technique. However there are some drawbacks:
   (a) the high requirement on computer power (e.g. cost of DNS scales with $(Re)^3$)[-], which limits the applicability for daily use.
   (b) the inherent multi scale problem in CAA. Firstly, the perturbations in acoustics are small compared to other aerodynamic quantities. Secondly, the difference in the speed of sound propagation and fluid propagation is very large for flows in the low Mach regime.
2. Hybrid methods: Decoupling of the sound generation and the acoustic sound propagation. The sound sources are identified by:
   (a) some classical CFD method, which can resolve the noise sources. These methods can be incompressible LES/DNS and compressible LES/DNS.
   (b) a CFD method, in which the sources are reconstructed. In this branch, the mean turbulent quantities are provided by RANS. Recently, methods have been devised to synthesize a turbulence field based on these time-averaged turbulence quantities. In a further process, this information is subsequently used as the source terms in a separate acoustic prediction method. Of course, this process depends heavily on the soundness of the empirics and the validation data used to calibrate them.
   (c) LES method in combination with the acoustic perturbation equations (APE) proposed by Ewert and Schroder (2004). The APE is a special variant of the LEE, which is discussed below. LES is used to resolve the unsteady flow problem in the hydrodynamic near field and subsequently applying an acoustic analogy based

on linear acoustic perturbation equations (APE) to determine the related sound radiation toward the farfield. The acoustic simulation based on APE considers mean-flow convection and refraction effects of a nonuniform mean flow such that the computational domain of the LES has to comprise only the significant acoustic source region in the immediate vicinity of the trailing edge. A detrimental effect of such an approach is the requirement of extra computer power.

In aeroacoustics one is also interested in the sound propagation to the farfield, which is the second branch of the hybrid method. Therefore, the sound sources need to be transported. Techniques are:

(a) Based on an analytical approach. An integral formulation of the source terms along a surface or within a volume are used.

(b) A more complex approach is based on a numerical solution of the linearized Euler transport equation (LEE) or a wave equation. Additional complexity arises in differences in boundary formulations between CFD and acoustic domain, discretizations and resolution.

Interim conclusion

It already becomes clear that a few techniques are not suitable for this research and will therefore not be treated further.

- Due to the multiscale problems and stringent demand on computer power, the direct method is not convenient.
- Hybrid method provides a good alternative.
- Semi-empirical is not flexible and requires calibration. Industry requires flexibility and reliability.
- The APE and LEE are in principle good candidates. They are accurate and can be applied to a variety of cases. However additional computer power and extra complexity in the implementation make these approaches less interesting for this thesis.
- The coupling between the classical CFD techniques and the integral information offers the best trade-off. This method is relatively fast compared to other methods and has proven to be reliable for similar test cases.

1.1.3 Numerical Methods

In the previous part it is suggested to use a hybrid method. This approach needs some CFD method to provide the noise sources. The numerical methods, with their advantages and drawbacks and their applicability for aeroacoustics will be discussed here. The numerical methods are sorted by their level of detail in the solution, starting with the lowest level.

(Unsteady) Reynolds Navier Stokes (URANS)

The RANS method is the outcome of the classical averaging of the Navier-Stokes equations. The RANS method is characterized by the turbulence closure models to model the turbulent fluctuations. For the application in aeroacoustics, this method has some shortcomings. The turbulence models must model a large set of scales. Detailed informations about the small fluctuations are often required in aeroacoustics. However as already was mentioned, it is possible to reconstruct noise sources or recreate the stochastic turbulence field from a RANS. This technique uses a model to synthesize a turbulence field based on these time-averaged turbulence quantities(Bechara et al. (1994)). There has been a number of model turbulence spectrums developed over the years from experimental velocity correlations. These model spectra use the turbulence length scales calculated by the RANS model. Once the spectral information has been assumed, a deconvolution procedure is used to synthesize the transient velocity field at each point required by the noise prediction model.

Hybrid RANS-LES method

The hybrid method is a blending between the statistical RANS and LES method, which will be discussed below. The method is developed to overcome the excessive computer demands of LES, and in the meanwhile to increase the accuracy of RANS. The basic principle here is to solve the boundary layer with RANS, whereas LES is used for the external flow and separation regions.

Large Eddy Simulation (LES)

LES is used to resolve the majority of the full range of turbulent scales. LES resolves directly all the large scales, which contain the most energy and contribute most to the transport of properties. The small scales, or eddies behave in a universal way, and are simply modeled. Resolving most of the eddies, consequently requires a lot of computer power.

Interim Conclusion

- RANS is not capable to capture the small unsteady fluctuations which are essential for aeroacoustics. Hence, one should apply synthetic turbulence to generate or account for the acoustic noise sources.
- LES is accurate and proven to be reliable, but it is rather computationally expensive.
- The hybrid RANS-LES method can capture the most important fluctuations, although it is less accurate as LES, but faster.
- Note that the DNS method was not discussed anymore. Reasons are addressed before.

1.1.4 Farfield propagation methods

In the hybrid methods, the flow and acoustic field are computed separately. The flow data obtained by a CFD method can be used to solve the acoustics and provide the farfield propagation. It was shown that many methods are possible. Due to the complexity of some methods, this thesis is restricted to the integral formulations, or acoustic analogies. One can distinguish roughly three types of integral formulations, sorted according to complexity:

1. Lighthill: is the most general formulation and is derived from the exact Navier-Stokes equations. This form requires that the source may not be located at the boundary of the computational domain, as stated by Lighthill, M.J. (1952). The objective is to investigate trailing edge noise, implying sources close to the profile. This makes the integral not suitable.
2. Curle's formulation: takes the presence of walls into account. And is therefore a generalization of Lighthill as given in Curle, N. (1955). Besides the noise sources throughout the volume, it also considers the sources at the surface/profile.
3. An even more complete formulation is given by Ffowcs Williams and Hawkings (1969). In addition to the surface and volume sources, it also reckons for the movement of the surface. This is very interesting and inevitable for dealing with rotating blades or wind turbine blades.

Interim conclusion

- Scattering from the surface or pressure fluctuations along the surface should be included.
- Curle is a simple an reliable formulation and can give a fast and quick idea.
- Ffowcs Williams and Hawkings is the most general and reliable.

1.2 Introduction to the test cases

In this thesis one will consider some general test cases which are representative and are challenging for noise predictions. The test cases were chosen in such a way that validation with respect to the acoustics was possible. For these cases the benchmark of Brooks et al. (1989) was used as reference data. This database provides data of noise production of a classical NACA 0012 with different chord lengths and subjected to various flow conditions. The noise in this reference is found to be broadband and tonal in character. The broadband noise corresponds to profiles with sharp trailing edges, whereas tonal noise was observed for blunt trailing edges. Some test cases were chosen to identify the ability of the approach, presented in this thesis, to reproduce this noise.

Following conditions were used for all the simulations considered:

- a symmetric NACA0012 is chosen to be the test airfoil
- a freestream velocity of $70m/s$ is considered
- a Reynolds number of 1 million is chosen

For the first case no incidence angle was chosen. This case was challenging to see whether the turbulence model was able to capture all boundary characteristics properly. In the second case, the airfoil was put under seven degrees angle of attack. Here, the ability to simulate separation was tested. For the seven degrees case, the airfoil was both clean and tripped at 25% of the chord. In this case the noise spectrum is expected to be broadband. The last case was a NACA 0012 airfoil with a blunt trailing edge, which was expected to generate tonal noise. No incidence anlge was selected for this case.

1.3 Research Objective and Approach

The goal of this thesis is to simulate the noise emanating from an airfoil. It is known that the trailing edge contributes most to the noise generation. Additionally the effect of a blunt trailing edge on the noise production should be quantified.

In the previous sections of this chapter, some different conceptual approaches were already addressed. It was suggested that the hybrid formulation, where the flow and acoustics are solved separately, could be an appropriate tool to reach the objectives. Therefore, following items are inevitable for completing this study and are discussed in depth in the remainder of this thesis:

- A turbulence model has to be chosen, in order to provide enough detail.
- Select numerical tool, which can simulate the unsteady, turbulent incompressible flow.
- A good test case has to be build. Therefore a mesh, which fulfills the turbulence model requirements and computer resources is necessary.
- Setting up a good test case. Select suitable boundary conditions, solver settings and accurate discretization schemes.
- A validation of the results is essential. This validation is twofold. Both the aerodynamic flow variables and acoustics should be validated. Do the various test cases show comparable results as in literature?

1.4 Outline

The general outline of this thesis will be given now. This first chapter presented an overall introduction into the state of the art in computational aeroacoustics. Chapter 2 discusses

the general approach for turbulence modeling. A detailed description of the hybrid RANS-LES model is given. Chapter 3 is devoted to the CFD software and some basic principles to solve the governing equations. Chapter 4 discusses the computational aeroacoustic methods. Validation and verification for a flat plate and the NACA 0012 with zero incidence angle are considered in chapter 5. Results for the NACA 0012 with seven degrees angle of attack and airfoil with blunt trailing edge are considered in chapter 6. The report is completed with the conclusions and recommendations.

Chapter 2

Physics and Modeling

Nowadays in industry, wall bounded flows are modeled with classical RANS models. However when detailed characteristics of the flow are required, such as in aeroacoustics, these models provide limited accuracy. On the other hand, DNS and LES which are capable of facing these problems, are still computationally expensive for high Reynolds numbers and not possible for the near future. These issues are tackled with the development of hybrid RANS-LES. This chapter provides more insight in the applied numerical method and the implementation of a turbulence model. The first part of this chapter discusses the way the fluid dynamics are incorporated. The second part focuses on the way the hybrid RANS-LES method is applied.

2.1 Governing flow equation

The objective of this thesis is to simulate the trailing edge noise, induced by some external flow. Since these flows are typically in the low Mach range and subjected to Newtonian fluid properties, the Navier-Stokes equations can be assumed as the governing equations describing the fluid dynamics. The Navier-Stokes equations consist of five equations. One equation describes the conservation of mass (2.1a, three equations (2.1b) describe the conservation of momentum (1 for each direction) and one formulates the conservation of energy.

$$\frac{D\rho}{Dt} = \frac{\partial \rho}{\partial t} + \nabla \cdot \rho \mathbf{u} = 0 \tag{2.1a}$$

$$\frac{D\rho \mathbf{u}}{Dt} = \frac{\partial \rho \mathbf{u}}{\partial t} + \nabla \cdot (\rho \mathbf{u}\mathbf{u}) = -\nabla p + \nabla \cdot (\mu \nabla \mathbf{u}) + \mathbf{f} \tag{2.1b}$$

$$\frac{D\rho\ e}{Dt} = \frac{\partial \rho e}{\partial t} + \nabla \cdot (\rho \mathbf{u} e) = -\nabla p \mathbf{u} + \nabla \cdot (\mu \mathbf{u} \nabla \mathbf{u}) - \nabla q \tag{2.1c}$$

where $D/Dt = \partial/\partial t + \mathbf{u}\nabla$ is known as the material derivative. Furthermore p, ρ, e are the pressure, density and total specific energy. The velocity components are incorporated in $\mathbf{u}$. The symbol ∇ refers to the Nabla operator which is defined as:

$$\nabla = \left(\frac{\partial}{\partial x}, \frac{\partial}{\partial y}, \frac{\partial}{\partial z} \right) \tag{2.2}$$

According to the low Mach regime, one can consider the flow as incompressible, resulting in a constant, homogeneous density through the domain. The assumption of the absence of external forces, such as gravity and body forces, result in a simpler form of the Navier-Stokes equations. Moreover it is not expected that the temperature will have influence on the flow field dynamics. Hence, only four unknown quantities remain (velocity components and pressure), since one can simply omit the energy equation of 2.1c , resulting in:

$$\nabla \cdot \mathbf{u} = 0 \tag{2.3a}$$

$$\frac{\partial \mathbf{u}}{\partial t} + \nabla \cdot (\mathbf{u}\mathbf{u}) = -\frac{\nabla p}{\rho} + \nabla \cdot (\nu \nabla \mathbf{u}) \tag{2.3b}$$

The last term in equation 2.3b corresponds to the viscous stress $\nabla\tau$.

2.2 Numerical methods and turbulence

Aeroacoustic engineering is inherent connected with the existence of turbulence. Turbulence appears in enormous amount of industrial applications. There are various ways of computing the different scales which exist in turbulence. As already was mentioned in section 1.1.3, there is a technique which provides an 'exact' solution of the NS equation. Such a technique represents all the scales in turbulence. No additional modeling is required. This was called the **D**irect **N**umerical **S**imulation (DNS). Unfortunately, it had some limitations, which were already addressed (see section 1.1.3). A second method was **L**arge **E**ddy **S**imulation (LES). LES computes the most important large scales and models the smallest scales. The **R**eynolds **A**veraged **N**avier **S**tokes are used to model a very wide range of the the turbulent scales. In this thesis, a hybrid RANS-LES method will be used. This method combines the advantages of both RANS and LES. First some general principles of LES are discussed.

2.2.1 LES principles

The basic theory and idea of LES was formulated by Smagorinsky, J. (1963). According to the theory of Kolmogorov, the large scales, which contain the most of the energy and do most of the transporting, are the most important ones and are calculated directly. The smallest scales, which are assumed to behave uniformly are easily modeled. This is in a nutshell the basic principle of LES. Otherwise stated, this means that the larger scales contain the majority of the energy, whereas the smaller scales only contribute a fraction of the total energy. This can be illustrated by the turbulent energy spectrum or the energy cascade, shown in Figure 2.1. For convenience the Kolmogorov's law, indicated by the straight line is also included and is defined as:

$$E(k) = C_k \epsilon^{2/3} k^{-5/3} \tag{2.4}$$

where C_k is a constant around 1.5, ϵ the energy dissipation rate and k the wavenumber (proportional to the inverse of the length scale). A energy spectrum can roughly be divided in three subregions:

1. The first region is characterized by the larger eddies which contain the most energy and are provided by the integral length scales, denoted by the wavenumber k_i.
2. The second region contains the eddies which follow the Kolmogorov's law and this region is known as the inertial subrange. The region is dominated by the transitive scales and as such transfer energy from the large to the small scales.
3. The last region is the dissipative range and contain the very small scales. The behaviour of the eddies is dominated by the viscosity and energy transfer from the larger scales. It can be assumed that they do not depend on the larger scales and therefore do not aware from the geometric boundaries.

In Figure 2.1, the cutoff wavenumber K_c is the scale separation between the larger and smaller scales. This separation will be explained in next section. Note that the representation of the energy spectrum is in fact an idealization. In the real world the energy spectrum can be more complex.

LES filter

Like in RANS, where some averaging is performed to elucidate the large scales, one applies a filter in LES. The filtering is used to perform a scale separation. This is a locally derived weighted average of the flow properties over a volume of a fluid. An important feature of the filter process is the filter width Δ. The turbulent length scales larger as Δ are retained in the flow field, whereas the smaller scales, the **S**ub-**G**rid **S**cales (SGS) should be modeled. The idea is that one can write any flow variable, e.g. velocity, as a contribution of the large and small scales:

$$\bar{\mathbf{u}} = \mathbf{u} - \mathbf{u}' \tag{2.5}$$

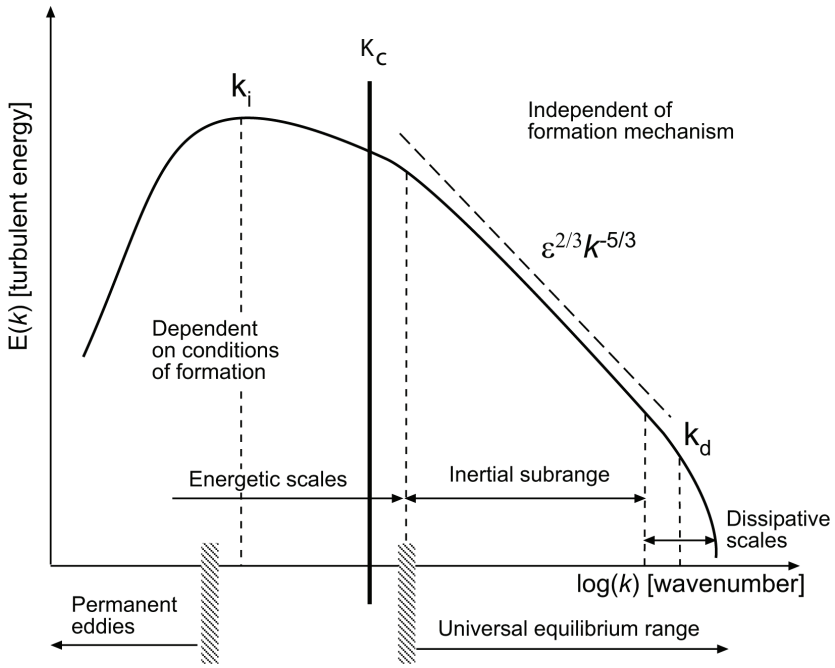

Figure 2.1: The energy spectrum subdivided in 3 regions. A energy-containing part, a region which transfers the energy to the smaller scales and the dissipation region (de Villiers (2006)).

The overbar refers to the larger, resolved scales, whereas the prime corresponds to the smaller scales. The filtering process to obtain the larger scales is defined as:

$$\bar{\mathbf{u}} = \oint \mathbf{u}(x')G(x, x'; \Delta)dx' \tag{2.6}$$

where the filter function $G(x, x', \Delta)$ should satisfy following condition;

$$\oint G(x, x'; \Delta)dx' = 1 \tag{2.7}$$

Figure 2.2 is a schematic one-dimensional representation of the filtering operation of a flow variable. The standard filter, applied in OpenFOAM is the implicit top-hat filter. This filter is simply defined as the average over a rectangular region. This filter is often applied in finite volume methods. If the grid-spacing is chosen to be the filter width, the averaged and the local value of $\bar{\mathbf{u}}$ will be equal. The top-hat filter function is given as:

$$G(x, \Delta) = \begin{cases} \frac{1}{\Delta}, & \text{if } |x'| \leq \frac{\Delta}{2} \\ 0, & \text{otherwise} \end{cases} \tag{2.8}$$

Figure 2.3 is an illustration of a top-hat filter with a filter width of 0.06. Some other filter operations, such as the Gaussian filter or the sharp hat filter exist, but are not treated further.

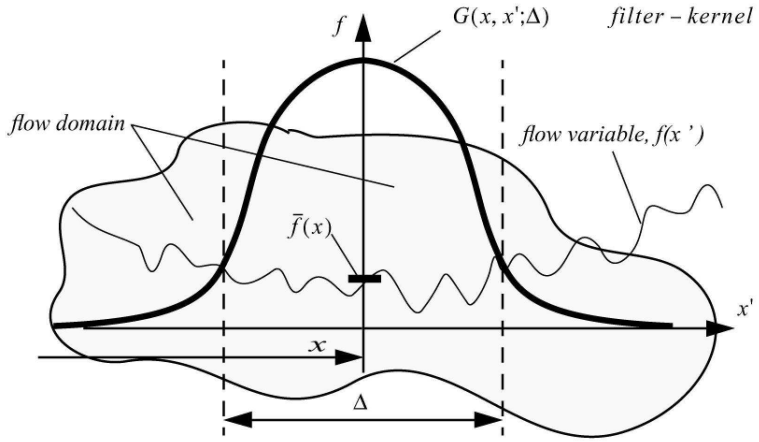

Figure 2.2: A representation of an arbitrary filter function of a flow variable.

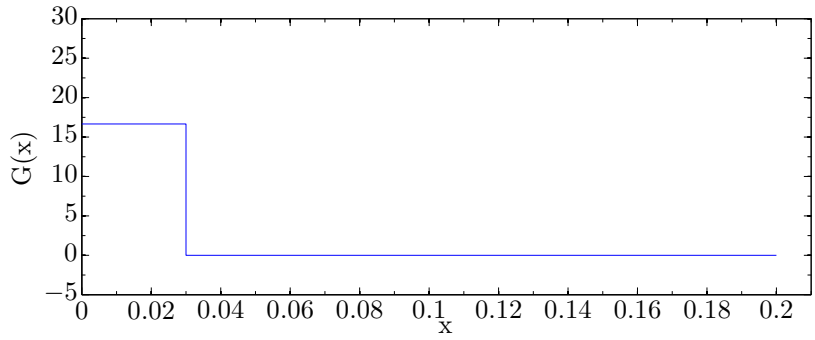

Figure 2.3: top-hat filter

For the interested reader, some additional information about the filter operations can be found in Davidson (2007).

2.2.2 Filtered Navier-Stokes equation

If the filter is applied to the incompressible Navier-Stokes equations 2.3b, one obtains the equations of motion, in terms of the resolved large scales, denoted by the overbar $\bar{\cdot}$:

$$\frac{\partial \bar{u}_i}{\partial x_i} = 0 \tag{2.9a}$$

$$\frac{\partial \bar{u}_i}{\partial t} + \frac{\partial}{\partial x_j}(\bar{u}_i \bar{u}_j) = -\frac{1}{\rho}\frac{\partial \bar{p}}{\partial x_i} + \frac{1}{\rho}\frac{\partial \tau_{ij}^R}{\partial x_j} + \nu \nabla^2 \bar{u}_i \tag{2.9b}$$

The non-linear convection term in NS causes a dependency between the resolved and unresolved scales. The influence of the unresolved scales are incorporated in the subgrid-stress

tensor, which includes the residual stresses. This is defined as:

$$\tau_{ij}^R = \rho(\overline{u_i u_j} - \overline{u}_i \overline{u}_j) \tag{2.10}$$

An Eddy-viscosity model is used to define the unresolved scales in LES. Therefore, the stress tensor can be written as:

$$\tau_{ij}^R = 2\rho\nu_t \overline{S}_{ij} + \frac{1}{3}\delta_{ij}\tau_{kk}^R, \tag{2.11}$$

where ν_t is the eddy or turbulent viscosity. This yields,

$$\frac{\partial \overline{u}_i}{\partial t} + \frac{\partial}{\partial x_j}(\overline{u}_i \overline{u}_j) = -\frac{1}{\rho}\frac{\partial \overline{p}}{\partial x_i} + 2\frac{\partial}{\partial x_j}[(\nu + \nu_t)\overline{S}_{ij}] \tag{2.12}$$

A last step is to describe the ν_R. A definition of the Eddy-viscosity will be given in following section.

2.3 Choosing the turbulence closure model

To determine the eddy viscosity (ν_t), the Spalart-Allmaras (S-A) model is used. This is a relative simple model, since it only uses one additional equation. Therefore, only one additional unknown variable is introduced, the modified turbulent kinematic viscosity $\tilde{\nu}$. The turbulent eddy viscosity as defined in (Spalart et al., 2006)is:

$$\nu_t = \tilde{\nu} f_{v1} \quad \text{with } f_{v1} = \frac{\chi^3}{\chi^3 + c_{v1}^3} \quad \text{and } \chi = \frac{\tilde{\nu}}{\nu} \tag{2.13}$$

Here, c_{v1} is a constant and ν represents the molecular viscosity, whereas $\tilde{\nu}$ is the working variable, which satisfies the transport equation given by

$$\frac{D\tilde{\nu}}{Dt} = c_{b1}\tilde{S}\tilde{\nu} + \frac{1}{c_\sigma}\left[\nabla \cdot ((\nu + \tilde{\nu})\nabla\tilde{\nu}) + c_{b2}(\nabla\tilde{\nu})^2\right] - c_{w1} f_w [\frac{\tilde{\nu}}{\tilde{d}}]^2 \tag{2.14}$$

$$\tilde{S} = \omega + \frac{\tilde{\nu}}{\kappa^2 \tilde{d}} f_{v2} \tag{2.15}$$

$$f_{v2} = 1 - \frac{\chi}{1 + \chi f_{v1}} \tag{2.16}$$

The quantity ω corresponds to the magnitude of the vorticity and the function f_w is defined as

$$f_w = g[\frac{1 + c_{w3}^6}{g^6 + c_{w3}^6}]^{1/6}, \tag{2.17}$$

$$g = r + c_{w2}(r^6 - r), \tag{2.18}$$

$$r = \frac{\tilde{\nu}}{\tilde{S}\kappa^2 \tilde{d}^2}. \tag{2.19}$$

The set of constants are listed in Table 2.1.

$c_{b1} = 0.135$	$c_\sigma = 2/3$
$c_{b2} = 0.622$	$\kappa = 0.41$
$c_{w2} = 0.3$	$c_{w3} = 2$
$c_{v1} = 7.1$	$c_{w1} = c_{b1}/\kappa^2 + (1 + c_{b2})/c_\sigma$

Table 2.1: List of constants corresponding to Spalart-Allmaras closure model.

2.4 Hybrid RANS-LES models

Hybrid techniques, typically make use of the solution of another set of model equations in a region near the wall. In zonal hybrid methods a region in the vicinity of the wall is defined where the turbulent boundary layer is solved. Communication to the outer LES region is prescribed by explicit boundary conditions. On the other hand, in blended hybrid methods a smooth transitions is made between different regions.

The most common type of a hybrid RANS-LES is DES (Detached Eddy Simulation) which was first proposed by (Spalart and Allmaras, 1992). The general idea behind these types of models is to combine the advantages of both RANS and LES. More precisely, the model acts as a RANS model in attached boundary layers and turns into LES for the separated flow regions. For these blended hybrid methods, a smooth transition is made from regions where the unsteady Reynolds-averaged equations are solved to those where a standard LES is performed. The switching between two models depends on the local grid-resolution. However these blended approaches, like DES suffer from transition layers resulting from their interface treatment and as a result decrease the skin friction as was shown in Piomelli et al. (2003). An overview of DES and DDES (Delayed Detached Eddy Simulation) and the issues encountered with these models will be addressed in this section. A possible solution to overcome these problems is provided in next section 2.5.

2.4.1 Classical Detached Eddy Simulation (DES)

The original DES combines the standard Spalart-Allmaras RANS model with its Sub-Grid Scale (SGS) counterpart by means of a limiter which is defined by:

$$l_{DES} = \min\{d_w, C_{DES}\Delta\}, \tag{2.20}$$

where l_{DES} is the model length scale, d_w is the distance to the wall involved in the destructive term of the S-A model, $C_{DES} = 0.65$ an empirical derived constant and Δ which is defined as the largest local grid-spacing:

$$\Delta = \max\{\Delta_x, \Delta_y, \Delta_z\} \tag{2.21}$$

The DES model acts as a classical S-A RANS background model in the attached boundary layer near the wall (at $d_w < C_{DES}\Delta$) and as a SGS model with the filter $C_{DES}\Delta$ in the separation region, which is generally away from the wall (at $d_w > C_{DES}\Delta$).

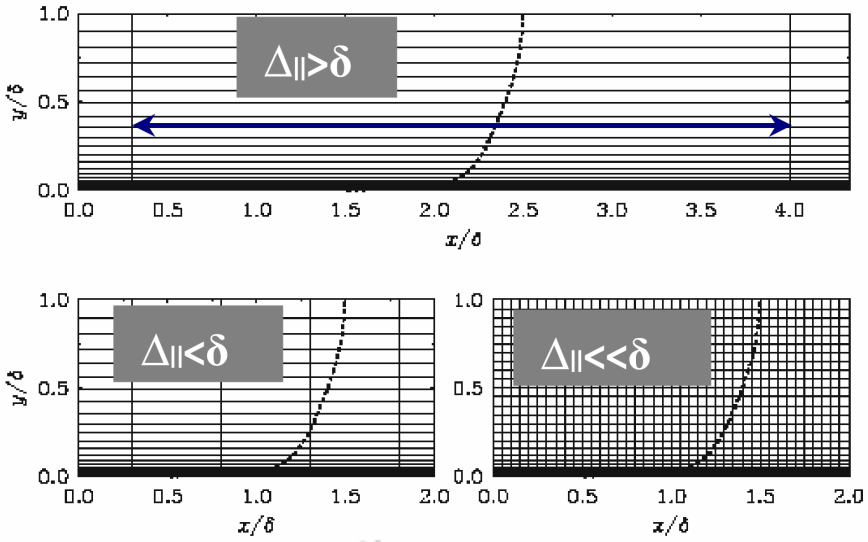

Figure 2.4: Different mesh designs as can be encountered during grid refinement. The first has a spacing larger as the boundary layer. The second mesh has a smaller spacing than the boundary layer, but is too coarse to support LES content. The last mesh is a LES grid.

Although this turbulence model is very promising, it still encounters some drawbacks. Problems arise when the wall bounded flows have thick boundary layers and small separation regions. In this case, the grid spacing parallel to the wall $\Delta_{||}$ often becomes less than the boundary layer thickness. The grid spacing is then fine enough for the DES length-scale to follow the LES branch in accordance with (2.20). And as a consequence it will lower the eddy viscosity below the RANS level, but the resolved Reynolds stresses, or the LES content, deriving from the velocity fluctuations have not replaced the modeled Reynolds stresses. These 'missing' stresses reduce the skin friction. This phenomena is called Grid Induced Separation (GIS) in literature (Spalart and Allmaras, 1992; Spalart, 2009).

To give a clear overview of the importance of the grid, Figure 2.4 presents some basic grid design.

The first part of Figure 2.4 shows a wall-parallel spacing $\Delta_{||}$ which exceeds the boundary layer thickness δ. Therefore the DES length-scale will be of the RANS type ($l_{DES} = d_w$) throughout the boundary layer. The last type in Figure 2.4 shows a grid with all spacings smaller as δ. Consequently, this can be seen as a classical 'pure' LES grid. The sub grid scale model will be activated ($l_{DES} = C_{DES}\Delta$) in the majority of the boundary layer. A RANS model will only be used in the vicinity of the wall ($l_{DES} = d_w$). For the second grid, the spacings are not as small as the pure LES grid. Therefore the SGS model of the DES will originate deep in the boundary layer. At this point, the grid is not fine enough to capture all the velocity fluctuations. Moreover the eddy viscosity will be reduced, as well as the modeled Reynolds stresses, without the introduction of resolved stresses to restore the balance. This

phenomena is called Modeled Stress Depletion (MSD) in literature (Spalart and Allmaras, 1992).

2.4.2 Delayed Detached Eddy simulation (DDES)

The Delayed Detached eddy simulation (DDES) was formulated in order to avoid the appearance of the MSD which arises for the ambiguous grids like the second grid in Figure 2.4. The DDES is a simple modification of the classical DES of Spalart and Allmaras (1992). This model is similar to a proposal of Menter et al. (2003) for the shear-stress transport model. The key point is that it uses some blending functions (see section 2.5 on IDDES) to define the length scale. DDES detects boundary layers and maintains the full RANS mode, even if the grid spacing would have activated the DES limiter. This detection mechanism depends on the eddy viscosity and therefore on the solution as well. Simply stated as in (Haase, 2009), if such blending functions indicate that a point is inside the boundary layer, it refuses to transfer to LES mode. As a consequence, the transition between RANS and LES will be more abruptly. The DDES was designed to eliminate the odd reaction of the DES to a grid refinement beyond the limit of MSD or GIS.

The blending functions $F1$ and $F2$ of Menter et al. (2003) make use of the internal length scale of the RANS model and the wall distance. These 'shielding' functions are usually 1 in the boundary layer and fall rapidly to 0 at the edge of the boundary layer. In the S-A model (one equation model), the internal length scales is not available. Hence, a parameter r is used, which is the ratio (squared) of a model length-scale to the wall-distance. For the S-A model, the parameter is defined as:

$$r_d = \frac{\nu_t + \nu}{\max\left[\sqrt{U_{i,j}U_{i,j}}, 10^{-10}\right] \cdot \kappa^2 d_w^2} \tag{2.22}$$

where $U_{i,j}$ are the velocity gradients, κ the von Karman constant and d_w the wall distance. This parameter will be equal to 1 in the logarithmic layer and fall rapidly to zero at the edge. Following function, given by:

$$f_d = 1 - \tanh(8r_d)^3 \tag{2.23}$$

will be 1 in the LES region ($r_d << 1$) and 0 elsewhere. Furthermore, a new definition of the DES length scale given in equation 2.20 is restated by:

$$l_{DES} = d_w - f_d \max\left(0, d_w - C_{DES}\Delta\right) \tag{2.24}$$

In contrast to the old length scale, given by equation 2.20 where only grid dependency was taken into account, the modified length scale of equation 2.24 also depends on the eddy-viscosity field. With this modification of l_{DES}, it is possible to refuse the LES mode, if the function f_d indicates that the point is well inside the boundary layer based on the value of r_d.

2.5 Improved Delayed Detached Eddy simulation (IDDES)

Another turbulence model is the Improved Delayed Detached Eddy simulation IDDES. The objective of this model is to combine the advantages of the wall modeled LES (WMLES), and the DDES capabilities. The wall modeled LES was a different approach to overcome the excessive need of resolution typically required for a classical LES of turbulent boundary layers. For instance the wall-stress model proposed by Schumann (1975), considered the first off-wall points in the logarithmic layer and used empirical derived wall functions together with velocities to calculate an estimate for wall stresses at the boundary.

On the other hand, it is also possible to use the DES for these WMLES as was attempted by Nikitin et al. (2000) and was successful. The problem of such WMLES was mostly found in the log-layer mismatch (LLM), between the RANS and LES regime. In fact, the simulation provided two logarithmic layers: the inner layer provided by the RANS model and an outer layer, which appears when all local grid-sizes are smaller than the distance to the wall. An under-prediction of about $15 - 20\%$ was noticed as a result of a mismatch between the inner and outer layer. Nevertheless, the WMLES proved to save computing time over LES. The IDDES was developed to avoid the LLM and provide a single set of formulas for both natural DES applications and their WMLES uses. In this way, the model can be used for different flow or different regions inside a single simulation over a complex geometry. Following discussion provides a global idea how the method works, and is based on the works of (Spalart and Allmaras, 1992; Haase, 2009; Greschner et al., 2010; Shur et al., 2008). Four aspects are adressed in this overview of the formulation of the IDDES model:

1. Modification of the Subgrid length-scale
2. The DDES branch of of IDDES
3. WMLES branch of the IDDES
4. Hybridization of DDES and WMLES

2.5.1 Subgrid length-scale

In literature, the most applied definition of the sub-grid length scale for a classical LES, is based on the cube root of a cell volume which is defined as:

$$\Delta = \sqrt{(\Delta x)^2 + (\Delta y)^2 + (\Delta z)^2}, \tag{2.25}$$

Furthermore, the choice of the sub-grid length scale for the simple DES (see 2.4.1) was based on the maximum of the three cell dimensions 2.21. Difficulties are found with both definitions of sub-grid scale length. More explicitly in the value of the SGS constants, which should have different values for different flow regions such as wall-bounded flows or free turbulent flows (Decaying Isotropic Homogeneous Turbulence). Therefore a new formulation was established to avoid the need of different SGS constants for wall-bounded flows and free turbulent flows.

A new idea for the new formulation of the sub-grid scale length is to include some wall-distance dependency, which yields:

$$\Delta = f(\Delta_x, \Delta_y, \Delta_z, d_w) \tag{2.26}$$

In equation 2.26, there is a dependency on the local cell sizes and the distance to the wall d_w. The computational domain can be divided in three subdomains. Firstly, away from the wall, the grid is mostly isotropic and is set like for the classical DES equal to the maximum local grid spacing.

$$\Delta_{free} = \Delta_{max} \equiv \max(\Delta_x, \Delta_y, \Delta_z) \tag{2.27}$$

Secondly, for the region close to the wall, the subgrid length scale should not follow the decrease of the wall-normal step. In this region the subgrid length scale is defined by the wall-parallel grid only:

$$\Delta_{wall} = const(d_w) = f(\Delta_x, \Delta_z) \tag{2.28}$$

Thirdly, the sub-grid length scale for the region between the above limiting cases is assumed to behave as a linear function of d_w. Moreover it is assumed that Δ varies within the range $\Delta_{min} \leq \Delta \leq \Delta_{max}$.

All those three statements can be captured in one single expressions:

$$\Delta = \min\left\{\max\left[C_w d_w, C_w \Delta_{max}, \Delta_{wn}\right], \Delta_{max}\right\}. \tag{2.29}$$

In equation 2.29, Δ_{wn} is the grid step in the wall-normal direction and C_w is a constant equal to 0.15 based on a LES of a developed channel flow. Figure 2.5 presents a typical variation of the sub-grid scale length across a channel flow.

The solid line in Figure 2.5 occurs when $\Delta \leq C_w d_w$ is valid. Moreover the value of Δ remains constant as long as $d_w \leq \Delta_{max}$. At this point the value of the sub-grid length scale Δ is equal to $C_w \Delta_{max}$. When the distance to the wall becomes larger as the maximum cell size dimension, $d_w > \Delta_{max}$ the SGS length grows linearly with $\Delta = C_w d_w$. Once the value Δ_{max} is reached, the SGS length remains at this value. The dashed line is typical for a strong wall-normal stretching. Near the wall the value of the SGS length is constant $C_w \Delta_{max}$. Once $\Delta_{wn} > C_w \Delta_{max}$ the SGS length grows linearly until Δ_{max} is reached. From Figure 2.5 it is clear that the rate is larger as in the first case. Since this last behaviour is undesirable for simulations, an acceptable rate of growth of the wall-normal step should be aimed for.

Compared to other SGS models, the IDDES approach uses a more complex formulation of evaluating the grid filter. Besides the cell dimensions, the wall normal distance and the height of the cell in wall normal direction have their influence in the determination of the grid filter.

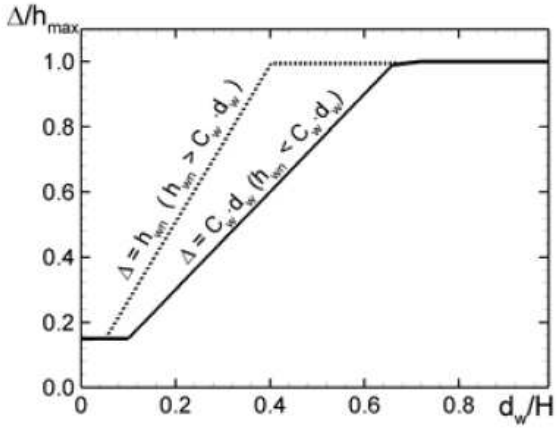

Figure 2.5: Variation of the sub-grid length scale across a plane channel

2.5.2 The DDES branch of IDDES

The first branch corresponds to DDES and is only activated when the inflow conditions do not have turbulent content. The DDES length scale was already reported in 2.24, but is repeated for convenience.

$$l_{DDES} = l_{RANS} - f_d \max\left(0, l_{RANS} - l_{LES}\right) \tag{2.30}$$

with $l_{LES} = C_{DES}\Psi\Delta$ and $l_{RANS} = d_w$. An expression for the delaying function was given in equation 2.23. There appears an additional factor Ψ compared too the classical length scale of DES. The reason for the introduction of this factor is because in the LES mode of DES, the subgrid eddy viscosity decreases with grid refinement and decrease of flow Reynolds number. At some point the DES will mis-interpret and act as like in the vicinity of a wall. As a consequence, the eddy viscosity will drop relative to the ambient velocity and length scales through f_v and f_t functions which corresponds to the S-A model.

For the S-A model the function depends on the ratio of the eddy viscosity and the molecular viscosity, $\frac{\nu_t}{\nu}$ or $\chi \equiv \tilde{\nu}/\nu$ according to the parameters in the S-A model. Furthermore this factor Ψ can be seen as an increased effective value for C_{DES}. This shield function $\Psi\left(\nu_t/\nu\right)$ for a S-A model can be expressed as:

$$\Psi^2 = \min\left[10^2, \frac{1 - \frac{c_{b1}}{c_{w1}\kappa^2 f_w^*}\left[f_{t2} + \left(1 - f_{t2}\right) f_{v2}\right]}{f_{v1}\max\left(10^{-10}, 1 - f_{t2}\right)}\right] \tag{2.31}$$

with $\kappa = 0.424$ The correction is inactive ($\Psi = 1$) when the subgrid eddy viscosity is higher than about 10ν and becomes stronger for lower values. Note that for the expression of Ψ, the terms which correspond to f_{t2} are ignored.

2.5.3 WMLES branch of IDDES

In contrast to the DDES branch, the WMLES branch will be activated when the inflow conditions are unsteady, contain turbulent content and have a sufficient fine grid to resolve the boundary-layer eddies. To achieve a coupling between RANS and LES, the following blended RANS-LES length scale is used

$$l_{WMLES} = f_B(1 + f_e)l_{RANS} + (1 - f_B)l_{LES} \tag{2.32}$$

with the empirical blending-function f_B defined as:

$$f_B = \min\left\{2\exp(-9\alpha^2), 1.0\right\} \tag{2.33}$$

and $\alpha = 0.25 - \frac{d_w}{h_{max}}$. The blending function is characterized by a rapid switch between the pure RANS mode and LES mode deep inside the boundary layer. This transition is located around the range of wall distance $0.5h_{max} < d_w < h_{max}$ as can be observed from Figure 2.6. The value for f_B in the RANS mode is equal to one and zero for the LES mode. The overall idea of this function is to provide an abrupt change between modes.

Another empirical function f_e in 2.32 can be seen as an 'elevating' function defined as:

$$f_e = \max\left\{(f_{e1} - 1, 0\right\}\Psi f_{e2} \tag{2.34}$$

The function f_e in equation 2.34 is intended to counteract an excessive reduction of the modeled (RANS) Reynolds stresses, which is generally found by the interaction of the RANS and LES regions in the vicinity of their interface. This function is formulated in order to treat the log-layer mismatch. The function f_{e1} in 2.34 is defined as:

$$f_{e1}\left(\frac{d_w}{h_{max}}\right) = \begin{cases} 2\exp(-11.09\alpha^2), & \text{if } \alpha \geq 0 \\ 2\exp(-9.0\alpha^2), & \text{if } \alpha < 0 \end{cases} \tag{2.35}$$

The value for α was already used in equation 2.33 and f_{e1} is clearly only depended on the grid (not on the solution). So this function serves as an 'elevating' for the RANS component of the blended RANS-LES length-scale in equation 2.32. The value of f_{e1} is equal to f_B in the transition zone, defined by $f_B < 1$. The function f_{e2} is formulated as:

$$f_{e2} = 1.0 - \max\left\{f_t, f_l\right\} \tag{2.36}$$

The purpose of f_{e2} is to control the intensity of 'elevating' of the RANS component of the model 2.32 by using the functions f_t and f_l, which are given as:

$$\begin{aligned} f_t &= \tanh\left[(c_t^2 r_{dt})^3\right], \\ f_l &= \tanh\left[(c_l^2 r_{dl})^{10}\right], \end{aligned} \tag{2.37}$$

where the functions r_{dt} and r_{dl} are analog to r_d which was defined in 2.22. The subscript t and l refer to the turbulent viscosity ν_t and laminar viscosity ν. The parameter r_{dt} will be close to 1 in the logarithmic part of the turbulent boundary layer, whereas r_{dl} will be close to 1 in the laminar sublayer. The parameters c_t and c_l are some constants depending on the model. These constants depend on the background RANS model, which are 3.55 and 1.63 for the Spalart-Allmaras-IDDES respectively. Since the functions f_t and f_l depend on r_d (see equation 2.22) (and therefore also on the solution), the function f_{e2} will also depend on the solution. The functions f_t and f_l are close to 1 in the boundary layer and will enforce f_{e1} and f_{e2} to become zero.

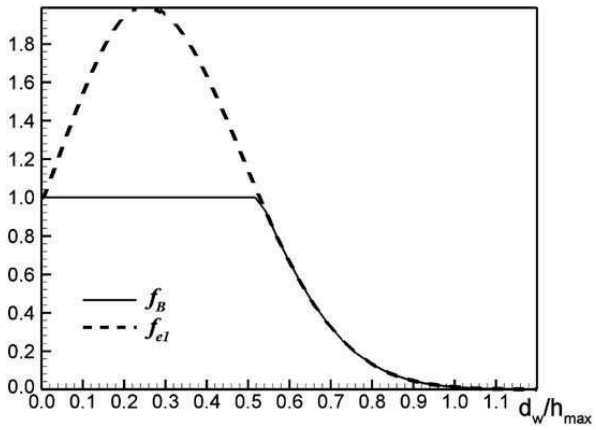

Figure 2.6: Profiles of different blending functions

2.5.4 Hybridization of DDES and WMLES branches

The purpose was to find a method which can ensure an automatic choice of the WMLES or DDES mode, depending on the type of simulation used and the grid used. With the formulations for the DDES-length scale and the one for WMLES this is still not possible. In order to do so, a reformulation of the DDES length-scale and equivalent to 2.30 is defined as:

$$\tilde{l}_{DDES} = \tilde{f}_d l_{RANS} + \left(1 - \tilde{f}_d\right) l_{LES} \tag{2.38}$$

with the modified blending function:

$$\tilde{f}_d = \max\left\{\left(1 - f_{dt}\right), f_b\right\} \tag{2.39}$$

with $f_{dt} = 1 - \tanh\left[(8r_{dt})^3\right]$

Both branches, DDES and WMLES can now be coupled with a hybrid turbulent length scale defined as:

$$l_{hyb} = \tilde{f}_d(1 + f_e) l_{RANS} + (1 - \tilde{f}_d) l_{LES} \tag{2.40}$$

To conclude, it can be observed that when the simulation has an inflow with a turbulent content following is valid. The quantity $r_{dt} << 1$ and results that f_{dt} will be close to 1. Moreover $\tilde{f}_d$ will be equal to f_B so that l_{hyb} will be reduced to l_{WMLES}. On the other hand, when no turbulent content is present, the quantity f_e will drop to zero and therefore the hybrid length scale l_{hyb} is reduced to $\tilde{l}_{ddes}$.

2.6 Summary

1. The unsteady, incompressible and turbulent Navier-Stokes equations are the governing equations.

2. LES filtering is applied for scale separation. Numerical requirements based on common LES simulations should be considered.
3. The Spalart-Allmaras one equation model is used as the closure model
4. The IDDES method is applied as a hybrid RANS-LES method
5. Mesh design is of paramount importance. Mesh influences the transition between the RANS and LES branches.

Chapter 3

CFD Software

This chapter presents a brief overview of the software and the computational methodology used to reach the objective. A more detailed description of such methodologies is available in all kinds of text books and papers. However, this chapter treats the basic principles and methodologies necessary to carry out a LES simulation. Furthermore, the discretization and the numerical schemes are addressed.

3.1 OpenFOAM

There are a lot of CFD packages available to perform a LES simulation. Some of them are already coupled with some build-in acoustic solver. For instance, ANSYS Fluent couples various solvers to the Ffowcs-Williams and Hawkings acoustic analogy. Another solver is FINE Hexa 2.5-4 of NUMECA. Although these packages are being extensively used and proven to be reliable, this research was carried out with OpenFOAM. Here are some of the reasons listed why OpenFOAM is chosen instead of the other CFD packages:

- Free software. Other software packages are rather costly.
- Open source software. It is possible to adapt the code and build new functionalities.
- Is community driven. Various communities work on various fields of applications. This enables a fast evolution.
- Can easily work in parallel.
- Increasing popularity in industries.
- Already used for computing acoustics.

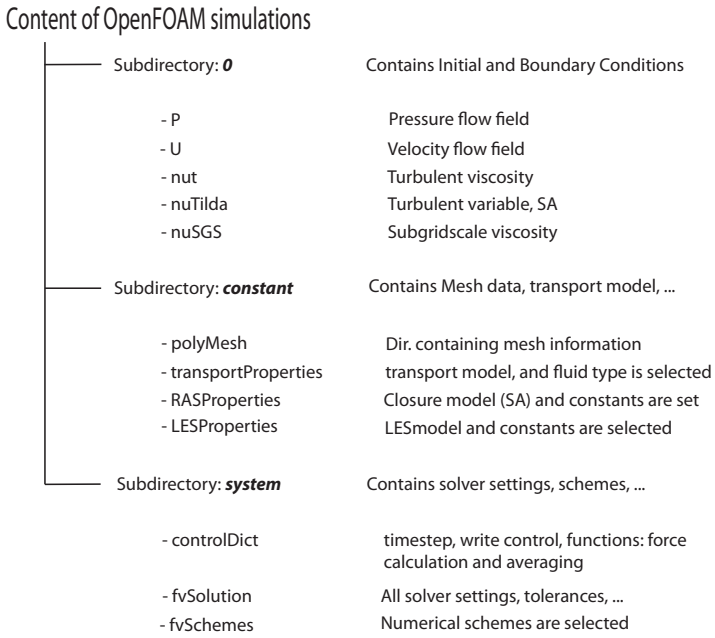

Figure 3.1: Overview of the content of a case in OpenFOAM. Three subdirectories are necessary to define the case.

Although these advantages of OpenFOAM seems to be very promising and guarantee success, it is still a 'relatively new' CFD package. Program errors are still possible and often reported in the community. Therefore, more verification and validation is required and advisable.

3.1.1 Structure OpenFOAM

The key feature of OpenFOAM is that all its packages are written in C++ language. All these items create a bunch of solvers, utilities and libraries, making it an appropriate tool for dealing with fluid dynamics and continuum mechanics. OpenFOAM uses a typical structure to set up a problem. An overview of the three subdirectories which are necessary to create a case in OpenFOAM is given in figure 3.1.

3.2 Discretization

OpenFOAM uses the **F**inite **V**olume (FV) method as a numerical approach for the LES simulation. This section describes how the governing equations are discretised and which numerical schemes are used. It is clear that various possibilities exist. Although altering these schemes could have result in more accurate or faster computation, it is beyond the scope of this research. This thesis only presents the settings which were used for this research.

The FV method is based on the fact that the domain is subdivided or discretized in space.

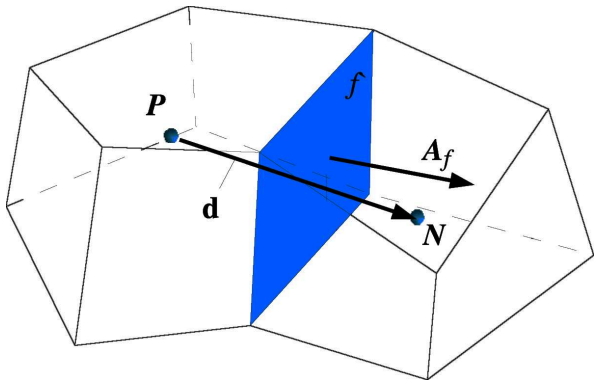

Figure 3.2: Control volumes of a finite volume approach

A time-marching method is needed to solve the quantities in time. Hence a semi-discrete system is used to solve the problem.

A set of control volumes (CV) are used for the spatial discretization. A computational point **P** is defined in each CV, which is bounded by faces of arbitrary shape.

Figure 3.2 shows an example of such CV. A vector **d** is defined, which connects the cell center (eg. **N**) of the adjacent volume. The face normal area vector for the common face between the cells is denoted by **A**. OpenFOAM defines the majority of its variables, p, $\mathbf{u}$ at **P**, resulting in a collocated variable arrangement.

Dealing with unsteady phenomena requires temporal discretization as well. The time domain is divided in time intervals or time steps. A solution is obtained by marching Δt from the initial condition.

The goal is to discretize the governing equations for the Large Eddy simulation of an incompressible, Newtonian fluid. The filtered Navier Stokes equations are presented in equation 2.9b. According to the FV method, and after integrating of CV and in time yields:

$$\int_V \nabla \cdot \overline{\mathbf{u}} dV = \int_{\partial V} d\mathbf{A} \cdot \overline{u} = 0 \tag{3.1}$$

$$\int_t^{t+\Delta t} \left[\frac{d}{dt} \int_V \overline{\mathbf{u}} dV + \int_V \nabla \cdot (\bar{\mathbf{u}}\bar{\mathbf{u}}) dV - \int_V \nabla \cdot \nu_{eff} (\nabla \overline{\mathbf{u}} + \nabla \overline{\mathbf{u}}^T) dV \right] dt = \tag{3.2}$$

$$- \int_t^{t+\Delta t} \left[\int_V \frac{\nabla \bar{p}}{\rho} dV \right] dt \tag{3.3}$$

The equation above appears to be a second-order equation, due to a a diffusion term, introducing a second derivative. Therefore, to obtain a good accuracy, the order of discretization should be equal (second order) or higher than the equation. Furthermore, the temporal discretization should also be of second order. A transported quantity, i.e. velocity, pressure is

assumed to vary linearly around the point and time t. Applying a Taylor series, one obtains:

$$\phi(x) = \phi_P + (\mathbf{X} - \mathbf{X}_P) \cdot (\nabla\phi)_P + \mathcal{O}\left(|\mathbf{X} - \mathbf{X}_P|^2\right), \tag{3.4}$$

$$\frac{\partial\phi(t)}{\partial t} = \frac{\phi(t + \Delta t) - \phi(t)}{\Delta t} + \mathcal{O}(\Delta t). \tag{3.5}$$

Each term in the governing equations will be treated separately. The spatial discretization is considered first, followed by the temporal discretization.

3.2.1 Spatial discretization

First the evaluation of the various volume, surface, divergence and gradient integrals on a control volume are briefly addressed. A full derivation is provided in Jasak (1996).

$$\begin{aligned}
&\text{Volume integral:} && \int_{V_p} \phi(\mathbf{x})\, dV \approx \phi_P V_P \\
&\text{Surface integral:} && \int_f \phi d\mathbf{A} = \phi_f \mathbf{A}_f \\
&\text{integral of divergence:} && \int_{V_P} \nabla \cdot \phi dV \approx \sum_f \mathbf{A}_f \cdot \phi_f \\
&\text{integral of gradient} && \int_{V_P} \nabla\phi dV \approx \sum_f A_f \phi_f
\end{aligned} \tag{3.6}$$

Convection term

The discretization of the convection term is established by applying the integral of a divergence in 3.6. The convective term becomes:

$$\int_{V_P} \nabla \cdot (\bar{\mathbf{u}}\phi)\, dV = \sum_f \mathbf{A} \cdot (\bar{\mathbf{u}}\phi)_f = \sum_f (\mathbf{A} \cdot (\bar{\mathbf{u}})\, \phi_f = \sum_f F\phi_f, \tag{3.7}$$

where F is defined as the volume flux through the face $F = \mathbf{A} \cdot \bar{\mathbf{U}}_f$. Some second order interpolation between the cell value $\mathbf{P}$ and its neighbouring value, is required to obtain the values at the faces.

Diffusion term

The volume integral of the diffusion term is discretized as

$$\int_{V_P} \nabla \cdot (\nu\nabla\phi)\, dV = \sum_f \mathbf{A} \cdot (\nu\nabla\phi)_f = \sum_f \nu_f \mathbf{A} \cdot (\nabla\phi)_f, \tag{3.8}$$

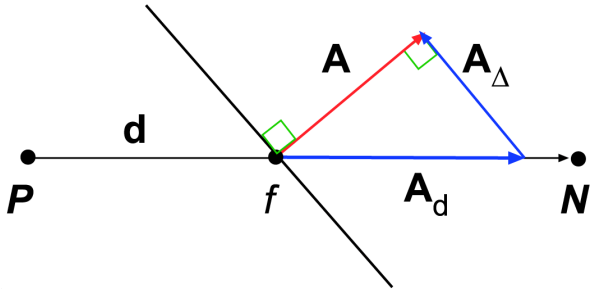

Figure 3.3: Decomposition of a non-orthogonal cell

The terms in the right hand side of 3.8 should be evaluated with an appropriate method. The scalar ν_f can simply be found by an interpolation. The other term $\mathbf{A} \cdot (\nabla\phi)_f$ is very mesh depended and will be addressed now. For an orthogonal mesh, the face gradient of ϕ can be expressed as in equation 3.9. For such a mesh, the vectors $\mathbf{d}$ and $\mathbf{A}$ are parallel.

$$\mathbf{A} \cdot (\nabla\phi)_f = |\mathbf{A}| \frac{\phi_N - \phi_P}{|\mathbf{d}|}, \tag{3.9}$$

where N refers to the neighbouring cell of $\mathbf{P}$. When the mesh is non-orthogonal, the second order accuracy is not valid any more when applying equation 3.9. An additional term, reflecting the non-orthogonality arises. Figure 3.3 shows a schematic overview of cell non-orthogonality.

$$\mathbf{A} \cdot (\nabla\phi)_f = \underbrace{|\mathbf{A}_d| \frac{\phi_N - \phi_P}{|\mathbf{d}|}}_{orthogonal} + \underbrace{\mathbf{A}_\Delta \cdot \left(\widetilde{\nabla\phi}\right)_f}_{non-orthogonal} \tag{3.10}$$

If the non-orthogonality of a mesh is high, the correction can result in negative coefficient, which can lead to instability. As a consequence the correction is rather limited, and accuracy will be reduced. For LES simulations, the order of accuracy of the set of equations is important. Therefore, one should aim for building a mesh with limited non-orthogonality.

3.2.2 Temporal discretization

Like with the spatial discretization, there are a wide range of ways to perform a temporal discretization. The most important thing to remember is that each term in the transport equation should be second order accurate. A Cranck-Nickolson scheme is known to perform very well, but this is considered to be rather expensive and therefore unwanted. Another method is the second order backward differencing approach, which will be addressed now.

Second order Backward Differencing (BD)

This type of temporal discretization uses three time steps to achieve a second order accuracy. The temporal derivative is given as:

$$\frac{\partial \phi}{\partial t} = \frac{\frac{3}{2}\phi^{n+1} - \phi^{n} + \frac{1}{2}\phi^{n-1}}{\Delta t} \tag{3.11}$$

Through the simulation, the truncation error should be minimized. However, small variation in face fluxes and derivatives can cause errors. This errors can be considered as an additional diffusion, which could have a detrimental effect on the LES simulations. The problem is due to the fact that such errors can exceed the sub-grid diffusion.

To maintain stability throughout the simulation, the cell face Courant number, defined by 3.12 should be set below 1.

$$CFL = \frac{\bar{\mathbf{u}}_f \cdot \mathbf{n}}{|\mathbf{d}|} \tag{3.12}$$

Therefore, for LES simulations the time step is typically very small, resulting in a small temporal diffusion error.

3.2.3 Pressure-Velocity Coupling

Since both pressure and velocity quantities depend on each other, a pressure equation is used to couple those quantities. The pressure equation is based on a semi-discretized formulation of the momentum equation. The pressure equation is given as:

$$a_p \bar{\mathbf{u}}_p = \mathbf{H}(\bar{\mathbf{u}}) - \nabla \bar{p} \tag{3.13}$$

The details of further derivations are not considered here, but it is known that the final form of the full Navier-Stokes equations can be written as:

$$a_p \bar{\mathbf{u}}_p = \mathbf{H} - \sum_f \mathbf{A} \cdot \bar{p}_f \tag{3.14}$$

$$\sum_f \mathbf{A} \cdot \left(\frac{1}{a_p}\right)_f (\nabla \bar{p})_f = \sum_f \mathbf{A} \cdot \left(\frac{\mathbf{H}}{a_p}\right)_f \tag{3.15}$$

Detailed information can be found in (de Villiers, 2006; Jasak, 1996). Here, a_p is a set of coefficients, depending on $\bar{u}_p$. The $\mathbf{H}$ vector consists of a convection part and a source contribution, which includes source terms, transient terms, except the pressure term. For unsteady simulations, like in this study, the PISO (Pressure Implicit with Splitting of Operators) as proposed by (Issa, R.I., 1986; Wesseling, P., 2001) is a preferred scheme. The PISO algorithm solves the equations 3.14 and 3.15 successively.

3.2.4 Turbulence Modeling Implementation

This study was focused on the use of the Spalart-Allmaras model, which was already introduced in 2.3. The S-A equation shows some similar time, convective and diffusive terms, which follow the classical discretization methods as before. Recalling the S-A equation:

$$\frac{\partial \tilde{\nu}}{\partial t} + \nabla \cdot (\tilde{\nu}\bar{\mathbf{u}}) - \frac{1}{\sigma}\nabla \cdot ((\nu + \tilde{\nu})\nabla\tilde{\nu}) = \underbrace{c_{b1}\tilde{S}\tilde{\nu}}_{production} + \underbrace{\frac{1}{\sigma}c_{b2}(\nabla\tilde{\nu})^2}_{transport} - \underbrace{c_{w1}f_w\left(\frac{\tilde{\nu}}{\tilde{d}}\right)^2}_{dissipation} \tag{3.16}$$

where the values of the constants and expressions for the functions can be found in table 2.1. The production terms derived as an explicit function of $\tilde{\nu}^{n-1}$, where $n-1$ refers to previous time step. In such a way, one can enhance the stability of the solution. The production term is given as:

$$\tilde{\nu}_{production} = c_{b1}\left[|\nabla \times \bar{\mathbf{u}}| + \frac{\tilde{\nu}^{n-1}}{\kappa^2\tilde{d}^2}f_{v2}\right]\tilde{\nu}^{n-1} \tag{3.17}$$

The transport term is discretized as:

$$\tilde{\nu}_{transport} = \frac{c_{b2}}{\sigma}\nabla\tilde{n}u^{n-1} \cdot \sum_f \mathbf{A} \cdot \tilde{\nu}_f \tag{3.18}$$

The destruction term becomes:

$$\tilde{\nu}_{dissipation} = -\left[c_{w1}f_w\frac{\tilde{\nu}^{n-1}}{\tilde{d}^2}\right] \cdot^{z} \tag{3.19}$$

Note that the functions f_{v2} and f_w are also function of $\tilde{\nu}^{n-2}$.

3.3 Solving the Navier-Stokes equations

Now the discretized Navier-Stokes, and the PISO algorithm is addressed, it is possible to describe the approach to solve the Navier-Stokes and consequently to perform a LES simulation. The global solution procedure is summarized in figure 3.4 and the different steps are now briefly considered:

1. A RANS solution, containing the pressure, velocity, turbulent viscosity and face fluxes is used as the initial field to start the LES simulation.
2. In the next step, the turbulent properties are updated, according to previous time-steps.
3. The pressure-velocity coupling is solved based on the PISO algorithm. A prediction of the velocity field is made, based on previous flow fields and equation 3.15. A preconditioned bi-conjugate gradient solver (PBiCG) applicable to asymmetric matrices is used. As a preconditioner the Diagonal incomplete-LU (DILU) method is applied.

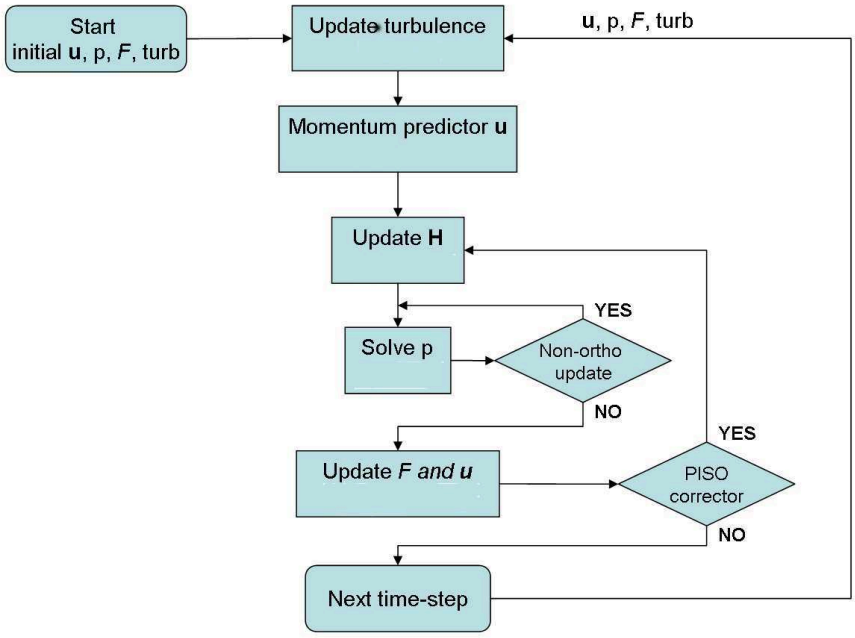

Figure 3.4: Schematic overview of the solution procedure.

4. The **H**-vector is updated by the predicted velocities. Therefore the pressure equation 3.13 is solved according to the preconditioned conjugate gradient solver applicable to symmetric matrices. A significant improvement with respect to computational time is established with the generalized geometric-algebraic multi-grid solver (GAMG) as a preconditioner.

5. The pressure equation is solved iteratively and non-orthogonal correctors are used to sustain convergence. In this LES simulations, zero or only 1 corrector was used.

6. The velocities and the fluxes are updated with the new pressure using some continuity formulations. The number of PISO loop correctors can be set in a way that a certain tolerance on the quantities is achieved. For these simulations, it was found that 2 correctors were sufficient.

7. Simulation can proceed to the next time step where, the calculated values are used to make an initial guess.

3.4 Solvers and Preconditioners

A great amount of computational savings could be achieved by setting the solvers, preconditioners and tolerances in a decent format. The subdirectory *fvSolution* includes those settings and conditioners. The applied settings for the PISO scheme are given in Appendix C. Solving

the pressure equation is considered as the most computational demanding. The generalized geometric-algebraic multi-grid solver (GAMG) was selected as a preconditioner to solve the pressure equation. According to OpenCFD (2011), GAMG uses the principle of: generating a quick solution on a mesh with a small number of cells; mapping this solution onto a finer mesh; using it as an initial guess to obtain an accurate solution on the fine mesh. GAMG is faster than standard methods when the increase in speed by solving first on coarser meshes outweighs the additional costs of mesh refinement and mapping of field data. In practice, GAMG starts with the mesh specified by the user and coarsens/refines the mesh in stages. The Preconditioned Conjugate Gradient (PCG) solver is used to solve for pressure equation. A speed-up of the calculation procedure was realized by selecting GAMG instead of DIC as preconditioner. The other terms are solved using a Preconditioned Bi-Conjugate Gradient (PBiCG) solver for asymmetric LDU matrices, where LDU refers to Lower triangular, Diagonal, Upper triangular.

3.5 Summary

- OpenFOAM provide a suitable environment for current simulations.
- OpenFOAM enables to work on multiple computer processors in parallel, making large computations as LES possible.
- More extensive work, concerning validation and verification is necessary due to possible bugs.
- A good mesh quality can enhance the computational speed.
- GAMG was used to solve the pressure equation. Hence, serious computation savings were achieved.
- Current simulations were done with only one setting of discretization. All runs were found to be stable and there was no need to alter the settings, although it could have improved the result. Further investigation on this is required.

Chapter 4

Computational Aero-acoustics

Previous chapters were all focused on the simulation of aerodynamic quantities. This chapter discusses the method to solve the acoustics.

4.1 Review of Computational Aero-acoustics

In the introduction, it was concluded that the direct noise simulations are not appropriate for the test cases considered in this thesis. A direct simulation has stringent demands on computational power and difficulties to simulate simultaneously the noise generating sources and propagating waves. Therefore, it was chosen to use a hybrid CAA methodology to compute the farfield acoustics. In such a method, the problem is decomposed into simulating the aerodynamic source regions and the acoustic field. Accordingly, to identify the farfield noise, one has two perform two stages:

1. An accurate description of the noise mechanisms is provided by the classical CFD techniques. The CFD technique, presented in chapter 2 will be used to solve the time-dependent incompressible Navier-Stokes equation.

2. The aerodynamic solution of the first step is used to obtain the noise mechanisms. Here the aerodynamic variables are transformed into the acoustic variables. The sources are transported to the farfield according to the acoustic waves.

This chapter will mainly focus on the last step. The first step was already considered in chapter 2. For the second step, one can apply various strategies, concerning the acoustic analogies, linearized Euler equations, wave equations or APE. As a matter of convenience, only the acoustic analogies are considered. Additional information on the computational acoustic techniques is provided in Wagner et al. (2007); de Roeck (2007).

4.2 Acoustic Analogies

The technique of the acoustic analogies was established by (Lighthill, M.J., 1952) and since then multiple times used for aero-acoustic problems. The basic idea behind the analogy is to rewrite the Navier-Stokes equations, in which the left hand side is some wave operator and the right hand side is considered as the source terms. Due to some limitations, Lighthill is modified to make it applicable for more general problems. The basic theories will be discussed in more detail in this section.

4.2.1 Lighthill's acoustic analogy

Lighthill obtained his scalar function with respect to the acoustic variable ρ by taking the time derivative of the continuity equation 2.3b and subtracting the divergence of the momentum equation. Note that in these calculations, the absence of external forces and mass sources is assumed. Adding the term $-c_0^2\partial^2\rho/\partial x_i$ to both sides yields in the famous Lighthill's equation:

$$\frac{\partial^2\rho}{\partial t^2} - c_0^2\nabla^2\rho = \frac{\partial^2 T_{ij}}{\partial x_i x_j} \tag{4.1}$$

where T_{ij} is the Lighthill tensor and defined as:

$$T_{ij} = \rho u_i u_j + \left(p - c_0^2\rho\right)\delta_{ij} - \tau_{ij} \tag{4.2}$$

Since no assumptions were made, the equation 4.1 is still an exact formulation and contains physics such as propagation. If the Lighthill tensor is considered as quadrupole source term, the left hand side refers to the propagation, resulting in an inhomogeneous wave equation. However, the left hand side is only applicable for ordinary waves. For problems where such an isotropic wave operator is not appropriate, Lighthill's equation is not applicable.

4.2.2 Curle's Analogy: the influence of solid boundaries

An extension of Lighthill's analogy was proposed by (Curle, N., 1955). The difference is that this analogy incorporates the influence of the presence of solid boundaries. Now the global sound field is a contribution of two origins:

1. Quadrupole sources (Lighthill), which are present in the vicinity of the solid boundaries.
2. Dipole sources, generated by fluctuating aerodynamic forces on the solid boundaries, acting on the fluid.

The additional contribution is reflected in a new term $\partial f_i/\partial x_i$, appearing on the right hand side of 4.1. It is known that at low Mach numbers, the dipole sources are more efficient noise mechanisms than the quadrupole sources. The surfaces will reflect and diffract the radiated

sound, changing wave characteristics. Consequently, the acoustic field is often calculated by the contribution of the dipole sources only, and neglecting the quadrupole sources.

The most general solution of the inhomogeneous wave equation 4.1 on a bounded domain is:

$$\rho' = \frac{1}{4\pi c_0^2}\int_V \frac{\partial^2 T_{ij}}{\partial y_i y_j}\frac{1}{|\mathbf{x}-\mathbf{y}|}dV(\mathbf{y}) + \frac{1}{4\pi}\int_S \left\{\frac{1}{r}\frac{\partial \rho}{\partial n} + \frac{1}{r^2}\frac{\partial r}{\partial n}\rho + \frac{1}{c_0 r}\frac{\partial r}{\partial n}\frac{\partial \rho}{\partial t}\right\} dS(\mathbf{y}) \tag{4.3}$$

In equation 4.3, all the quantities $\frac{\partial^2 T_{ij}}{\partial y_i y_j}$,$\frac{\partial \rho}{\partial t}$,$\rho$ and $\frac{\partial \rho}{\partial n}$ are evaluated at the retarded times $t - r/c_0$. The parameter $r = |\mathbf{x}-\mathbf{y}|$, where $\mathbf{x}$ and $\mathbf{y}$ are the locations of the observer and sound source respectively. Note that $\mathbf{n}$ is the outward normal from the fluid. The first integral in 4.3 is taken over the total volume V external to the solid boundaries, whereas the second refers to the surface S of the solid boundaries. Due to the complexity of previous notation, Curle has rewritten it into a more applicable form:

$$\rho(\mathbf{x},t) = \frac{1}{4\pi c_0^2}\frac{\partial^2}{\partial x_i \partial x_j}\int_V \frac{T_{ij}}{r}dV(\mathbf{V}) - \frac{1}{4\pi c_0^2}\frac{\partial}{\partial x_i}\int_S \frac{n_j}{r}\left(p\delta_{ij} - \tau_{ij}\right)dS(\mathbf{y}) \tag{4.4}$$

In order to come to previous solution, one introduced the free-space Green's function G and performed some proper mathematical operations. More detail about the derivation and the corresponding Green's function is provided in (Rienstra and Hirschberg, 2001; Goldstein, 1976). Getting rid of the derivatives in the integral and applying $\rho' = p'/c_0^2$ yields in a far-field approximation:

$$\begin{aligned} p'(\mathbf{x},t) \cong & \frac{x_i x_j}{4\pi \|\mathbf{x}\|^2 c_0^2}\frac{\partial^2}{\partial t}\int_V \left[\frac{T_{ij}}{r}\right]_{t_e} dV(y) \\ & - \frac{1}{4\pi}\frac{\partial}{\partial t}\int_S \left[\frac{\rho v_i}{r}\right]_{t_e} n_i dS \\ & - \frac{x_j}{4\pi \|\mathbf{x}\| c_0}\frac{\partial}{\partial t}\int_S \frac{\mathbf{P}_{ij} + \rho v_i v_j}{r} n_i dS \end{aligned} \tag{4.5}$$

Assuming the source region acts as a compact body, one can neglect the variation of the retarded time t_e over the surface and can write $r = |\mathbf{x}|$ if the origin is $\mathbf{y} = 0$ inside the body. Furthermore, the second integral refers to a monopole-like sound field, due to the mass flux through the surface S. This integral can be omitted, for the test cases considered here. The stress tensor $\mathbf{P}_{ij} = p\delta_{ij} - \sigma_{ij}$, contains in the effect of the hydrodynamic pressure and a viscosity related term σ_{ij}, which will not be considered further. Additionally, the velocities v_i and v_j at the surfaces are zero.

$$\begin{aligned} p'(\mathbf{x},t) \cong & \frac{x_i x_j}{4\pi \|\mathbf{x}\|^3 c_0^2}\frac{\partial^2}{\partial}\int_V \left[T_{ij}\right] dV(y) \\ & - \frac{x_j}{4\pi \|\mathbf{x}\|^2 c_0}\frac{\partial}{\partial t}\int_S p n_i dS \end{aligned} \tag{4.6}$$

Assumptions

In order to come to 4.6 some assumptions were made and the formulation is not exact anymore. It is important to note when the Curle's formulation is applicable. The assumptions, which are for paramount importance in this thesis will be itemized here.

1. The position of the listener $|\mathbf{x}|$ is large enough with respect to the surface. Moreover $|\mathbf{x}| >> \lambda$, where λ is the wavelength of the sound generated, so that $|\mathbf{x}|$ lies in the radiation field of each dipole along the surface.
2. The position of the listener is large compared to the typical dimension of the solid boundaries L.
3. If one assumes that $L << c_0/f$, where f is the sound frequency, one can neglect r/c_0 of the retarded time. This implies that
$$L << \frac{c_0}{f} \approx \frac{c_0 L}{U_0} \quad \text{i.e. if} \quad \frac{U_0}{c_0} << 1 \tag{4.7}$$
4. The first integral in equation 4.6 can be neglected for flows with low Mach numbers. The quadrupole sources contained in the volumes are therefore not considered.

Dimension Analysis

Due to the simple integral solutions of the acoustic analogies, it was possible for Lighthill to predict the behaviour of jet noise. Even though, he was not able to perform and validate his results. Assuming that the frequency and the Lighthill's stress tensor are proportional to, U_0 and $\rho_0 U_0^2$, he revealed that the pressure fluctuations scales with:

$$p'(\mathbf{x},t) \sim \rho_0 U_0^2 M^2 \frac{L}{\|\mathbf{x}\|} \tag{4.8}$$

where L is the characteristic length scale. Since the acoustic power density for the farfield is defined as:

$$I_{ac} = \frac{\left\langle p'^2 \right\rangle}{\rho_0 c_0} \tag{4.9}$$

where the brackets refer to long time averaging. According to 4.8 and 4.9 he found that the radiated power or intensity of sound generated by quadrupoles varies with the eight power of the mean velocity. Lighthill's eight power law is given as:

$$I_{ac_q} \sim \rho_0 U_0^3 M^5 \frac{L^2}{\|\mathbf{x}\|^2} \sim U_0^8 \tag{4.10}$$

A same analysis can be performed for Curle. For a dipole source, the pressure fluctuation and the acoustic intensity are proportional to:

$$p'(\mathbf{x},t) \sim \rho_0 c_0^{-1} U_0^3 \frac{L}{\|\mathbf{x}\|} \qquad I_{ac_D} \sim \rho_0 M^3 U^3 \frac{L^2}{\|\mathbf{x}\|^2} \sim U_0^6 \tag{4.11}$$

4.2.3 The Ffowcs-Williams and Hawkings analogy

An even more advanced acoustic analogy than Lighthill and Curle was established by (Ffowcs Williams and Hawkings, 1969). Contrary to previous analogy, where a stationary solid boundary was assumed, this analogy can take the arbitrary motion of solid boundaries into account. Typical applications for this analogy are the noise prediction of fans, helicopter blades and full scale wind turbines. Although the test cases in this thesis are steady, this method is worth to be mentioned, due to its generality and its use in industrial applications. The key idea is to use generalized functions to rewrite the governing equations and make them valid for the whole domain, including the fluid and the solid bodies. The formulation of FW-H will not be considered in detail, but will only be given for completeness. Detailed derivations can be found in Ffowcs Williams and Hawkings (1969); de Roeck (2007); Wagner et al. (2007).

$$\begin{aligned} p'(\mathbf{x},t) = & \frac{1}{4\pi}\frac{\partial^2}{\partial x_i \partial x_j}\int_V \left[\frac{T_{ij}}{r(1-M_r)}\right]_{t_e} dV \\ & - \frac{\partial}{\partial x_i}\int_S \left[\frac{L_i}{r(1-M_r)}\right]_{t_e} dS \\ & + \frac{\partial}{\partial t}\int_S \left[\frac{Q}{r(1-M_r)}\right]_{t_e} dS \end{aligned}$$

with

$$\begin{aligned} Q &= \rho_0 U_i n_i & U_i &= \left(1 - \frac{\rho}{\rho_0}v_i + \frac{\rho u_i}{\rho_0}\right) \\ L_i &= P_{ij} + \rho u_i (u_n - v_n) & P_{ij} &= p'\delta_{ij} - \tau_{ij} \\ T^*_{ij} &= \rho u_i u_j + (p' - a^2\rho')\delta_{ij} - \tau_{ij} \end{aligned} \tag{4.12}$$

4.3 Acoustic Relations

Sound Pressure Level (SPL)

Sound is a weak pressure disturbance which travels through a fluid as a wave. The pressure disturbances p' are generally very low compared to the atmospheric pressure. A human ear has a very large range, wherein it can detect pressure fluctuations. This range varies between the $20Hz$ and $20kHz$ as the lower and upper limits, respectively. Due to this large range, the measure of sound levels are expressed on a logarithmic scale. The pressure amplitude is given by the **S**ound **P**ressure **L**evel (SPL) as:

$$SPL = 20\log_{10}\frac{p'_{rms}}{p_{ref}} \tag{4.13}$$

where the SPL is given in decibels (dB). The human ear hearing in air as medium is the threshold for determining the reference pressure $p_{ref} = 2 \cdot 10^{-5} Pa$. This reference pressure corresponds to a SPL value of $0dB$.

Sound Intensity

Another interesting quantity is the intensity, given by:

$$IL = 10 \log_{10} \left(\frac{\langle I \rangle}{I_{ref}} \right) \tag{4.14}$$

where $I_{ref} = 10^{-12} W m^{-2}$ for air and $\langle I \rangle = \frac{p'^2}{\rho_0 c_0}$.

Frequency and Wavelength

The temporal variation of harmonic waves are described by their frequency f or angular frequency $\omega = 2\pi f$, whereas the spatial variation is defined according to its wavelength λ or the wavenumber $k = 2\pi/\lambda$. The propagation speed of the wave, here c_0 relates the frequency and the wavelength through:

$$c = \lambda f = \frac{\omega}{k} \tag{4.15}$$

4.4 Summary

- An incompressible flow solver can be used for compressible acoustic effects, in case the flow has a low Mach number.
- Only the acoustic analogies are considered here. Its well known reliability and simplicity of implementation makes it possible to generate a fast postprocessing tool.
- The effect of solid boundaries has to be taken into account. This makes the Curle's formulation suitable as an acoustic analogy.
- Curle describes the contributions of 2 distinct origins. First the quadrupole field which represents, according to Lighthill the fluctuating applied stresses. Secondly, a dipole field which represents the fluctuating force with which the solid boundaries act on the fluid.
- Only the compact formulation of Curle was implemented.
- A dimensionless analysis has shown that when considering low Mach numbers, the dipole contribution is larger than the quadrupole contribution to the sound field. Therefore only pressure fluctuations along the boundary surface are considered.

Chapter 5

Verification and Validation

There are two types of verifications necessary in computer simulations. The first one is based on code verification, whereas the second one refers to the verification of the solution. The verification of the code is considered as an elaborated and complicated task and is beyond the scope of this thesis. It is however important to know that OpenFOAM was already used for the computation of acoustic noise sources. In Eugene, a detached eddy simulation was used to compute surface fluctuations along a mirror. Note that in this thesis, a different turbulence method was used and that it is important to be aware that code errors can contribute to errors throughout the simulation. In the development and its open-source nature, it is clear that bugs are often reported. If it would have been possible, this code verification should have deserved more attention and elaboration.

This chapter presents some simple approaches to verify and validate OpenFOAM and the implementation of the acoustic analogy. A simple flat plate geometry is used as a preliminary validation of OpenFOAM and the applied turbulence model IDDES. The acoustic analogy is tested at the end of this chapter by assuming a source function and its known analytical solution. Furthermore an overview of some test cases will be addressed. Thereby, more attention is given to the process which was followed to come to the final computational set up. An important challenge over here was to find a decent numerical grid to give confidence of the numerical solution. Therefore, a grid study was necessary and was used to quantify the model errors. Moreover choosing and finding a correct set-up turbulence model was also part of this work. The results of the CFD simulations will be given in the next chapter. The items below give a clear indication and overview of what is being discussed in this chapter:

1. The boundary layers of a flat plate geometry are investigated and compared with reference data of fluent and DNS simulations.
2. The turbulence model is chosen and motivated.
3. The test meshes and computational set-up are presented. This part also contains the results of the grid independence study based on the force coefficients.

4. The implementation of the Curle's acoustic analogy is verified by an analytical solution. Moreover a grid study regarding previous test meshes and based on the acoustic results is presented.

5. An interim conclusion will be presented at the end of this chapter.

5.1 The Flat Plate

Like for every numerical CFD software, it is inevitable to verify the CFD code. In a code verification one requires to perform some procedures to identify code mistakes that can affect the simulation. Roy (2005), gives a good overview about measures which can be taken to verify and validate software and simulation results.

No special attention on this verification procedures for the CFD software is given in this thesis as it is assumed it has already been done by the developers. However it is still possible to validate the results of some simple test case. A flat plate geometry is considered as this simple test case and the boundary layer profiles can easily be compared with reference data of Schlatter and R. (2010). In this reference, a canonical turbulent boundary layer under zero pressure gradient is studied via DNS. Note that in the DNS simulation the transition to turbulence of the inflowing laminar Blasius boundary layer is achieved with a random volume force. The simulations in this thesis do not have a turbulent strip, nor a boundary layer profile at the inlet. Data are available for different Reynolds numbers ($Re_\theta = 180$ to $Re_\theta = 4300$), based on the momentum thickness θ and free-stream velocity U_∞. The solution domain with dimensions is presented in Figure 5.1.

The dimensions of the domain are $1m \times 0.5m \times 0.1m$ for the x, y and z direction respectively and the domain has correspondingly 499, 74 and 19 cells in each dimension. Near the wall the cells are clustered to capture the boundary layer dynamics. The inflow freestream velocity is selected to be $26m/s$ and is uniform over the entire inlet boundary. The set of other boundary conditions are equal to the boundary conditions for other simulations and are summarized in table 5.3. The results would certainly have been improved when a more advanced boundary condition at the inlet was used. For instance, a Blasius boundary layer profile or mapping of the outlet to inlet are more appropriate for this type of case. The mean velocity profiles in wall coordinates are shown in Figure 5.2. The mean velocity profiles are located where the boundary is fully turbulent and computed with:

$$u^+ = \frac{u}{u_\tau} \tag{5.1}$$

$$y^+ = \frac{y u_\tau}{\nu_\infty} \tag{5.2}$$

where $u_\tau = \sqrt{\tau_w/\rho_\infty}$ is the wall friction velocity and τ_w the wall shear stress.

The velocity profiles of five simulations are shown in Figure 5.2. The thick blue line is considered as the DNS reference result by Schlatter and R. (2010). The thin black line is a steady state RANS simulations with the realizable k-epsilon turbulence model with enhanced

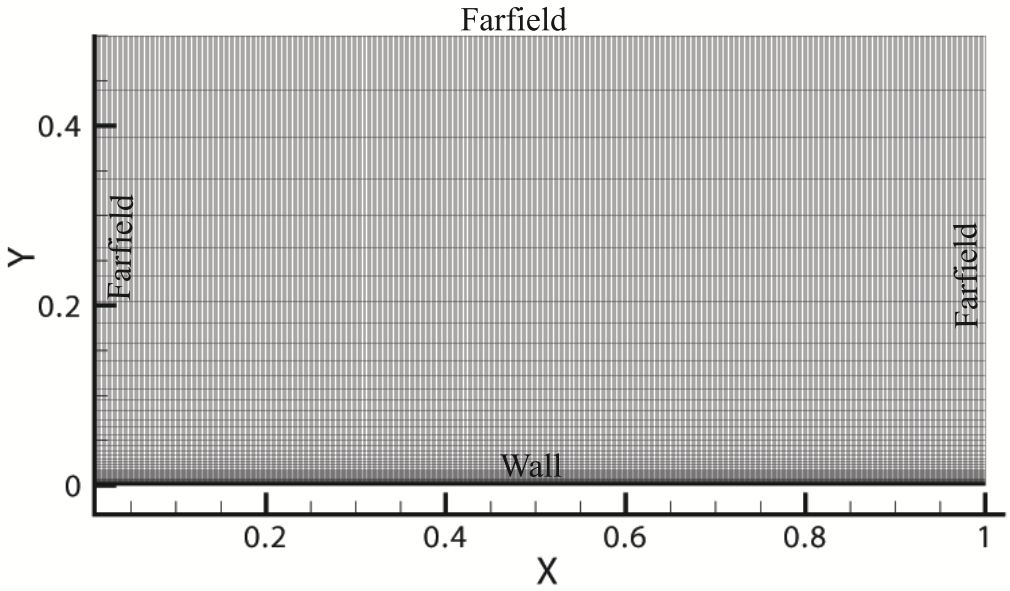

Figure 5.1: Solution domain flat plate geometry

wall treatment, carried out by another master student (Wijnen (2011)) in fluent. The full colored thick lines are all done with the OpenFOAM software. The pink line is the result of a steady-state RANS simulations with the Spalart-Allmaras turbulence model, which was also used for the further simulation with IDDES. This velocity profile is depicted at the position $x = 0.5m$. The RANS profile is compared with the DNS reference simulation and shows similar deviations as the fluent results. Both the viscous sublayer, the buffer layer and the log-law of the boundary layer are captured well. Therefore one can assume that the implementation of the Spalart-Allmaras model is properly done. The green and red curve shows the averaged velocity profiles of the IDDES simulations for $t = 0.0612s$ at the locations of $0.5m$ and $0.98m$ respectively. A slight difference between these profiles is noticeable, especially in the upper region. However the same trend as the reference data can be noticed. The latter profiles behaves better than the one in the middle of the plate. It can be expected that at this position the boundary layer is not yet fully turbulent and probably a longer plate and other boundary conditions would have been better. Also selecting the same position as the reference was hard to achieve. Note that in the simulations of OpenFOAM no use was made of a turbulent strip or a velocity profile at the inlet of the domain. Furthermore, it is also possible that the averaging process was too limited. Still a good global behaviour of the boundary layer profile was captured. With this test the IDDES approach confirms its capabilities of treating an attached boundary layer.

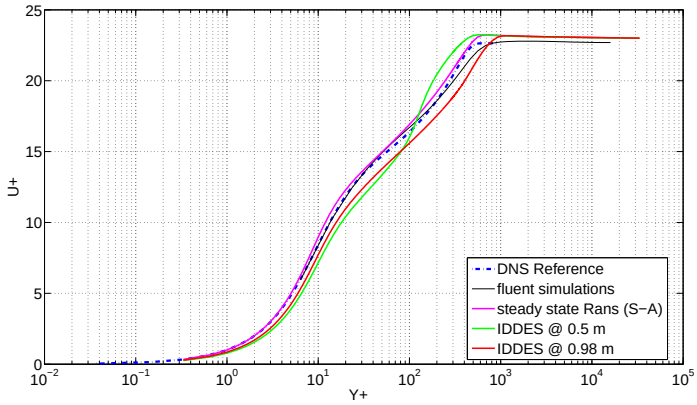

Figure 5.2: Velocity boundary layer profile for flat plate. Reference data by Schlatter and R. (2010) and fluent are included. The steady state RANS simulation with S-A model is provided by pink curve. The boundary layer profiles at two locations for the IDDES simulation are shown in green and red color.

5.2 The turbulence model

Solving an aero-acoustic problem requires the solution of small turbulent scales. A proven method is based on LES simulations, but is found to be rather slow. Using some variant of the DES, which were already mentioned in 2.4.1 is more appropriate for solving external aerodynamics. Here two variants are tested, namely the classical DES and the IDDES, which both make use of the Spalart-Allmaras closure model. For these cases, the same mesh and solver settings is applied in order to compare both methodologies. In the work of de Villiers (2006) it was concluded that the S-A DES model is very mesh depended and performs bad when a medium refined mesh is considered. Moreover, he found that the the Spalart-Allmaras DES was not suitable for cases when a weakly separated flow was expected. The problem here is that in boundary layer dominated flows, the model excessively damps the resolved turbulence near the wall. However, it was proven to be a very robust model. Since the test cases in this thesis will be characterized by small regions of separations, this methodology could have unexpected phenomena. Therefore the improved delayed detached eddy simulation was also investigated since it was designed to maintain the RANS mode throughout the whole boundary and solve it properly. One modification is based on a new definition of Δ, which includes the wall distance and not only the local characteristics of the grid, whereas normally the cube root volume is used. The IDDES was developed to avoid GIS and LLM, commonly found in ambiguous grids.

The modification tends to depress Δ near the wall and give it a steep variation, which stimulates instabilities, boosting the resolved Reynolds stress according to Spalart (2009). The feature was also noticed in the runs by a earlier fluctuating force coefficient and turbulent structures given by the Q-isosurfaces shown in Figure 5.3, 5.4 and 5.5. The Q corresponds to the second invariant tensor given as:

$$Q = \frac{1}{2}\left(\|\mathbf{W}\|^2 - \|\mathbf{S}\|^2\right) \tag{5.3}$$

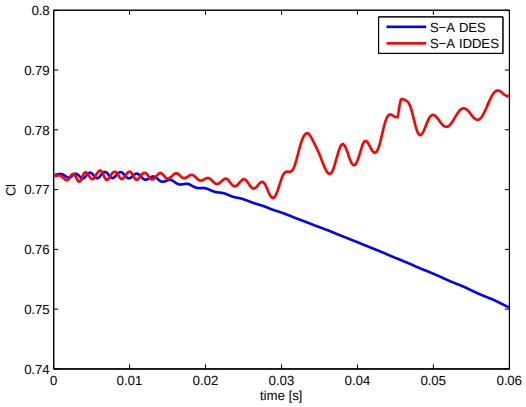

Figure 5.3: Cl coefficients for S-A DES and S-A IDDES model on the same mesh. Result of a preliminary run for a NACA 0012 with seven degrees angle of attack.

where the **W** is the antisymmetric part of the velocity gradient tensor and **S** is the local rate of strain tensor. Large (positive) values of Q indicate regions where the rate of strain is dominated by the rate of rotation, and therefore represent turbulent structures. Already from the lift coefficient, shown in Figure 5.3, one can see a large deviation for both runs. Although the grid is the same, the classical DES is not able to become turbulent, whereas the IDDES appears to have become turbulent much more easily.

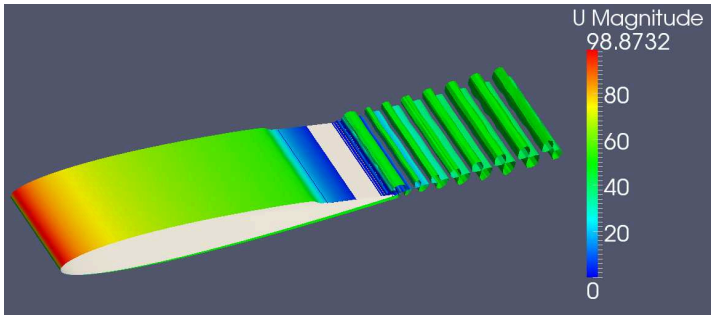

Figure 5.4: Q- isosurface=1E3 colored with velocity. The S-A DES formulation was used as hybrid RANS-LES method

These issues are very interesting and certainly should deserve more attention and elaboration to quantify the potential of each method. It should be wise to investigate the performance of those methods on different meshes, solver settings, boundary conditions and different flow conditions. The problem concerning the GIS and LLM with the original formulation of DES is not wanted and difficult to analyze. The usage of DES requires suitable meshes which are difficult to make and certainly require some experience. Although there are guidelines reported in Spalart (2001) to make DES-suitable grids, it will still not be straightforward. The IDDES was expected to reduce these issues and overcome these stringent demands. As for both models, the transition from the RANS to LES domain will give rise to model errors and uncertainties. Analyzing this transition region is complex and requires special treatment. Now the methodology is chosen, it should be investigated to find the resolutions of the computational grid with respect to the computational methodology, IDDES. More

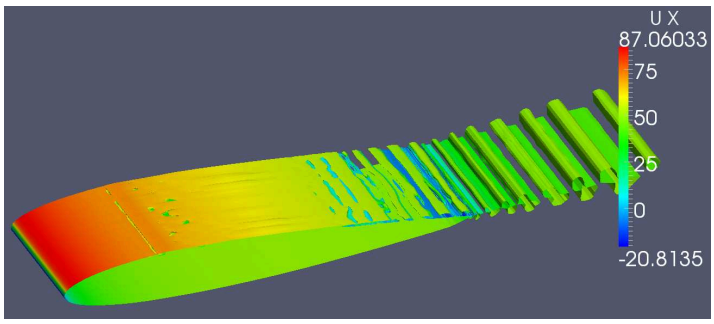

Figure 5.5: Q- isosurface=1E3 colored with velocity. The S-A IDDDES formulation was used as hybrid RANS-LES method

information about this, as well as solver settings and boundary conditions will be presented in next part.

5.3 Preliminary Test Cases

Before the simulations could be carried out with confidence, a series of other preliminary simulations were carried out. In this section, we will present some of them, which are considered to play a crucial role in the decision process. The focus of all those test cases was mainly to obtain a decent computational grid and to find good solver settings. The choice of turbulent model was already motivated in previous section.

5.3.1 Numerical grid

For the purpose of this project, a structured grid with hexahedral elements was chosen. The computational mesh was generated with Pointwise V16.03 Release 4. Building the computational mesh was not easy, and was an iterative procedure. Due to the limited time available, and the stringent demand of computer power, it was not possible to play around with various numerical grids, solver settings, and numerical schemes. Although various meshes were tested, a summary of the process of making a good mesh will be discussed here. A trade-off between the tested meshes resulted in the actual mesh design and a grid convergence study helped to quantify the order of accuracy. Before the numerical grid can be build some main aspects - depending on the turbulence model and computational power- should be considered to generate an appropriate mesh:

- The aero-acoustic noise for subsonic velocities is generated due to the turbulent structures hitting the solid boundaries. To capture the most important effects, a quite high wall resolution is required. The mesh at the trailing edge should be fine enough, since it is expected that the most noise is generated in this region. Note that no inflow turbulence will be used. This would have made the simulations more complex, since new

noise mechanisms would have been appeared and validation would have become more complicated.

- The turbulence models, provided in 2.4.1 requires that in order to resolve the boundary layer accurately, the near-wall resolution must be of the order of $y^+ \leq 1$.
- The growth ratio of the near wall cells(in normal wall direction) should be low and is typically around 1.1. To minimize the cell numbers, a larger stretching is applied for region away from the airfoil.
- While building meshes, special attention is given to minimize mesh non-orthogonality and skewness. A good mesh quality is necessary to obtain accurate results and to reduce the computational time.

Mesh design and settings

In the initial attempts, a rectangular domain as being used in literature Greschner et al. (2010) and Oberai et al. (2002) was considered. Various build-ups were tried. The airfoil was put under seven degrees angle of attack. The problems encountered in such a configuration were mainly due to a high non-orthogonality near the airfoil. As mentioned in chapter 2, high non-orthogonality, meaning low mesh quality, requires an additional correction and often an extra computational loop. Minimizing this can lead to computing savings. Moreover problems were found in the corners at the inlet of the domain as can be seen in Figure 5.6. Here an instantaneous velocity field is shown. The values of velocity at these corners blow up in the unsteady simulations, whereas an acceptable velocity field was found in the steady-state RANS simulations. A clear explanation is difficult to formulate, but it is probably ascribed to conflicting boundary conditions or high non-orthogonality without appropriate correction for it. Here a *fixedValue* at the inlet and *inletOutlet* at the upper boundaries was applied. The specific meaning of these boundary condition is addressed in section 5.4.4.

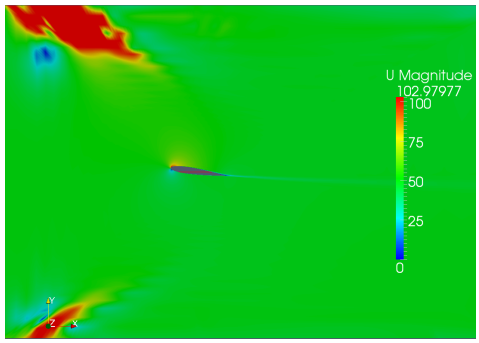

Figure 5.6: instanteneous velocity on a rectangular domain

Unfortunately, building meshes for such rectangular simulation domains was not easy with Pointwise. Also the applied solver settings, specifically the boundary conditions were not suitable for this configuration and could not retain stability although the initial RANS simulation was converged. This was mainly the reason why in further simulations an O-mesh

was used. For the O-meshes, the simulations were found to be more stable and were easier to generate. Therefore the O-mesh design was used in subsequent simulations.

Another issue for finding a good numerical setup was to determine the required resolution along the spanwise length and the amount of cells along the surface. The important thing here is to have enough resolution for the turbulence model to be valid and to have enough acoustic resolution. To speed-up the solutions, a rather coarse mesh was first made. This had a spanwise length of one quarter of the chord $z = 0.25c$. Simulations were only done with a spanwise resolution of 9 and 35 cells in z-direction. Figure 5.7 shows the isosurface of the Q-criterion equal to 1000. A roll up is visible, but the classical break-up in turbulent structures is absent. This is not surprisingly since for this configuration, only a resolution of 9 spanwise cells was used, which is too coarse to obtain turbulent structures. However the simulation proved to be stable which means that the boundary conditions are assumed to be suitable for such a configuration. These solver settings were also used for the final design and will be discussed in more detail afterwards. Moreover a good mesh quality was found, with a limited non-orthogonality. Although the solver settings were found to provide a stable

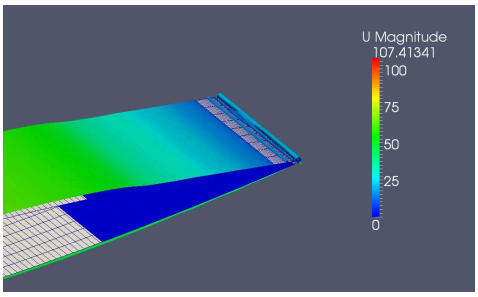

Figure 5.7: Q-isosurface 1000 colored with velocity. The span only contains 9 cells and no turbulent structures are visible.

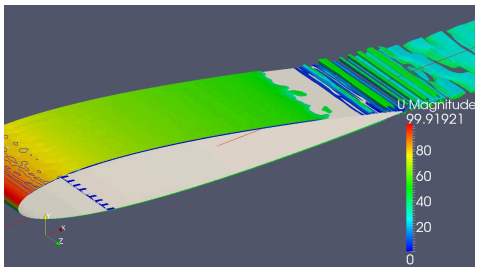

Figure 5.8: Q-isosurface 1000 colored with velocity. The span contains 34 cells and turbulent structures start to appear.

simulations, the resolution is still far from a classical LES simulation. Therefore, the number of spanwise cells were multiplied with a factor of almost four, resulting in 34 spanwise cells. Again, in Figure 5.8 the Q-isosurface of 1000 is shown. Although the boundary layer tries to become turbulent at around a quarter chord, a strong boundary development is not present. At the trailing edge, a role up is present, whereas a break-up of the turbulent structures is not visible. Compared to the case with only 9 spanwise cells, the wake shows a beginning 3D structure.

It was clear that DES simulations needed a much higher resolution, especially in the spanwise direction. To achieve this, the spanwise length was reduced to only $0.1c$ and the number of cells was increased to 50 which leaded to the final grid design. Also such a configurations and resolution as well as the same turbulence model was already proven by Greschner et al. (2010) to work good. Details will be discussed in following section 5.4.

Name	number of cells	cells on suction	cells on pressure	cells in span	cell on TE.	first cell [m]
Coarsest	347620	100	75	15	20	4E-06
Medium coarse	1061760	200	100	25	20	2E-06
Medium fine	1907060	240	130	35	30	1.5E-06
Finest	5938800	370	200	50	40	1E-06

Table 5.1: Overview of the resolutions of different meshes

5.4 Test Cases

5.4.1 Test meshes

A representative view of the solution domain is presented in Figure 5.9. The solution domain is an O-like domain, with the the airfoil located in the center of the domain. Here a front view and a side view are shown. The farfield boundaries are located sufficiently away from the airfoil to improve the stability of the numerical simulation. Therefore the farfield is located at a multiple chord lengths ($11c$) of the airfoil. Below we will take a closer look at the computational grid, and dimensions will be further quantified.

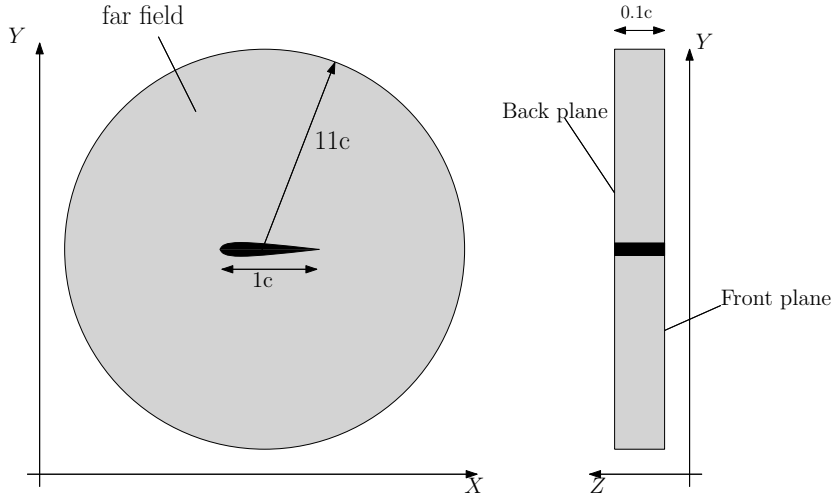

Figure 5.9: Representation of solution domain and boundary patch of the O-mesh.

To come to the final mesh design, four different meshes with increasing mesh refinement were considered and a grid study was performed. All these meshes are build-up similarly, have the same span-wise length, and a far-field at equal distance to the airfoil so that these influence can be omitted. Table 5.1 presents an overview of all the resolutions of the considered meshes. A global overview of the simulations which will be considered further is given in E.

For the finest mesh, the airfoil has around 370 cells on the suction side and only 200 on the pressure side. The mesh is clustered near the leading and trailing edge to capture all the most important phenomena. The airfoil has on both sides 50 cells in the spanwise direction. Therefore, we end up with a coarse LES-like grid on the suction side, and a RANS like grid on the pressure side. The trailing edge has a height of $2.5mm$ and contains 40 cells. The first cell normal to the wall was located at 1×10^{-6} to maintain a $y^+ < 1$ over the whole airfoil. The actual and most refined mesh contains of around nearly 6 million cells. A more detailed view of the mesh in the near-field around the airfoil and the trailing edge is depicted in Figures 5.10 and 5.11 Although the final mesh is a product of many attempts, it is still far from optimal. The O-mesh requires quite a lot of cells, because all the cells on the airfoil are also extruded to the farfield. The mesh in the wake could be too coarse to capture all the turbulent flow phenomena. Unfortunately, local refinement in this wake area without a large increment in cell amount and preserving mesh quality was hard to achieve. However, a grid refinement in the wake would probably not make a lot of difference for the acoustic computations, since they will only take the pressure fluctuations into account. This effect can be investigated in further research.

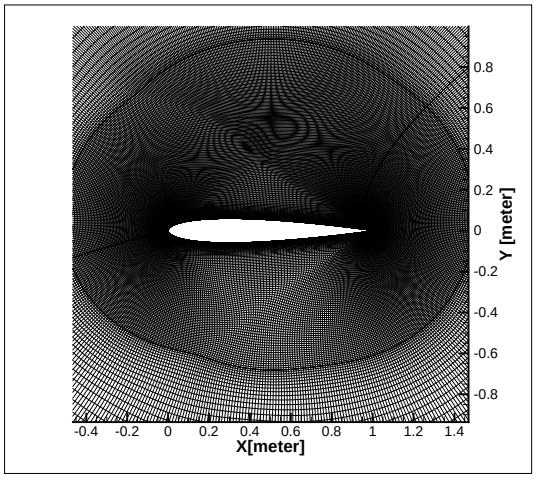

Figure 5.10: Close up of fine grid around NACA 0012.

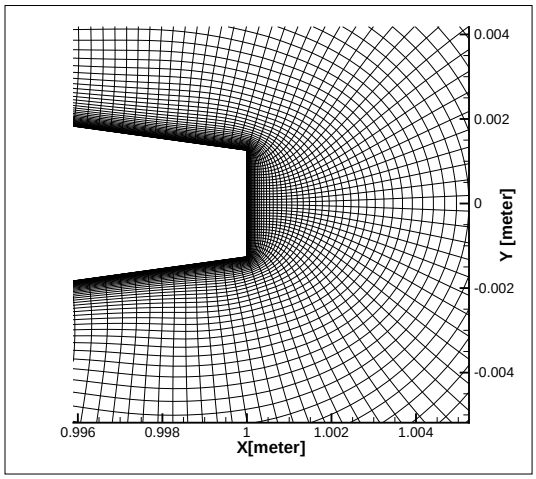

Figure 5.11: Close up of grid around trailing edge for the fine grid.

5.4.2 Preliminary results and grid study

With the previous mentioned test cases, one can obtain some preliminary results, which can give already some basic insight in the numerical simulation, the requirement on mesh resolutions and convergence. A NACA 0012 profile under zero angle of attack, a freestream velocity of $70m/s$ and a Reynolds number of 1 million is considered for these test cases. We will first investigate some basic quantities like the lift coefficients and drag coefficients for these simulation cases. The lift coefficients for all the test cases is shown in Figure 5.12, whereas the drag coefficient is depicted in Figure 5.13. The amplitude of the force coefficients fluctuate, till they reach a maximum at a physical time of around 0.08 seconds. Afterwards, the amplitude decreases again, and fluctuate around a certain mean slightly above 0, so that

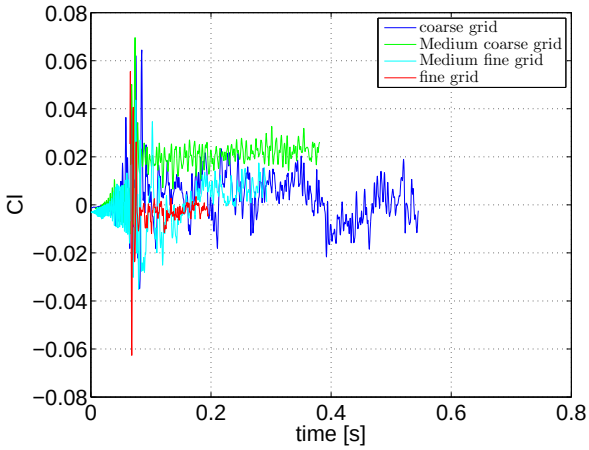

Figure 5.12: Lift coefficients for four different cases

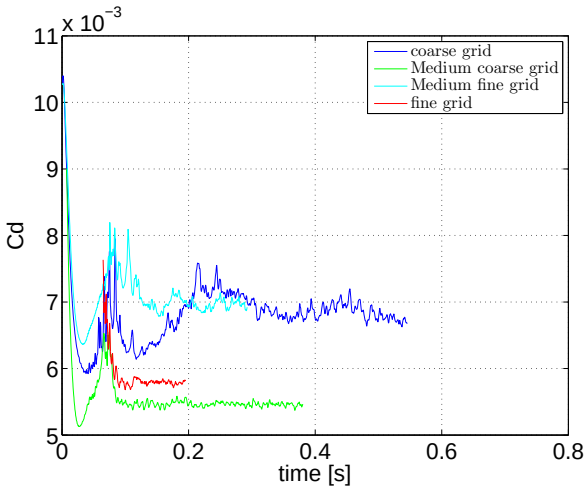

Figure 5.13: Lift coefficients for four different cases

the averaging process can start. One can observe from Figure 5.12 that for the coarsest mesh, the fluctuations are the largest whereas for the most refined the amplitude of the fluctuations becomes minimal. Since the NACA 0012 profile is a symmetric profile and the angle of attack is zero, one should expect a Cl value of around 0. The value for the drag coefficient also approximates the reference value of 0.0055 reported in Sheldahl and Klimas (1981).

Note that here an unsymmetrical mesh - more cells along the suction side then on the pressure side - was considered. If the mesh was symmetric, it would probably give anyway this value, even when a coarse mesh was considered. So therefore, one has to be carefully to make conclusions and an additional analysis on another angle of attack would be advisable.

Next some flow fields of the refined, and medium coarse test cases will be discussed. The averaged velocity field of the medium coarse case shows some unsymmetrical behaviour near the trailing edge as is shown in Figure 5.14. The boundary at the suction side is thicker than on the pressure side and covers a larger region. It is possible, that the difference in mesh design on both sides of the airfoil cause this behaviour, suggesting that the turbulence model depends on the mesh spacing. A possible reason can be that the grids are not fine enough to support LES content, or that not enough turbulent fluctuations are provided by the RANS mode. More detailed analysis is required to have a full understanding of this phenomenon. Regarding the finer mesh in Figure 5.15, a discrepancy between both sides is still noticable. Here, the pressure side of the airfoil, having a lower resolution, has a thicker boundary layer.

Figure 5.16 and 5.17 show the time averaged pressure coefficient Cp and skin friction coefficient Cf for both runs. The Xfoil data for the Cp quantity is also shown. The symmetrical airfoil NACA 0012 at 0 degrees angle of attack is considered, hence one expects a symmetrical behaviour in the pressure coefficient as well. The global behaviour compares quite good with the pressure distribution provided with Xfoil. For the medium coarse case there is a clear deviation from Xfoil, near the trailing edge. There is also a difference in distribution

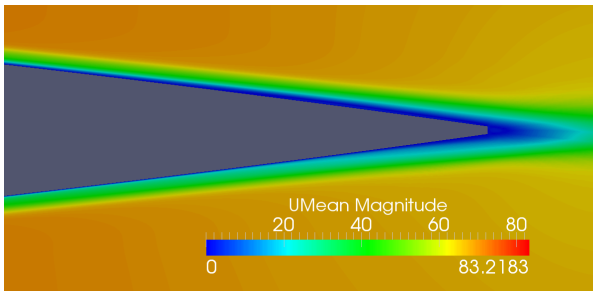

Figure 5.14: Mean velocity @ TE for medium coarse mesh and the unsymmetric behaviour along the pressure and suction side

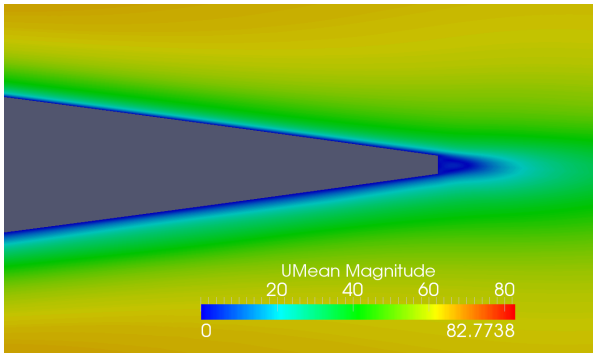

Figure 5.15: Mean velocity @ TE for the fine mesh and the unsymmetric behaviour along the pressure and suction side

between the suction and pressure side noticable, as was also seen from the velocity field, shown in Figure 5.14. The difference in mesh grid between both side, and the behaviour of the turbulence model on it could cause these differences, resulting in different boundary layer development. For the refined case these deviations are less pronounced although they are present. At around 60% of the chord, a bump in the pressure distribution is present in the Xfoil data, indicating a boundary layer transition. A same transitional behaviour is observed for the simulation with the fine mesh. However, the bump is located more to the leading edge. This can indicate that the free transition is not captured completely for this simulation. The

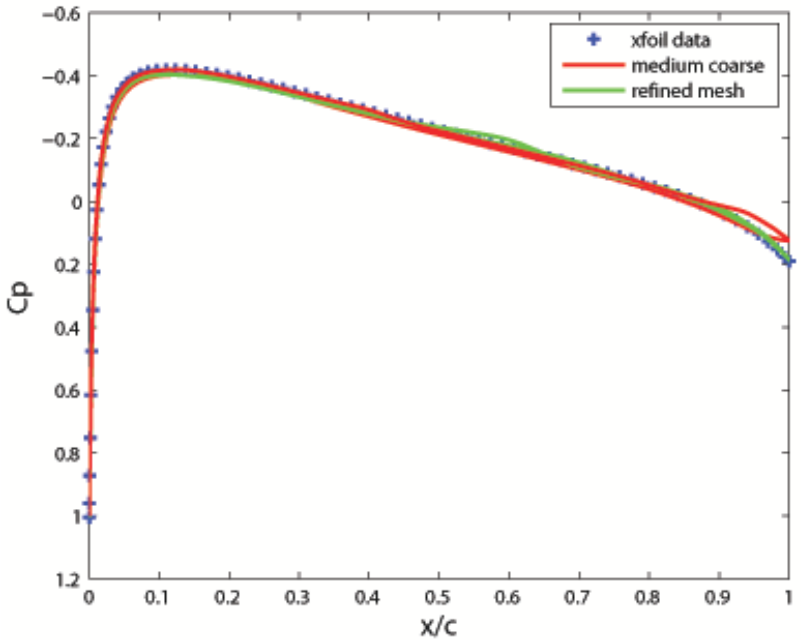

Figure 5.16: Pressure coefficient for the medium coarse and refined case for zero angle of attack. Xfoil data is also added for comparison purposes.

graphs for the skin friction even show a clearer difference between both simulations. Also the skin friction on both the pressure and suction sides differ from each other. A bump in the skin

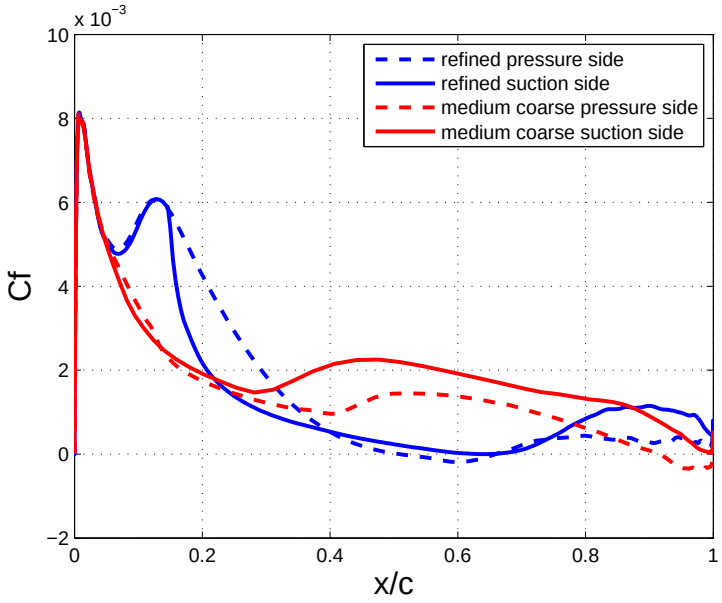

Figure 5.17: Skin friction for the medium coarse and refined case for zero angle of attack.

friction coefficient at around $0.1c$ indicates the transition region from a laminar to a turbulent boundary layer. This bump is not present in the coarse mesh, but is rather smoothed out over a larger part of the airfoil. Near the trailing edge an increment of the value of skin friction on the suction side can be noticed, implying the turbulent activity. The similar increment, although less strong is observed for the pressure side. Note that the value for skin friction is around $0.6c$ below zero, indicating a small separation zone. A big difference is noticed between both simulation runs. It reflects the importance of the grid and the need for a grid convergence study.

Velocity profiles for different positions on the airfoil are presented in Figure 5.18. Profiles are normalized with the mean outer velocity and a comparison is made between the pressure and suction side. The profiles in the laminar region on the first half of the airfoil are comparable. The shape of the profiles start to alter at around $0.4c$ and discrepancies in shape are clearly visible at $0.5c$. The profiles in the turbulent region again have comparable shapes, but the values in velocity are different. Figure 5.19 shows the Q-isosurfaces for a value of $1E05$ which are colored with the magnitude of the mean velocity. With the Q-criterion it is easy to visualize the flow structures and coherent vortices, present in the boundary layer. It is observed that the transition to a break down of these structures covers a large part of the chord. Near the trailing edge, this break-down is clearly visible. Even small scales can be captured, suggesting that the mesh grid is sufficient fine. Figure 5.20 demonstrates the quantity p'^2, directly obtained by OpenFOAM in a log-scaling. This quantity represents the instantaneous pressure value with respect to the mean pressure. These fluctuations are formed by the turbulent structures shedding over the trailing edge. Near the trailing edge these values are the largest which indicate that in this region the noise sources are located. Hence it confirms the appearance of trailing edge noise.

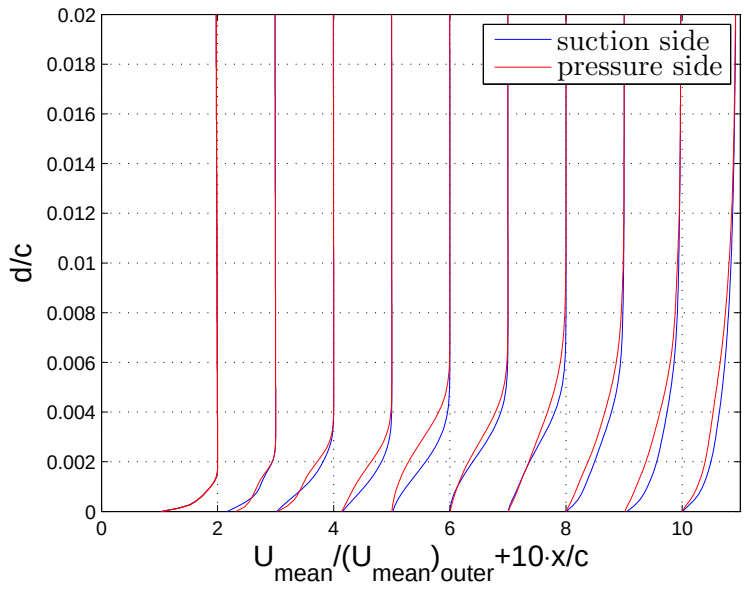

Figure 5.18: Comparison of velocity profiles for the pressure and suction side (refined mesh). Normalization is performed with respect to the outer velocity. Velocity profiles are presented for different positions on the airfoil.

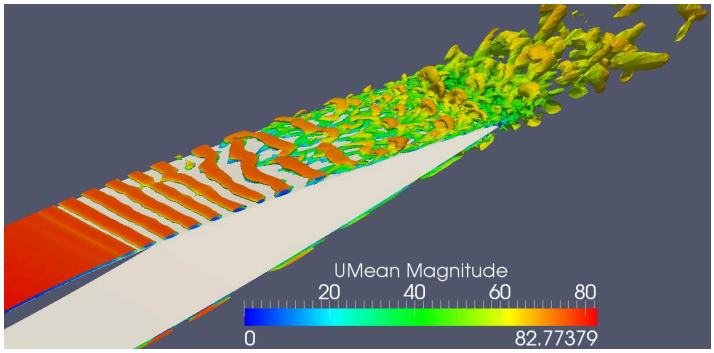

Figure 5.19: Q-isosurface for 1E-05, colored with mean velocity magnitude

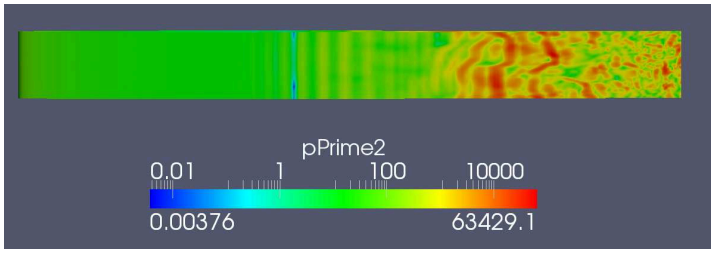

Figure 5.20: pressure fluctuations along the suction side

Some important boundary layer characteristics are summarized in table 5.2. They correspond to the velocity profiles located near the trailing edge. The displacement thickness, momentum thickness and shape factor are provided for both the pressure and suction side.

		$\delta^*[m]$	$\Theta[m]$	H
medium coarse:	suction	0.0088	0.0055	1,6
	pressure	0.01	0.0058	1.72
refined:	suction	0.012	0.0075	1.6
	pressure	0.01	0.0077	1.30

Table 5.2: overview boundary layer characteristics for medium coarse and refinedgrid

The displacement quantity is an important characteristic and will later on be used in the scaling of the acoustic results in order to compare the simulated acoustics and reference data. These boundary parameters are derived from the conservation of mass and momentum and are expressed in the equations

$$\delta^* = \int_0^{y\to\infty} \left(1 - \frac{u}{U_\infty}\right) dy \tag{5.4}$$

$$\theta = \int_0^{y\to\infty} \frac{u}{U_\infty}\left(1 - \frac{u}{U_\infty}\right) dy \tag{5.5}$$

The ratio between the momentum thickness and the momentum thickness determines the shape factor $H = \frac{\delta^*}{\theta}$ of the boundary layer.

5.4.3 Grid Convergence Study

First, the (spatial) grid convergence based on the lift coefficient is provided and presented in Figure 5.21 for the four meshes. The order of convergence observed from these results, is approximately equal to 2, which is also the theoretical order of convergence of the discretization of Navier Stokes equations. If no discretization errors would have been made, the model errors (governing equations, turbulence modeling) will remain. Differences are probably due to grid issues, limited averaging, turbulence modeling and other factors. Moreover, it can be seen that for the coarsest case, the solution is outside of the asymptotic range of convergence, and has a lower error compared to the finer grids. Note that a small value, 0.001 for Cl as reference value was used in the grid convergence study, to approximate the theoretical value of zero for Cl.

5.4.4 Model Details and boundary conditions

Physical boundary conditions such as the wall, farfield and initial conditions which include the known field values prior to the first time steps of the calculations are necessary to prescribe a problem. Here, we will shortly discuss the applied boundary conditions. The test cases have three different boundaries, namely farfield, the front-and-back planes and the airfoil as given in Figure 5.9. On all these boundaries we have to provide the conditions of a set of quantities depending on the chosen turbulence model. For the Spalart-Allmaras, one have to give: the *velocity*, *pressure*, the turbulent variable *nuTilda* and the subgrid scale viscosity

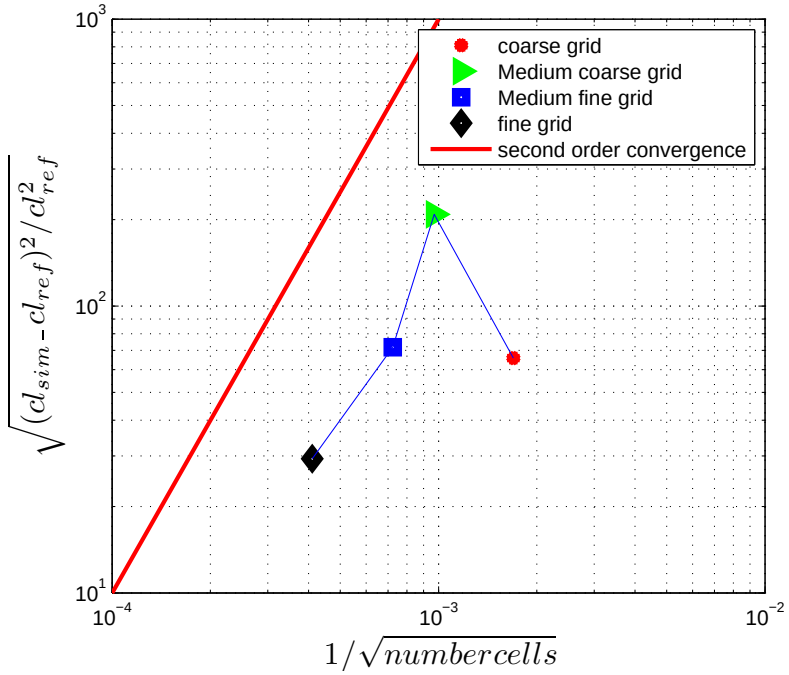

Figure 5.21: Grid Convergence based on Lift Coefficients

nuSgs. There are 3 commonly used basic boundary conditions: fixed value, zero gradient and cyclic boundaries. The fixed value boundary condition prescribes the value of the generic variable ϕ at the face of the boundary. The zero gradient boundary puts the normal gradient on the boundary to zero. Cyclic boundaries are used to mimic an infinite flow behaviour. The value of the faces are physically connected in this way. Applying the cyclic boundaries to the front-and-back planes enables us to mimic the behaviour of a larger spanwise length and retain the physical phenomena.

Farfield

The *inletOutlet* condition is applied for the velocity and turbulent quantities at the farfield, whereas for the pressure the *outletIntlet* condition is applied. Basically the *inletOutlet* condition is zero gradient unless the flow is inward in which case it is fixed value (inletValue). Moreover the *outletInlet* is zero gradient if the flow is inward and fixed value (outletValue) if the flow is outward. The values of velocities and the other quantities are summarised in table 5.3.

Wall

For the wall, here the airfoil, the no-slip boundary condition is appropriate. So, a *fixed value* boundary condition, setting a constant uniform velocity $\bar{\mathbf{u}} = 0$. Also the turbulent variable *nuTilda* is equal to zero. A zero gradient is considered for the pressure. For the *subgrid scale viscosity* a *nuSgswallfunction* is applied. The LES wall function in OpenFOAM assumes an

RANS initialisation			
	Farfield	*Wall*	Front and Back planes
Pressure	outletInlet value: 0	zeroGradient	Cyclic
Velocity	inletOutlet value: eg. [70 0 0]	fixedValue value: 0	Cyclic
nut	inletOutlet value: 2.8E-4	nutSpalartAllmaras-WallFunction value:0	Cyclic
nuTilda	inletOutlet value: 2.8E-4	fixedValue value: 0	Cyclic

IDDES			
Pressure	outletInlet value: 0	zeroGradient	Cyclic
Velocity	inletOutlet value: eg. [70 0 0]	fixedValue value: 0	Cyclic
nuTilda	inletOutlet value: 2.8E-4	fixedValue	Cyclic
nuSGS	zeroGradient	nuSgsWallFuction value: 1E-10	Cyclic

Table 5.3: Overview of the boundary conditions for all patches and variables with respect to the S-A model. Both conditions for RANS and IDDES are presented

instantaneous correlation between the the velocity at the first off-the-wall grid point and the wall shear using an assumed velocity distribution.

An overview of all the boundary conditions is given in table 5.3.

5.4.5 Simulation Details

All the simulations are initialized using first a potential flow, followed by a steady-state RANS. Several flow-through times are necessary to obtain the typical turbulent flow structures. The computation for the averaging purposes and the storing of the pressure data along the airfoil was initiated when enough turbulent structures were present. The averaging time should be long enough to obtain appropriate data. For the reproduction of the aero-acoustic noise sources, an averaging of at least 10 cross-over times is typically applied. The maximum Courant number was kept below one to preserve stability. Owing to the high velocities and

fine mesh sizes, a very small timestep was used. For the fine mesh it is chosen to take $\Delta t = 2\times10^{-6}$s, which demands that the simulations be averaged for approximately 70000 timesteps. This was practically impossible in this thesis and therefore only data over 50000 time steps was considered. The files which controls the timestep and writeintervals, configuration of the solver settings and the numerical schemes corresponding to these testcases, were discussed in 3.1.1 and presented in Appendix A, B and C.

5.5 Verification and Validation of Acoustics

In previous section it was demonstrated that the solution has a second order convergence based on the lift coefficient. Although this grid study is very usefull and inevitable for CFD simulations it does not provide any information about the convergence of the acoustic results. Therefore, this section demonstrates the grid convergence based on the sound pressure level as parameter. First information of the reference benchmark is provided. Next, a test is presented to check the implementation of the Curle's formulation.

5.5.1 Reference details

The NACA 0012 airfoil is selected as the test case in this thesis. The NACA 0012 airfoil is considered as a good model for trailing edge noise predictions. This profile has the advantage that it has been studied extensively. Besides the fact that the aerodynamic quantities can be verified with experimental and numerical results, its acoustics are also studied in detail. A paramount of acoustical data was collected at the aero-acoustic wind tunnel of the NASA Langley Research Center (Brooks et al., 1989). Brooks measured seven NACA 0012 airfoil blade sections of different sizes (chord lengths from 2.5 to 61 cm) tested at wind tunnel speeds up to Mach 0.21 (Reynolds number up to 3×10^6) and at angles of attack from $0\,°to\ 25.2\,°$. He also tested the effect of blunt trailing edges, which give rise to tonal noise peaks. Another benchmark is provided by Oerlemans and Migliore (2004). A photograph of the typical experimental set-up of Brooks is given in Figure 5.22.

The acoustic measurements were conducted with a set of 8 microphones. The sound pressure levels (SPL) for the an observer at $1.22m$ on top of the trailing edge are reported in terms of one third octave. The sound power is expressed in one third octave bands to easily see the composition over the frequency range and to make it possible for comparison. Frequency ranges which each octave is divided into one-third octaves with the upper frequency limit being 2 1/3 (1.26) times the lower frequency.

Experimental research is carried out extensively on trailing edge noise. However the experiments and CFD simulations can not be compared one to one. For instance, the spanwise length of the experiments cannot be reproduced in current CFD modeling. Fortunately Brooks et al. (1989) developed some spectral scaling laws for the five different self-noise mechanisms. With such a spectral scaling, it is possible to compare trailing edge noise data, acquired by different measurement techniques, different test facilities and different conditions. The simulations

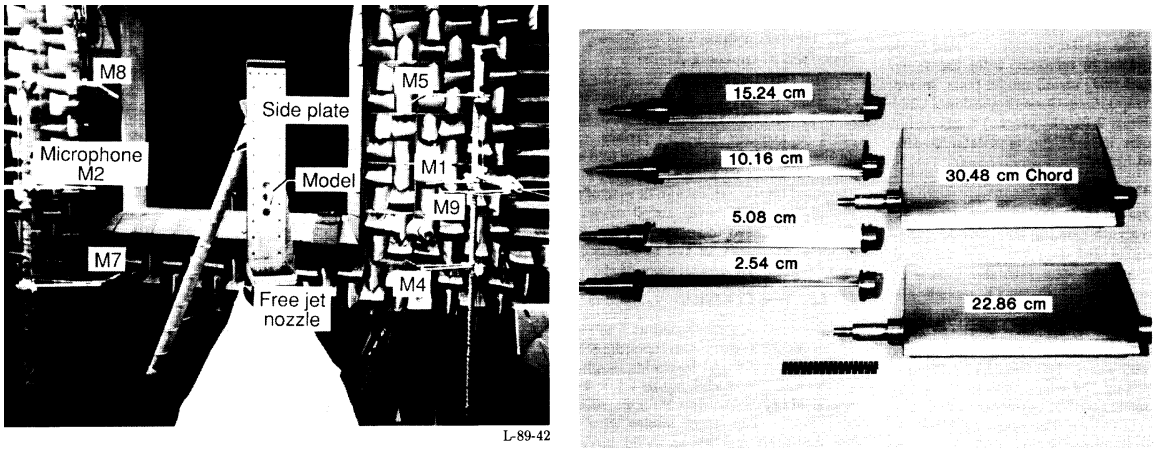

Figure 5.22: Setup from acoustic tests according to Brooks

were conducted with different settings compared to the reference data, so that the scaling laws should be applied. The form of the spectral scaling and normalization for a one third octave band is given as:

$$\text{Scaled } SPL_{1/3} = SPL_{1/3} - 50\log_{10} M_\infty - 10\log_{10}\frac{\delta_1 b}{r_e^2} \tag{5.6}$$

$$St = \frac{f_m \delta_1}{U_\infty} \tag{5.7}$$

This scaling is based on the freestream Mach number M_∞ and influences the scaling quite strong. The displacement thickness δ_1 is used as a turbulent boundary layer characteristic, or relevant length scale and affects both the SPL and normalized frequency. The boundary layer thickness can be computed from the velocity profiles near the trailing edge and were tabulated in table 5.2. The value r_e resembles the observer distance. The quantity b refers to the spanwise length. The measured or computed frequencies are besides the boundary layer thickness also scaled with the freestream velocity.

5.5.2 Validation of Curle

The Curle's acoustic analogy will be used as the CAA method to provide the noise predictions in the farfield. Unfortunately no verified code for this analogy was available and was eventually self-made. To check the implemented code, the time signal of a source was assumed to be known. For a simple signal, the pressure fluctuations can be described by an analytical solution by Howe (1998):

$$\frac{x_i}{4\pi c_0 |\mathbf{x}|^2}\frac{\partial F_i}{\partial t}\left(t - \frac{|\mathbf{x}|}{c_0}\right) \tag{5.8}$$

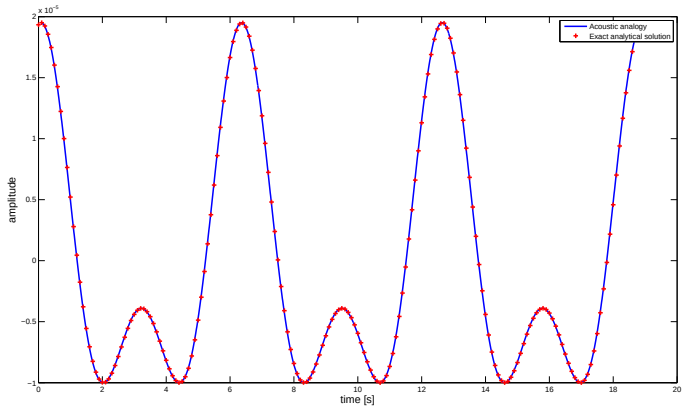

Figure 5.23: Comparision between exact solution and simulated

where in principle $F_i(t) = \oint p'_{ij}(\mathbf{y}, t)\, n_j ds(\mathbf{y})$ is the net force exerted on the fluid by the rigid body. Since it is difficult to test the implementation with the fluctuations on an airfoil surface, one can simply assume p'_{ij} to be a continuous functions so that it can simply be solved analytically. In this test case, one simply assumed this function to be equal to:

$$p'_{ij}(\mathbf{y}, t) = \frac{3}{2} \cdot \sin(t) + \sin(t) \cdot \cos(t) \tag{5.9}$$

for which an analytical solution easily can be found. Figure 5.23 shows the exact analytical solution and the approximated one of the Curle's acoustic analogy. It is clear that the implementation was done in a proper way since both approaches are matching perfectly. Note that for the real case the pressure values are calculated during the simulation and the normal vectors are known from the mesh. This was verified while implementing the code. The code is provided in Appendix D.

5.5.3 Acoustics

To compute the farfield noise, the Curle formulation for the compact source body given in equation 5.10 is used. For convenience the compact formula is restated here:

$$\begin{aligned} p'(\mathbf{x}, t) \cong & \frac{x_i x_j}{4\pi \|\mathbf{x}\|^3 c_0^2} \frac{\partial^2}{\partial} \int_V [T_{ij}]\, dV(y) \\ & - \frac{x_j}{4\pi \|\mathbf{x}\|^2 c_0} \frac{\partial}{\partial t} \int_S p n_i dS \end{aligned} \tag{5.10}$$

From equation 5.10, the radiated sound pressure at any location is computed by the time derivative of the calculated temporal variation of surface pressure and integrating along the surface. Note that the integral is evaluated at the retarded time. As already was motivated, the contribution of the Lighthill tensor in a volume dV will be neglected. For current Mach regimes, the sound production in a volume will be rather small compared to the surface

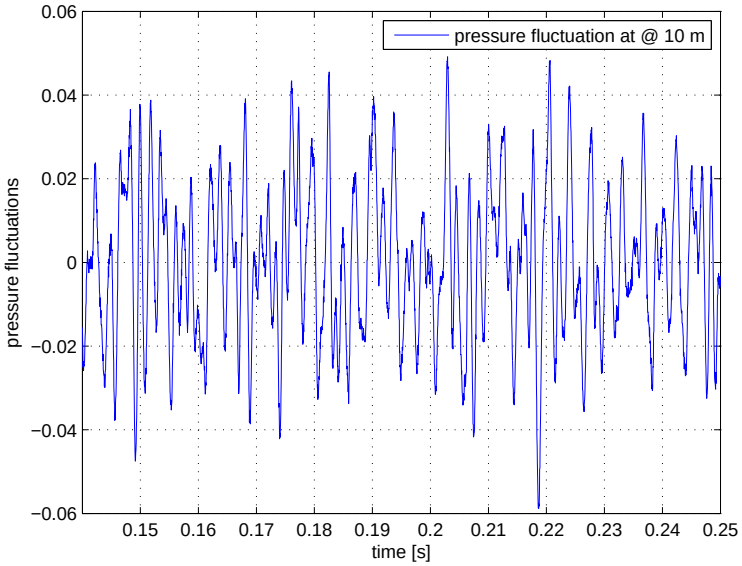

Figure 5.24: Pressure fluctuations for an observer at 10 m above the trailing edge

contributions. In order to do this, an algorithm is written in Matlab® which is added in Appendix D. The temporal pressure data and the normals are provided by OpenFOAM.

The surface pressure data is recorded from the moment that the boundary layer is turbulent. Recording all these data for every timestep (2×10^6) is very expensive and not necessary to predict the most important frequencies ranging from $100Hz$ to $3000Hz$. Note that at least a few flow through-overs are necessary to have a statistical good solution. The pressure data is recorded each $4 \times 10^5 s$, which is assumed to be sufficient and comparable to literature (Greschner et al. (2010)).

Figure 5.24 shows the pressure fluctuations as computed with equation 5.10 for an observer which is located directly above the trailing edge at a distance of 10 meters. Note that the pressure fluctuation signal corresponds to the refined case. The signal covers $0.12s$ in physical time and contains only 6000 samples. This is the equivalent of around 9 cross-over times. More samples would have been desirable, but was difficult to achieve due to limited resources. From the pressure signal it is possible to compute the sound power level, stated as:

$$SPL = 20 \log_{10} \frac{p'_{rms}}{p_{ref}} \tag{5.11}$$

with the reference pressure $p_{ref} = 2 \times 10^{-05}$. In order to decompose the pressure fluctuation signal into components of different frequencies, a Fast Fourier Transform (FFT) in Matlab® was applied. The consistency of the pressure signal can be checked by performing a FFT on different parts of the time signal. Each part of the signal should result in the same spectra, so containing the same information. Figure 5.25 shows the SPL's generated from the first, the last part of the signal and the whole signal. The SPL curves match in an acceptable level. A same trend and SPL values are observed for all the curves, proving the signal to be

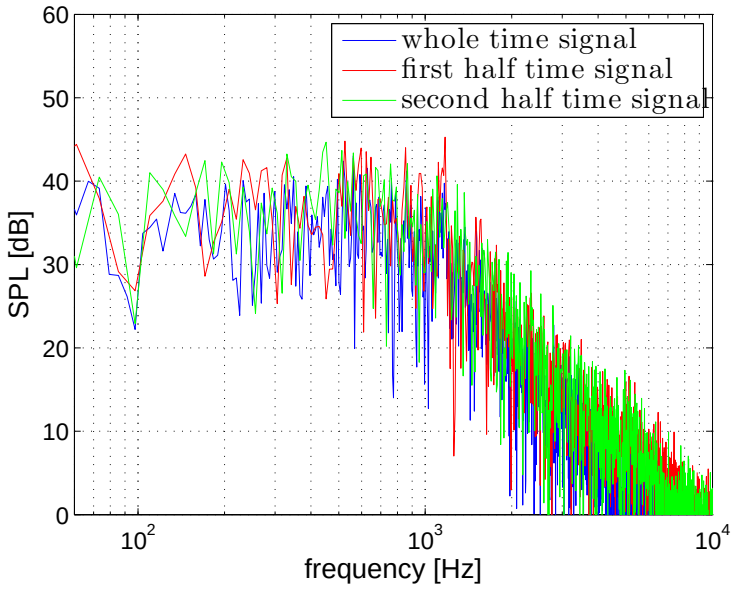

Figure 5.25: SPL of different timesignals

consistent.

Instead of the normal SPL, the third octave $SPL_{1/3}$ is used. Before a comparison with experiments can be made, the scaling laws of equations 5.6 and 5.7 are applied. An acoustic analysis was performed to the medium coarse, medium fine and refined case. Note that the coarsest mesh was not considered here. The boundary layer thickness of each simulation is summarized in table 5.3 and is used in equations 5.6 and 5.7. The freestream velocity is 70 m/s, which compares to a Mach number of $M = 0.20$. The spanwise length for all the simulation runs is $0.1m$. Moreover the position of the observer is fixed at $10m$ directly above the trailing edge.

Figure 5.26 presents a comparison of the simulated $SPL_{1/3}$. The BPM-model together with other references of Herr et al. (2010) are also included. The BPM-model is an empirical airfoil self noise prediction method based on boundary layer thickness at the trailing edge proposed by Brooks et al. (1989). This well known empirical model was derived from experimental measurements from a series of aerodynamic and acoustic tests on two and three-dimensional NACA0012 airfoil models at different Reynolds numbers. Brooks determined (based on the experiments) for each noise mechanism a formulation which provides the frequency and magnitude of the SPL.

A first observation is that there is a strong improvement of the fine mesh with respect to the medium coarse. Two aspects can be noticed. First the magnitude of SPL decreases with each mesh refinement. The top of SPL has dropped almost $10dB$ because of the mesh refinement only. This represents the importance of the computational mesh and the need for a grid study. The peak value of SPL of the fine mesh compares properly to the reference values. Moreover the overall trend of the SPL graph is captured decently. However a bump in SPL

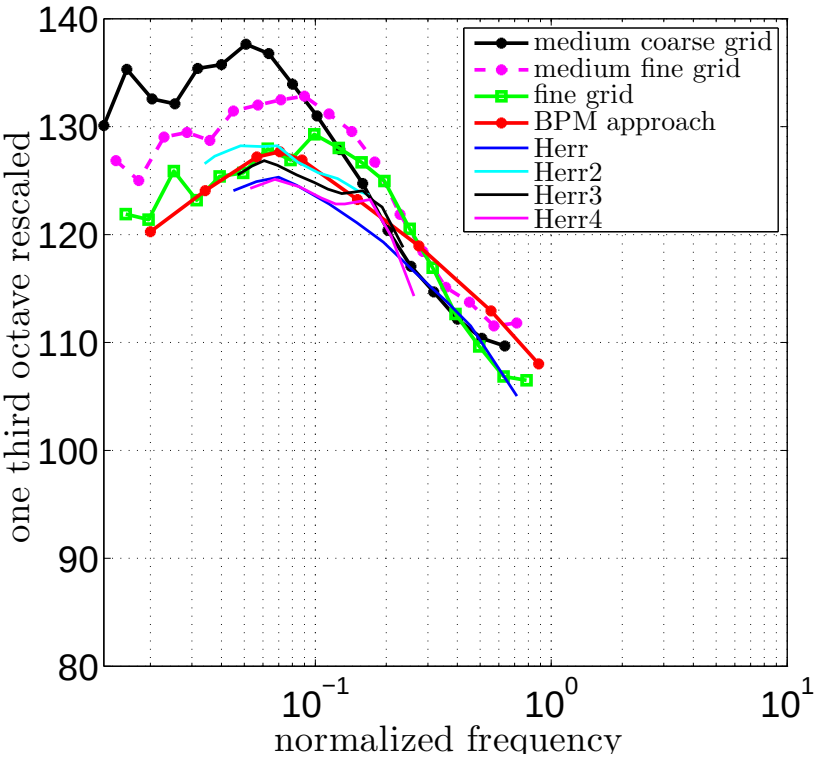

Figure 5.26:

at a Strouhal number of around 0.1 is noticable, whereas this was not observed for the coarse meshes. A second observation is that the top of the SPL also makes a small shift in Stouhal number with each mesh refinement.

Based on this results, one can again perform a grid convergence study. The grid study is now based on the Overall Sound Pressure Level (OASPL). Before, a grid study was done with only one parameter, the lift coefficient Cl. Here, one has to account for the Strouhal number and the magnitude of SPL. The OASPL is the sum of the contributions over a range of frequencies. The contributions to the OASPL were taken for a range of normalized frequencies between 0.03 to 0.3, since this is the important region for accurate noise predictions. It is expected that in this range the results are reliable. The lower frequency bound corresponds to the larger structures (long time intervals) in the time signal and to the large turbulent structures in the flow. Therefore to be reliable, they require a certain amount of time samples. It can be assumed that the larger structures have a time scale equivalent with one flow overtime. For these simulations the flow overtime is equal to $0.014s$. The higher frequencies correspond to the small scaled structures in the boundary layer flow. Sufficient resolution, both in space and time is required for an accurate prediction.

Figure 5.27 displays the grid convergence study for which the BPM-model was used as the reference curve in this grid study. The red line refers to second order convergence. The grid convergence study was based on the three cases: medium coarse, medium fine and refined case, each denoted with a different color. The simulations seem to reach a convergence which

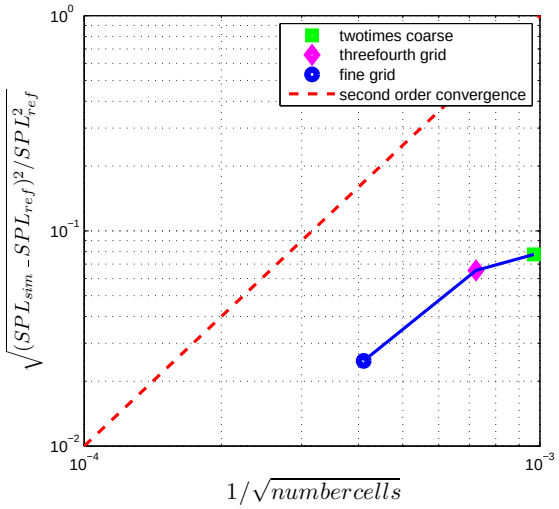

Figure 5.27: Grid convergence study based on SPL

is slightly lower as the second order convergence. This is an acceptable result for the sound pressure level, and provides confidence in the simulations and the hybrid approach. A finer grid could probably increase the accuracy as the discretization is lowered. Note that further refinement with a ratio of 2 results in a multiple of 8 times the amount of cells. Unfortunately this would have been beyond the limits of our resources.

An acceptance test for solution verification is the observed order of accuracy. Roy (2005) states that the observed order of accuracy is the accuracy that is directly computed from the code output for a simulation or set of simulations. The order is adversely affected by a bunch of mistakes such as code errors, bad numerical algorithms. There are two ways to compute the observed order of accuracy. The first method can obtained when the exact solution is known and therefore only two simulations are required. The second method does not require an exact solution, but demands three numerical solutions. Both methods will be elaborated since 3 numerical and an 'exact' solution is available.

When the exact solution is known, the observed order of accuracy p can be computed as:

$$p = \frac{\ln \frac{DE_2}{DE_1}}{\ln r_m} \tag{5.12}$$

where r_m is the grid refinement factor $r_m = h_2/h_1$ (the ratio between the coarse and fine mesh element size). The values DE_2 and DE_1 are the differences between the numerical solution and the exact solution for the coarse and fine mesh. In this context one can assume the BPM-model as an 'exact' solution, and an observed order of accuracy can be derived from the medium fine and fine meshes. The peak values of the SPL curves are used for these computations and are translated back to Pascals to calculate DE_2 and DE_1. The SPL of the exact solution compares with 45 Pa, whereas the values for the medium fine and fine mesh were 95 Pa and 55 Pa. Consequently, the errors DE_2 and DE_1 are 50 Pa and 10 Pa. The grid refinement factor is based on the ratio of the volume changes between the fine and coarse grid. A representative measure to compute the (element size) volume for each mesh can be

based on the volume for the first cell height and spanwise length. Therefore a grid refinement factor corresponding to the medium fine and fine mesh was calculated by:

$$h = \frac{y_{mediumfine}}{y_{fine}} \times \frac{(cells\,in\,span)_{fine}}{(cells\,in\,span)_{mediumfine}} = \frac{1.5E6}{1E6}\frac{50}{35} = 2.2 \tag{5.13}$$

These values with respect to the meshes can be found in table 5.1. Based on the calculated parameters, following observed order of accuracy can be achieved:

$$p = \frac{\ln \frac{50}{10}}{\ln 2.2} = 2.04 \tag{5.14}$$

Assuming that the exact solution is not known one needs three numerical solutions on different meshes to compute the order of accuracy. Because each mesh refinement doesn't have a constant grid refinement, one has to solve equation 5.15 to compute the observed order of accuracy.

$$\frac{f_3 - f_2}{r_{23}^p} = r_{12}^p \left(\frac{f_2 - f_1}{r_{12}^p - 1} \right) \tag{5.15}$$

The variables f_1,f_2 and f_3 are the simulated quantities for the fine, medium fine and medium coarse mesh. The values are 55Pa, 95Pa and 180Pa respectively. The grid refinement ratio's are calculated as before and equals $r_{12} = 2.2$ and $r_{23} = 1.8$. Based on a program in Matlab® one can find an observed order of accuracy of 1.56. Both these calculated values are acceptable.

The compact formulation used in this context only takes the contribution of the pressure on the airfoil into account. As a consequence, the source will radiate the sound pressure as a dipole. This is also shown in Figure 5.28 and clearly behaves as a dipole as expected. It shows the directivity for the frequencies of $500Hz$, $800Hz$, $1250Hz$ and $2000Hz$ for an observer location at 10 meters. Note that the scattering in different directions is more contributed to quadrupoles and especially for the higher frequencies. For a more advanced directivity with the typical lobes, one requires a more complex CAA method such as for example the LEE.

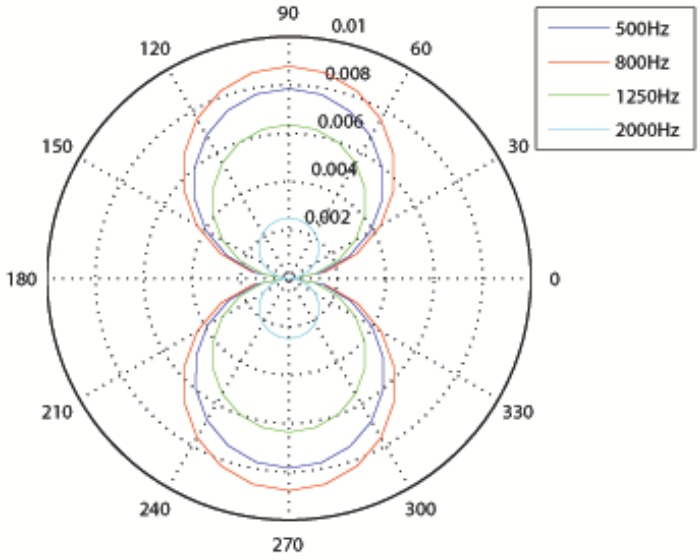

Figure 5.28: Directivity at 10 meter for different frequencies with respect to the fine mesh. The polar plot reveals the dipole nature of the noise sources.

5.6 Interim Summary

- A flat plate flow was considered to check the implementation of the S-A models. It showed comparable features with the DNS reference.
- A motivation for the choice of turbulence model was provided. The IDDES resulted in the most reliable approach and will be used in further simulations.
- Good convergence was achieved with respect to four different meshes. A grid study was based both on the lift coefficient and SPL. Unsymmetrical behaviour was noticed, which indicate the effect of the mesh on the IDDES simulations.
- The refined case showed acceptable results with respect to the reference data and consistency in the time signal was checked.
- The typical lobes in the directivity plots are absent. A more advanced CAA method is required for this.
- The results which were shown in this chapter confirm the ability of the hybrid approach to do noise predictions, and motivate its use for further research.

Chapter 6

Results

In previous chapter, a suitable configuration and setting for the NACA 0012 with zero incidence angle was investigated. A grid study based on the lift coefficient and sound power spectrum showed acceptable convergence. This chapter presents the results of the different airfoil configurations. Moreover the results are as much as possible compared to experimental or numerical data. First the different configurations are discussed. Afterwards, a validation of the aerodynamic quantities and acoustics is considered.

6.1 Description of the airfoil configurations

Several experimental test cases were attractive for this thesis. The flow conditions are chosen in such a way that they could represent operating conditions. Wind turbine blades typically operate in the low Mach regime and under different angles of attack. In this thesis the freestream flow velocity is set to a fixed $70m/s$. The Reynolds number, based on the chord length, is equal to $Re_c = 1 \times 10^6$. The chord length of the airfoil profile is one meter like in previous chapter. Three different airfoil configurations are discussed in the remainder of this chapter. For the first two cases the angle of attack was $7\,^\circ$. Hence, little separation is expected, which can be very challenging for the turbulence model to make an accurate prediction. Furthermore, for the first case a clean configuration was considered, whereas the influence of the presence of a turbulence trip is considered in the second case.

The last configuration is more challenging, as the influence of a blunt trailing edge is explored. This case is only tested for a zero angle of attack and in clean configuration. This last case will examine the capabilities of the turbulence model to simulate a flow with a large separation zone in the wake zone. Also for this case, tonal noise is expected as a result of the presence of the blunt trailing edge. Therefore, the last case can proof the power of the hybrid method, since special physical phenomena are present in both the aerodynamic and acoustic part. All the simulations have the same boundary conditions as was addressed in chapter 5. Moreover

	trip height	trip length	total cells	cells on suction	cells on pressure	cell in span	recorded time	recorded samples
clean	-	-	5938800	370	200	50	0.1 s	5000
tripped	0.5mm	46mm	4671576	460	300	40	0.065 s	3250

Table 6.1: Some information about the mesh and simulation runs for the NACA 0012 under seven degrees

the same grid as in the most refined mesh of chapter 5 was used for the clean case. The configuration with the trip has a slight modification. There are more cells in streamwise direction due to the presence of the trip. The cells in the spanwise direction is slightly reduced to limit the increment in cells. Some numbers with respect to the meshes are summarized in table 6.1. A detailed illustration of the mesh design is given in appendix F. Unfortunately, for the present cases no grid convergence study was achieved and an estimate about the error is difficult to make. Therefore the results should be treated with care.

6.2 NACA 0012 with seven degrees angle of attack

6.2.1 aerodynamic quantities

Two simulations were performed under seven degrees angle of attack. One had a clean airfoil surface and another was tripped at its suctions side at a quarter of the chord length. There is a slight difference in the cell numbers due to the presence of the trip. However, the resolution near the trailing edge was aimed to be similar between both simulations, to make a comparison possible. Here, both cases will be investigated and compared with each other. In following discussion, some differences will be addressed.

A comparison with Xfoil panel method will be used to verify some basic flow coefficients. Here, the lift -, drag - , pressure -, and skin friction coefficients will be considered. Additionally, the behaviour of the boundary layer flow will be explored in more detail. A good prediction of the turbulent boundary layer is important, since the majority of the noise is generated in there. Again the boundary layer characteristics are used for the scaling of the acoustics.

The pressure coefficient and the skin friction for the clean and tripped configuration are shown in Figure 6.1 and Figure 6.2. The pressure coefficient is compared with Xfoil data, visualized with the green curve. Both simulations obtain a lower peak value near the trailing edge compared to the Xfoil data. Moreover this underprediction of Cp value is continued over the first part of the suction side of the airfoil, leading to an underprediction of the lift coefficient. The Cp values at the pressure side match properly with the Xfoil data for both simulations. On the other hand, a clear distinction is noticeable on the suction side. The clean configuration shows a transition region starting at 30% of the chord, which is later than the transition prediction of 10% by Xfoil. Afterwards the flow reattaches and becomes turbulent. The skin friction drops rapidly in this region and becomes almost zero as is shown in Figure 6.2. Once the the boundary layer becomes turbulent, the skin friction increases.

The pressure and the skin friction coefficient in this transition region corresponds to one which is generally found in a laminar separation bubble. Initially the flow is reduced to zero velocity at the stagnation point, where it is compressed to the maximum pressure. Due to surface curvature a flow acceleration is generated until a pressure minimum is reached. This is followed by a convex curvature region in which the flow decelerates and pressure increases again. Here a positive pressure gradient pushes the boundary layer and destabilizes the flow, which can lead to separation. Therefore the adverse pressure gradient is found to be one of the main drivers of the laminar separation bubble. A schematic overview of this flow separation mechanism is shown in Figure 6.3. This transition region is not present for the tripped simulation. Typical behaviour of the laminar separation bubble was also reported in Boermans. (2009). However this phenomenon is very complex and still not completely understood. As such, simulating a correct separation point and a correct behaviour of the separation bubble is a hard task and further work on this and validation is required.

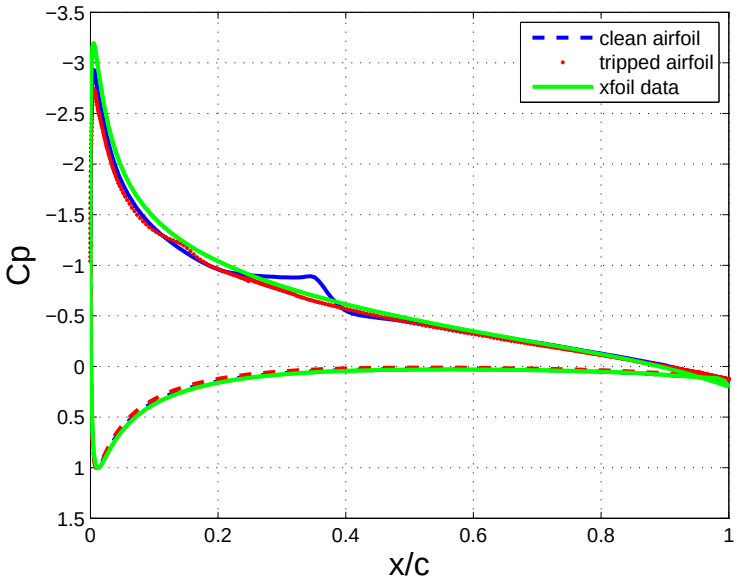

Figure 6.1: Pressure coefficient for the clean and tripped surface

Figure 6.4 and 6.5 show the velocity profiles for both simulation runs on the suction side and the velocity profile near the trailing edge. Note that the velocity profiles are normalized with the outer velocity. Figure 6.4 confirms the transition region located at 30% of the chord. So, it is clear that as the adverse pressure gradient increases, the velocity profiles becomes distorted. As a result the gradient of the velocity near the wall $\partial u/\partial y$ approaches almost zero. The boundary layers for the tripped airfoil retains its full boundary layer profile. The velocity profiles of the pressure side at the trailing edge side were similar to each other (not shown here), indicating the same behaviour of the boundary layer. Figure 6.5 provides the velocity profile at the trailing edge. Due to the tripping, the boundary layer will contain more turbulent structures which cause the boundary to be more full. On the pressure side, the shape is almost similar to each other, since no influence of the trip was found here.

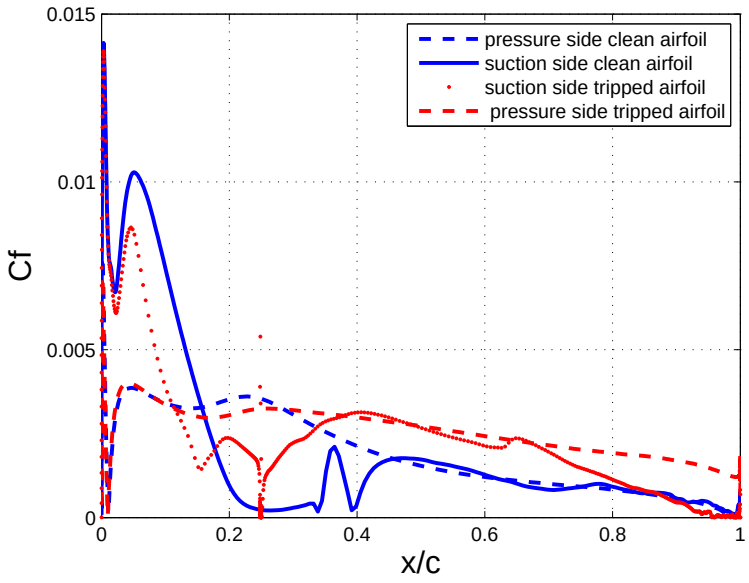

Figure 6.2: Skin friction for the clean and tripped surface

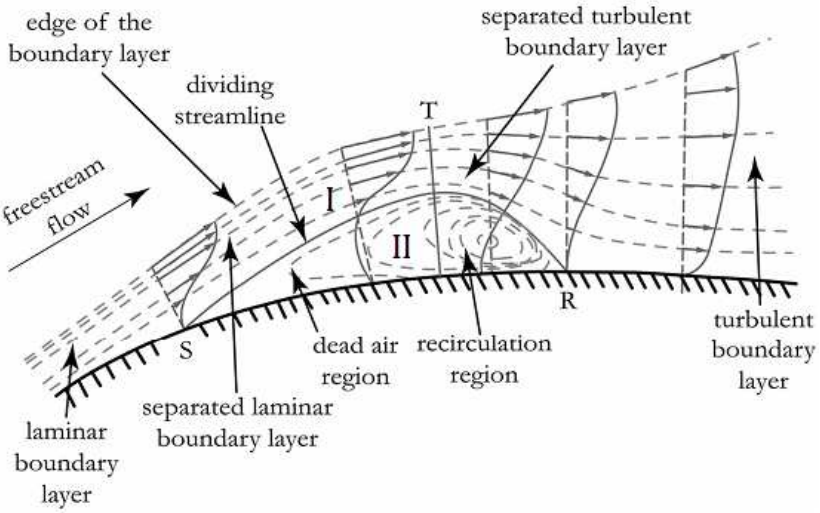

Figure 6.3: Schematic overview of a laminar separation bubble due to adverse pressure gradient

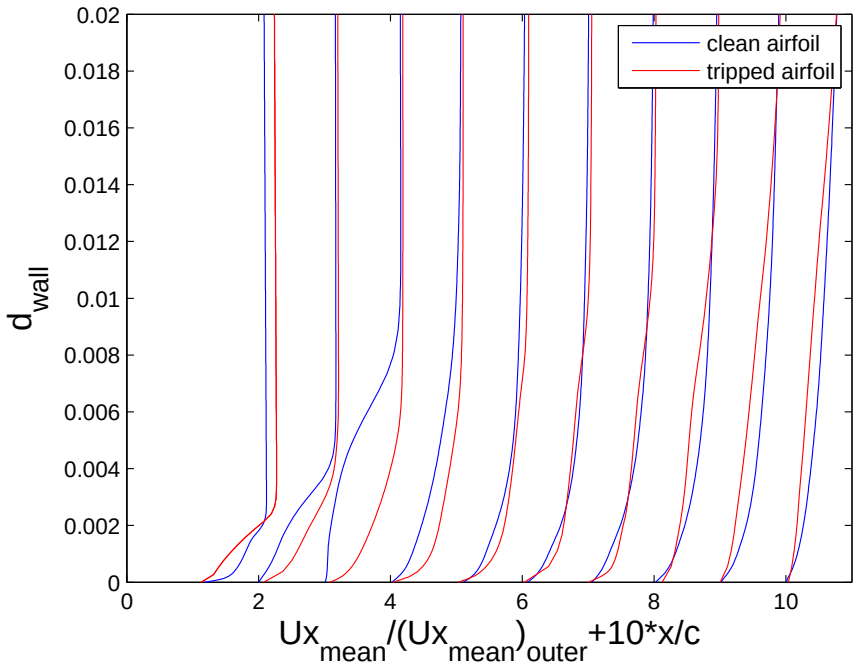

Figure 6.4: Velocity profiles on suction side for the clean (blue) and tripped (red) case. Velocity is normalized with the outer velocity for each position.

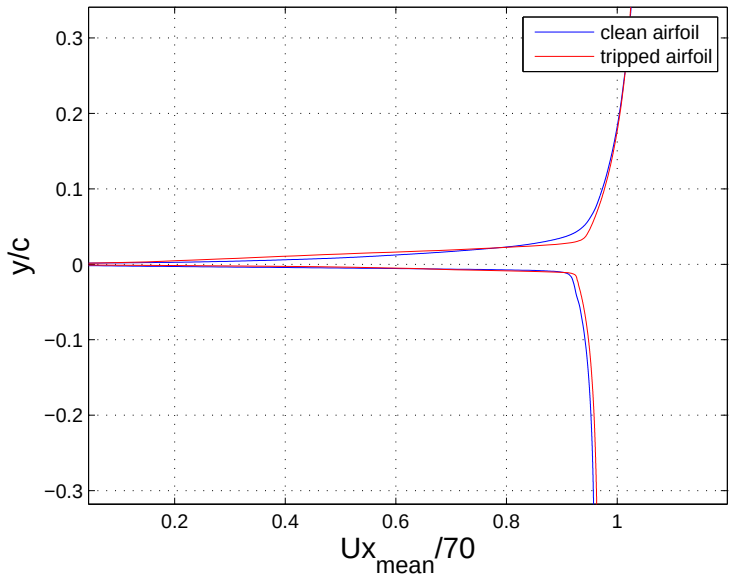

Figure 6.5: Velocity profiles at the trailing edge

Some important boundary layer parameters with respect to the suction side at the trailing edge are summarized in table 6.2.

		$\delta^*[m]$	$\Theta[m]$	H
clean	suction	0.0013	0.0102	1.27
tripped	suction	0.0017	0.0121	1.41

Table 6.2: Overview for boundary parameters for the seven degrees clean and tripped configuration.

To determine the blending position between the RANS and LES-mode the blending function f_{hyb} for the clean and tripped cases are shown in Figure 6.6 and 6.7 for an instantenous time. Remind that in the calculation of the length scale the turbulent viscosity was taken in to account. So it is in essence a time dependent parameter. As was described in section 2.5 the value of f_{hyb} is one in the full RANS mode and is zero for the full LES-mode. The IDDES is a global approach, which means that the whole boundary layer should be treated by the RANS mode($f_{hyb} = 1$). For both cases this was clearly the case, indicated by the red color. It can immediately be observed that the area of the RANS mode is much larger on the pressure side than on the suction side. The reason for this is that the turbulent content is rather low compared to the suction side. Hence, there will be no need to turn into the LES mode. On the suction sides, the area of full RANS mode is much smaller, indicating more turbulent activity. However there is some difference between the tripped and the clean configuration. In the clean configuration, the full RANS modes is much smoother on the suction side, and the thickness is almost equal along the entire suction side. The transition zone between the RANS and LES is represented by a value of $f_{hyb} = 0.5$ and is generally small, indicating a rapid transition. However near the quarter chord on the suction side of the clean airfoil, this transition zone becomes slightly bigger. Note that at this location, a laminar separation bubble was reported before, which probably make the transition zone from RANS to LES less fast. For the tripped airfoil, the blending function in Figure 6.7 is not smooth anymore. Before the trip, a larger full RANS mode and transition zone can be noticed. At the trip location, a transition zone starts away from the boundary and disappears around $0.7c$. Nevertheless a full RANS mode remains near the wall. For a clear understanding of the influence of a trip on the turbulence model further investigation is recommended.

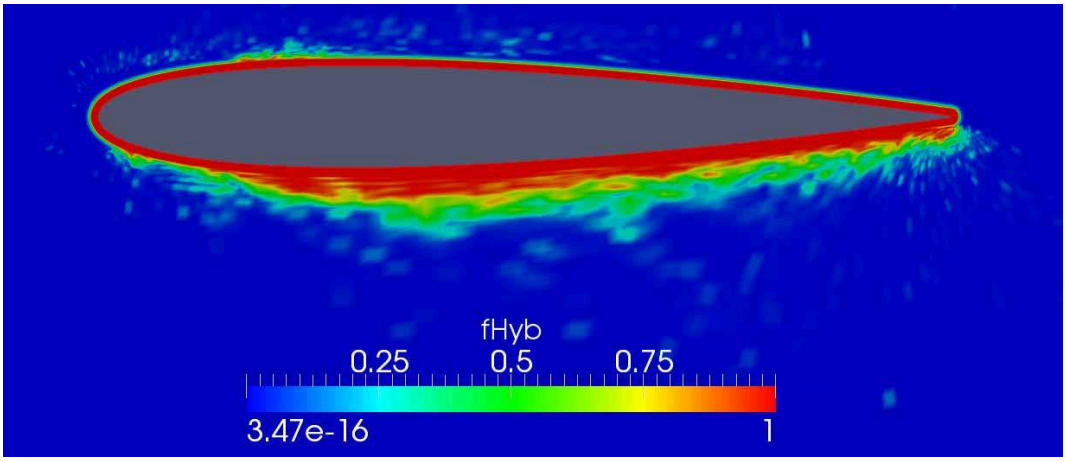

Figure 6.6: Hybrid length scale f_{hyb} for clean configuration. Red color denotes a full RANS mode ($f_{hyb} = 1$). Blue represents full LES mode ($f_{hyb} = 0$).

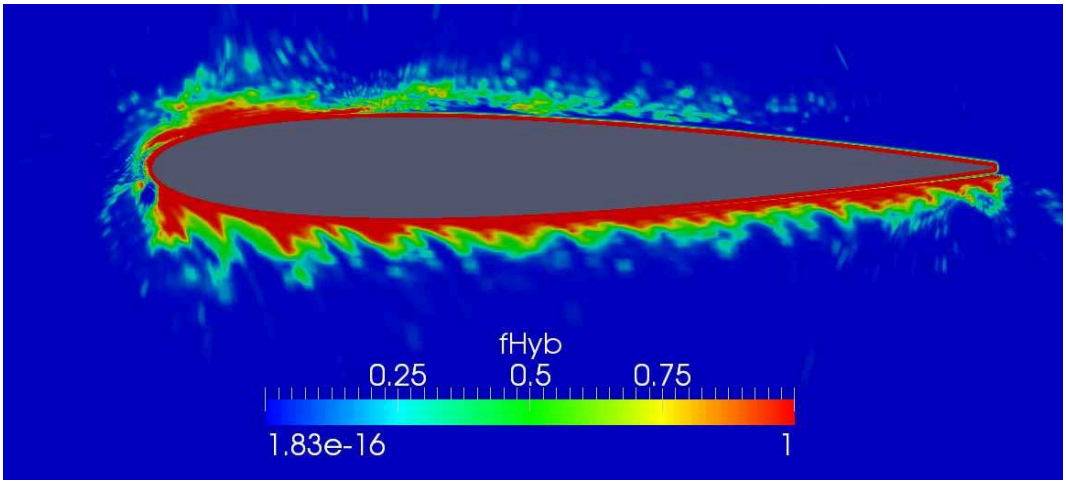

Figure 6.7: f_{hyb} for tripped configuration. Red color denotes a full RANS mode ($f_{hyb} = 1$). Blue represents full LES mode ($f_{hyb} = 0$).

Figure 6.8 depicts some selected boundary layer profiles in a logarithmic scale for the suction sides of the clean and tripped airfoil. The non-dimensional profiles show also the location of the blending behaviour for the turbulent boundary layer. A star symbol is added to flag the position $f_{hyb} = 0.5$. It seems that almost for all the boundary layer, the blending occurs outside the boundary layer. The profile near the trailing of the tripped airfoil has a blending in the boundary layer at $y^+ = 45$.

Figure 6.9 shows the time history of the tripped and the clean case. The tripped case becomes a little bit faster turbulent with respect to the clean case. For the clean case it takes longer to develop since no transition was triggered. The mean value for the tripped case is observed to be lower as the clean case, which was expected due to the faster transition and the effect on the pressure distribution observed in Figure 6.1. Moreover the form of the signal is different for both cases. Since for the acoustics the pressure fluctuations along the surface are considered, and consequently are related with the lift coefficient, one can already expect a priori a variation in the sound pressure level spectra. This will be discussed shortly.

Figure 6.10 and 6.11 show the mean magnitude velocities of both the clean and tripped configuration. For the clean case a region with low velocity is visible at the suction side at a quarter chord length. Here, the transition zone is clearly present, even suggesting a laminar separation zone, as already was found in the velocity profiles shown in Figure 6.4. This transition zone is disappeared for the tripped case. A close-up of this transition region is given in Figure 6.12 and 6.13. The behaviour at the pressure side is similar between profiles of the clean and tripped case. This was confirmed with the wake profile considered in 6.5.

A representation of the turbulent structures and vortex detectation, given by the Q-criterion is shown in Figure 6.14 and 6.15. Both simulation can generate fine turbulent structures and clearly show the transition region. The transition region for the clean configuration is characterized by larger structures compared to the tripped configuration. The tripping causes the flow to become rapidly turbulent.

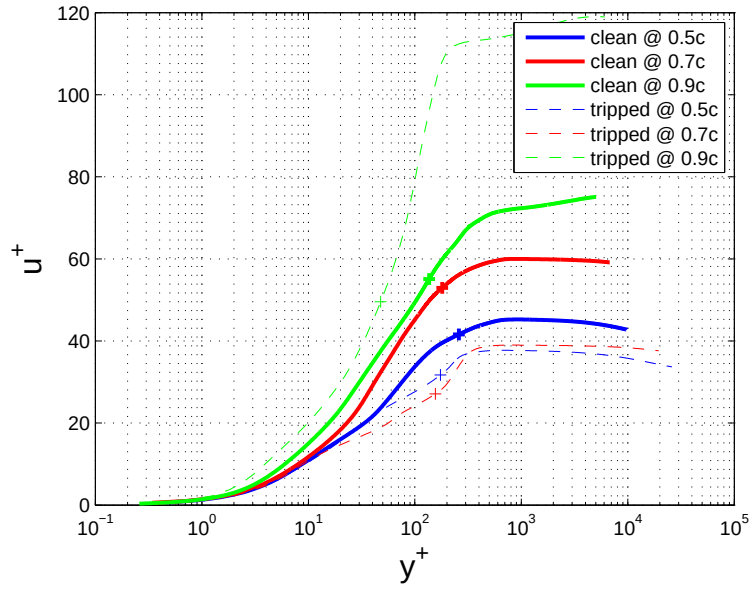

Figure 6.8: Non dimensionlised velocity profile with indication of hybrid length scale=0.5 (full line: clean, dashed: tripped) for different positions.

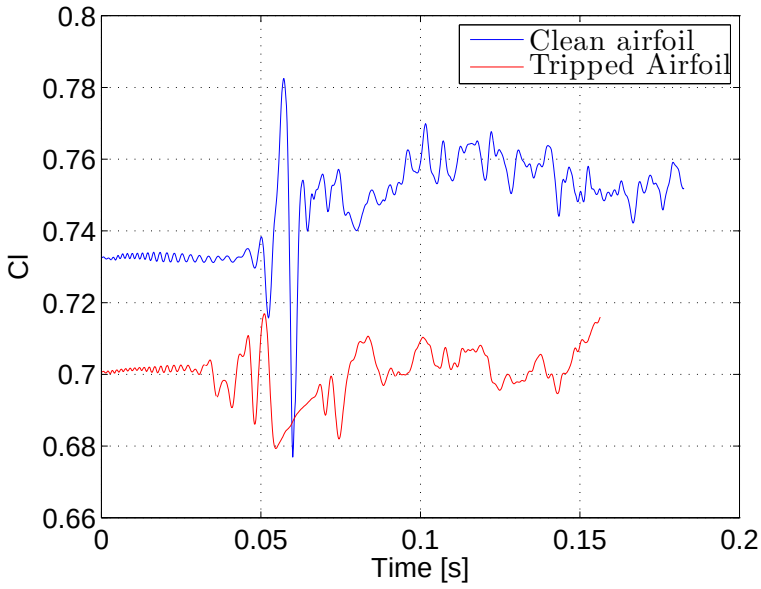

Figure 6.9: Cl coefficient for clean and tripped airfoil

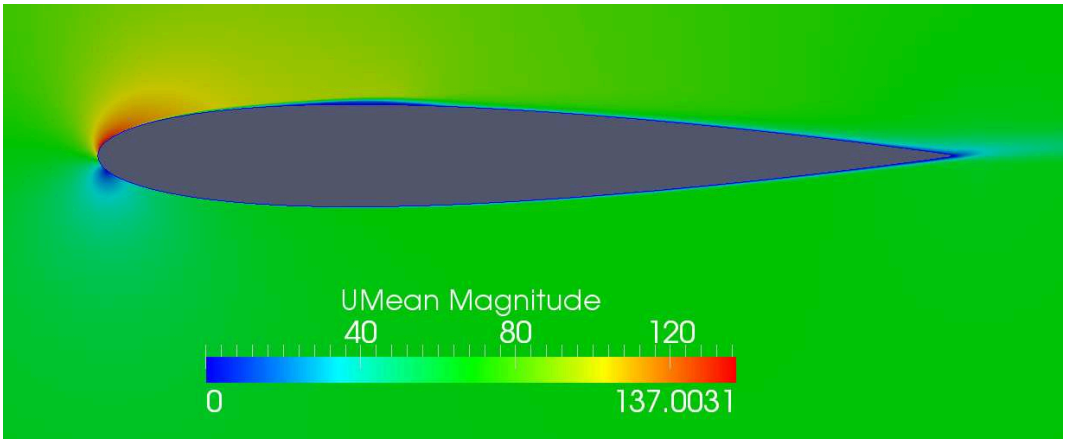

Figure 6.10: Mean Velocity flow field of clean case with laminar separation bubble around 30% of the airfoil

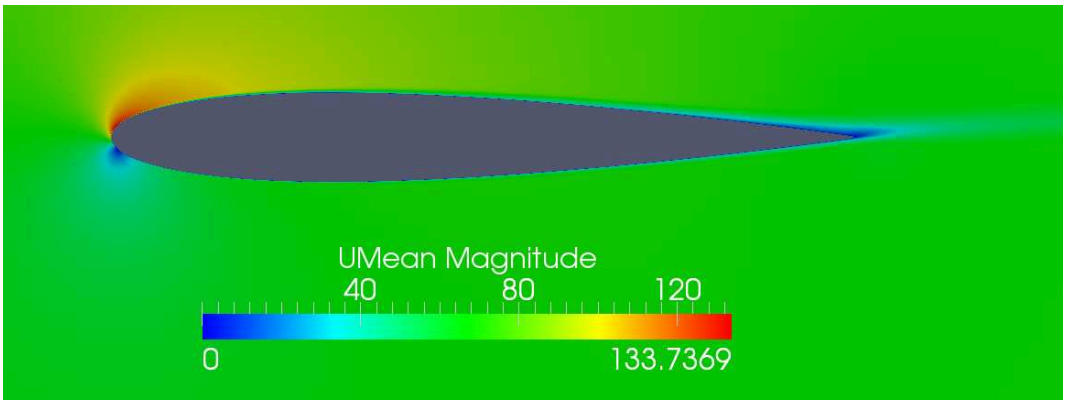

Figure 6.11: Mean Velocity flow field of tripped case. No separation bubble is noticed.

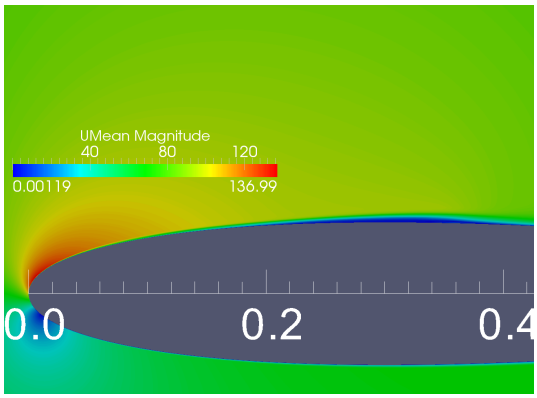

Figure 6.12: Close up of the mean velocity flow field of the clean case with laminar separation bubble around 30% of the airfoil

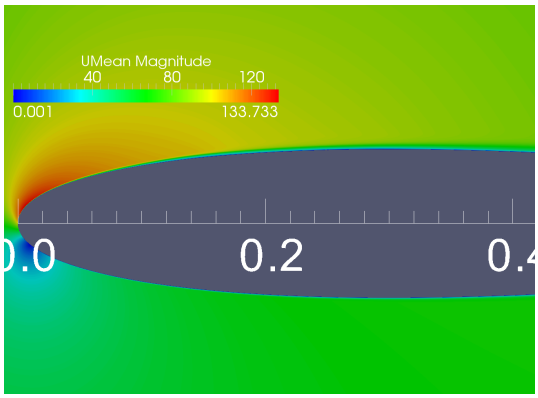

Figure 6.13: Close-up of mean velocity flow field of tripped case. No separation bubble is noticed.

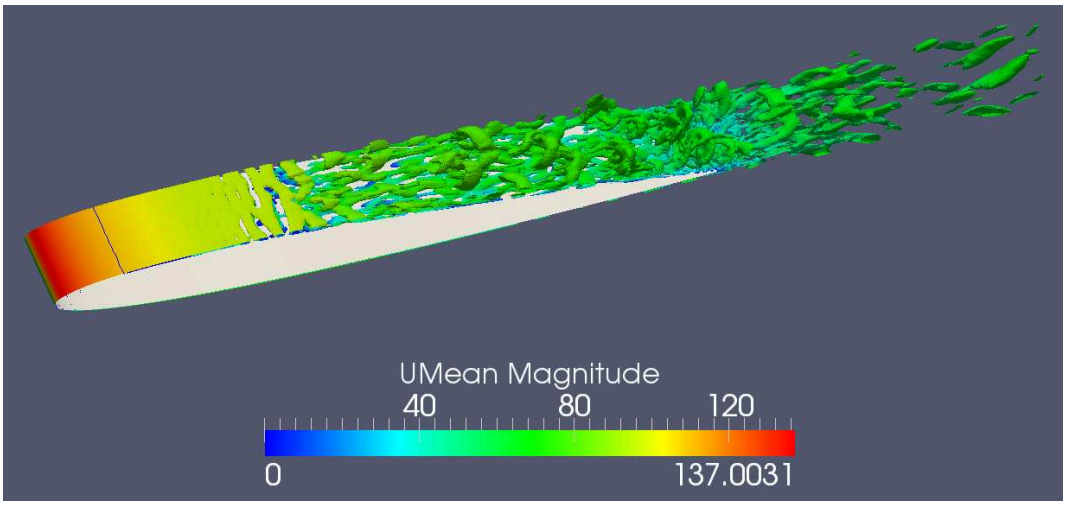

Figure 6.14: Q-isosurface 1E5 colored with mean velocity(clean), with larger transition region

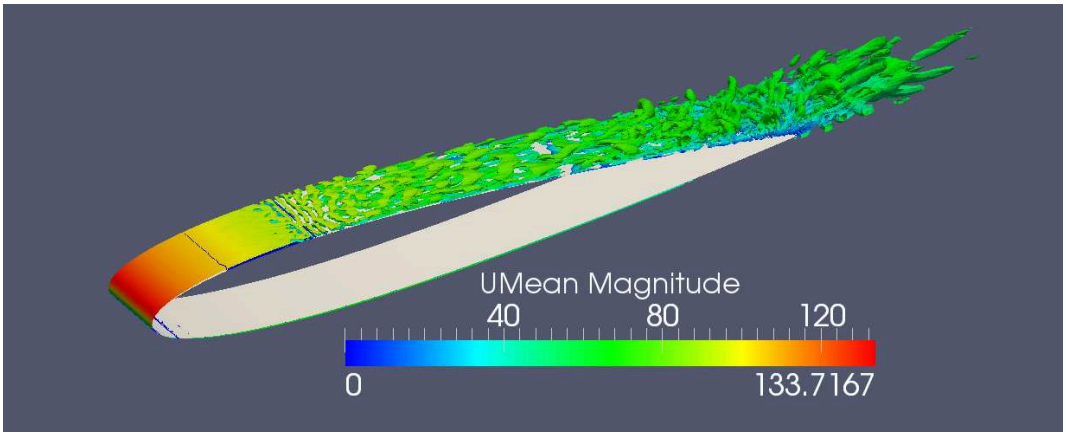

Figure 6.15: Q-isosurface 1E5 colored with mean velocity(tripped). The turbulator strip causes rapid change in turbulent fluctuations.

6.2.2 acoustics

The acoustics of the NACA 0012 were analyzed in chapter 5 and were in relative good agreement with the reference data. The same process was repeated here to determine the acoustics of the seven degrees cases. Therefore the pressure was recorded during the simulations. For the clean configuration the recorded pressure covers $0.1s$ in physical time. In total the time history of the signal presented in Figure 6.16 contains 5000 samples, so that each $2E-05s$ the pressure on the surface was saved. The time history of the tripped case, shown in Figure 6.17 spans a physical time of only $0.07s$. This corresponds to only 5 cross-overs, which is rather small for an acoustic analysis. Note that for both time signals, the start-up phenomena are ignored.

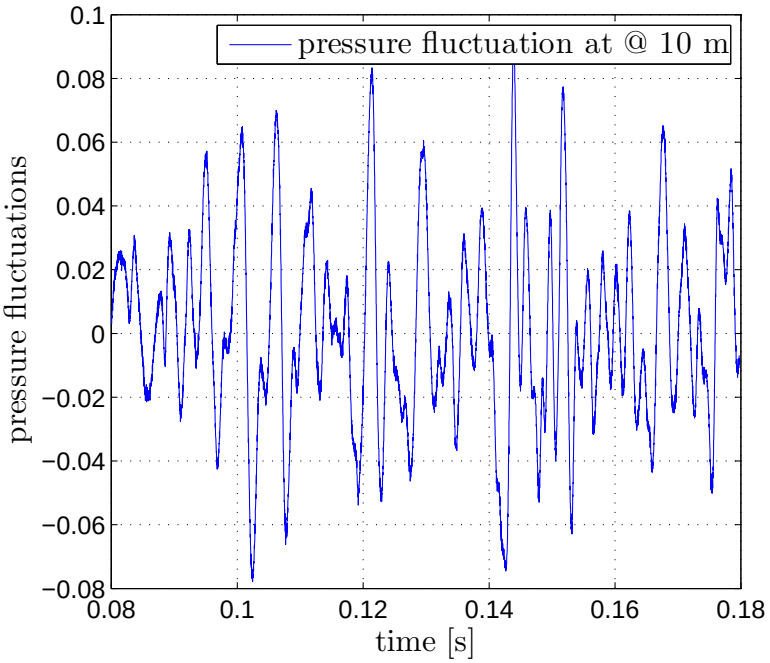

Figure 6.16: Pressure fluctuations in time at observer 10 meters. Seven degrees angle of attack for clean airfoil

There is a clear difference between both time signals. The pressure fluctuations of the clean airfoil are more smooth and show some regularities compared to the tripped case. The time series of the pressure signal in Figure 6.17 shows clearly more irregularities. It looks to be divided in two parts. In the first part of the signal (till $0.125s$), the frequency of the oscillations is much lower than the second part of the time series. Moreover, the first part of the time series contains larger amplitudes compared to the second part. It might be that the first part of the signal contain still start-up phenomena, which is undesirable for acoustic computations. However, it should be noticed that the second part of the time series in the tripped case looks more to the signal generated by the clean configuration. The maximum amplitude of the pressure fluctuations are comparable, but the frequency is much higher.

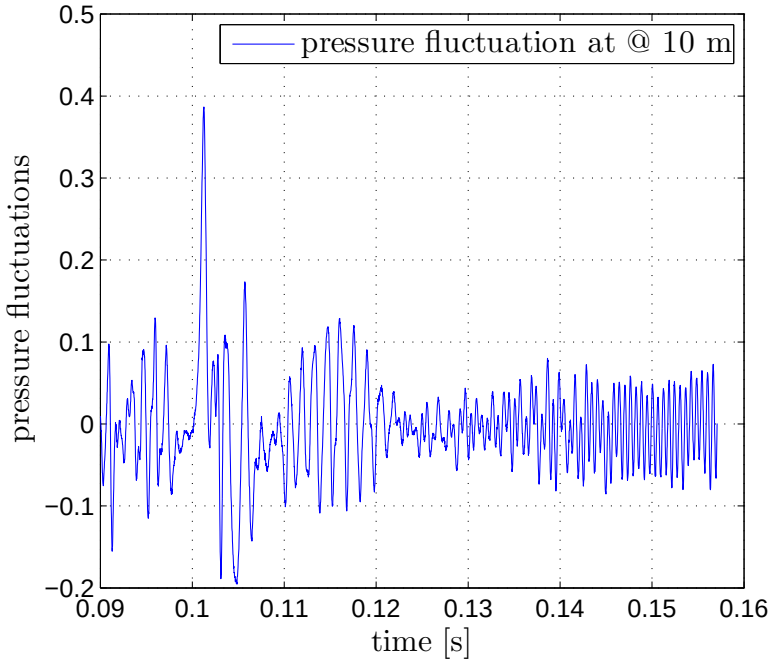

Figure 6.17: Pressure fluctuations in time. Seven degrees angle of attack for tripped airfoil

Based on these pressure signals, the SPL is calculated. Remind that for aeroacoustic analysis one needs sufficient data samples. Hence it is clear that the tripped case is unreliable for decent analysis. Certainly more data should have been recorded, but unfortunately the time was limited. It can be expected a priori that they will result in a different SPL.

Figure 6.18 shows the calculated rescaled sound pressure level in comparison with the reference results Brooks et al. (1989). Again the scaling was based on the formulation provided in equations 5.6 and 5.7. The boundary layer thickness was reported in table 6.2 and equals 0.013 m for the clean configuration and 0.017 m for the tripped configuration. The freestream velocity is $70m/s$ ($M = 0.204$). The observer was located at ten meters above the trailing edge.

The SPL denoted by the thick green graph (clean) matches reasonably well with the experiments. The general trend in the SPL was also found in the reference. Still an underprediction of the peak value of around 3 to $5dB$ can be noticed. Also a small shift in the normalized frequency is found, but is acceptable. For the normalized frequency ranging from 0.05 to 0.07Hz the underpredicton becomes almost $10dB$. Lower frequencies are not considered to be in the range of acceptable accuracy. The SPL denoted by the cyan curve corresponds to the tripped configuration and clearly deviates from the reference. A mismatch in both the peak value and frequency can be observed. Referring to the pressure fluctuations in Figure 6.17 the low frequencies showed higher amplitudes (in first part of the signal), whereas the high frequencies are mostly present in the last part of the signal. The analysis of the time series of the pressure fluctuations provides not enough consistency to be confident in the actual results. Putting it differently, one will find different sound pressure level spectra when the

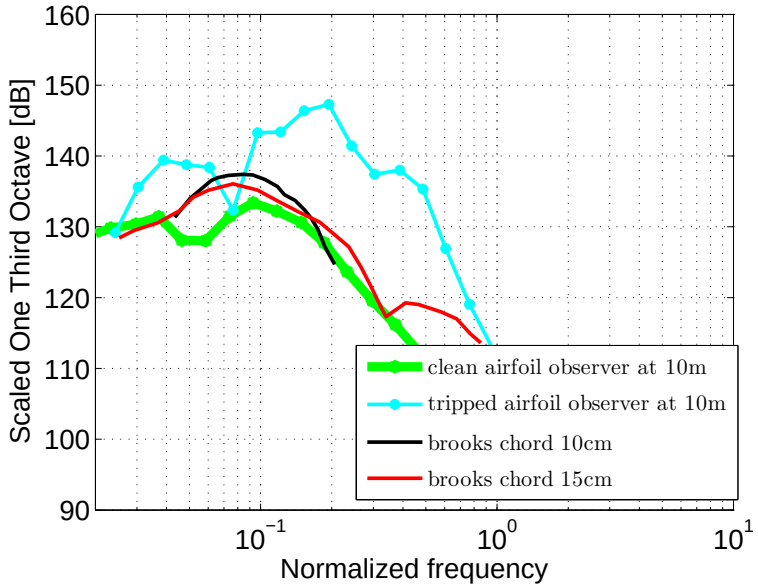

Figure 6.18: SPL for clean and tripped configurations and reference of brooks (whole time intervals)

time signal is chopped in different parts. The first part of the signal will result in a more broadband noise, whereas the second part will be determined with tonal noise. This is also observed in Figure 6.19 where the SPL's for 3 different time intervals were presented. The peak at a frequency of around 1800Hz is allocated to the last part of the time signal. No such a strong tonal noise was observed in the first part.

Next we will try to identify the location of the high frequency noises. Therefore, we will consider three different sections of the NACA 0012 and compare their contribution to the overall sound spectra. Figure 6.20 shows an overview of the different sections on the airfoil. The entire airfoil is also included and is denoted in the blue color. For the other sections, the upper part (with the trip) of the NACA 0012 was not included. Cuts were made at a y-location of 0.04m and 0.02m and are depicted in the green and red color. Previous acoustic analysis were repeated on these sections and their pressure fluctuations for these three cases are presented in Figure 6.21. The upper time serie corresponds to the entire airfoil and the lower two are results from section 1 and section 2. It can be observed that the amplitude of the pressure fluctuations decreases for each cut-off, which is logic since there is less surface area accounted to produce noise and a lower peak value is found in Figure 6.22. Moreover the higher frequencies at the last part of the signal remain and a tonal peak still appears. The pink curve represents the SPL of the pressure fluctuations along the pressure side only. The strong tonal noise is disappeared, although it is still noticeable.

A directivity plot is shown in Figure 6.23 and illustrates the dipolar radiation of the noise mechanism. Note that the lobes, which are generally characteristic for higher frequencies are not visible.

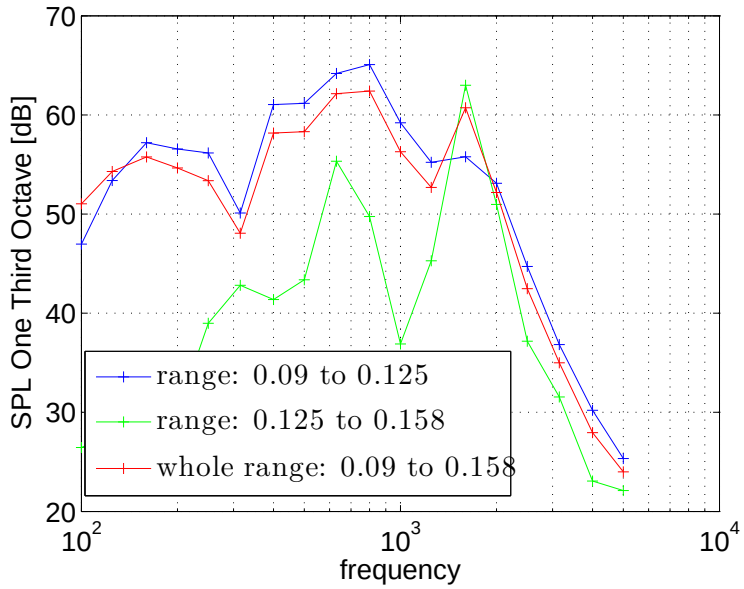

Figure 6.19: SPL for tripped configuration with respect to three different time intervals

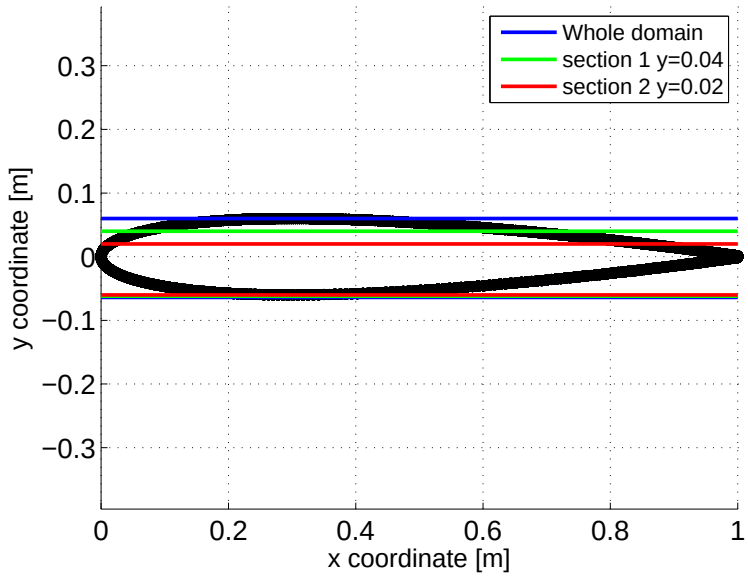

Figure 6.20: Overview of different airfoil sections. The blue section denotes the whole airfoil. Green represents section 1 for which the surface above $y = 0.04$ is removed. Red corresponds to section 2.

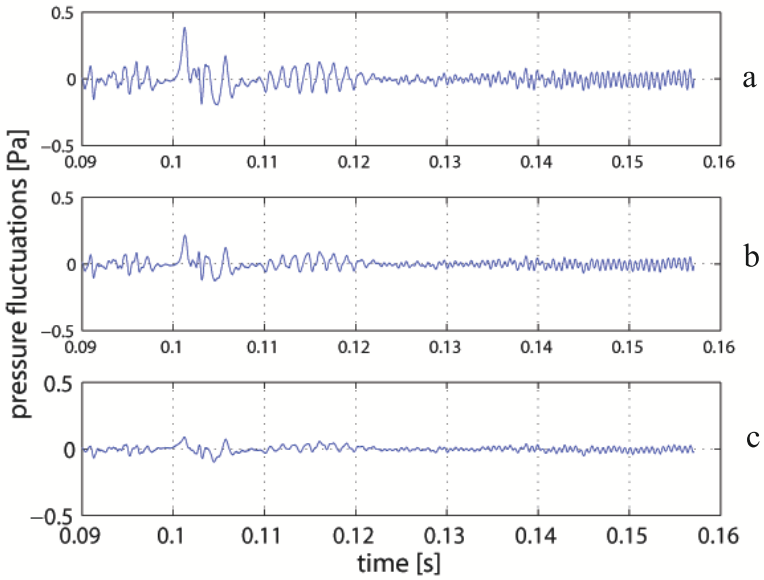

Figure 6.21: Pressure fluctuations for different sections. Graph (a) represents the whole airfoil. Graph (b) and (c) correspond to section 2 and 3

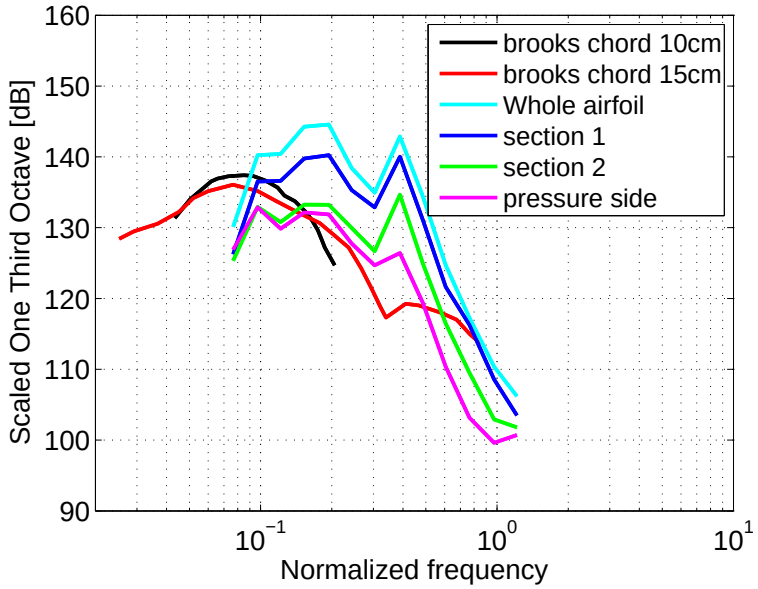

Figure 6.22: SPL for different sections of the tripped airfoil. The reference is included for convenience.

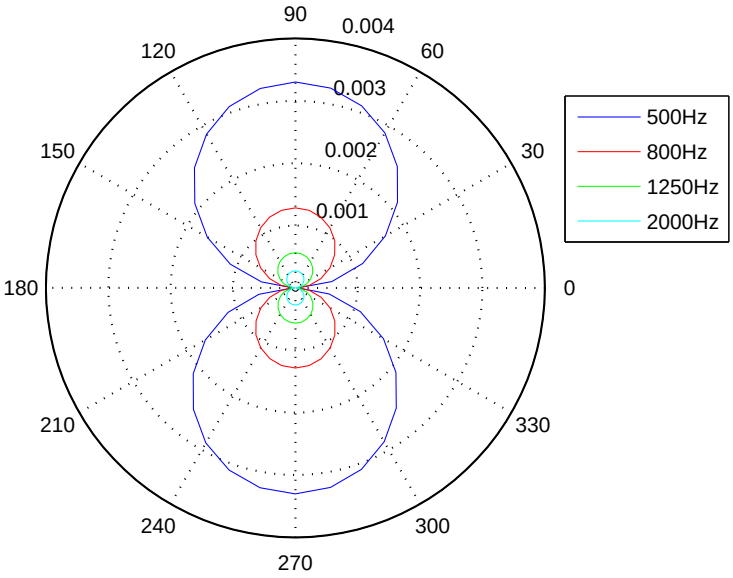

Figure 6.23: Directivity plot for clean configuration for different frequencies.

All these findings indicate a possible bad behaviour in the current simulation of the tripped case. Allocating or judging these causes is a challenging task and requires more experience. On the one hand, a longer time series of pressure fluctuations can already be a first step. The recorded samples cover only 5 cross-over times and are rather too limited for good statistical aeroacoustic analysis. But on the other hand the duality in the time signal gives rise to questions concerning the simulations. Although the averaged pressure distribution was acceptable, the time behaviour still remains unclear. Several questions are unanswered and are summarized below:

- Is the tripping properly done? In experiments one applies typically a zig-zag strip. Similar tools are not available in the CFD software and will make the meshing hard to perform. Instead a continuous trip over the whole spanwise length was used as is shown in Appendix F.
- The mesh refinement around the tripping was limited. Due to the abrupt transition to turbulence the mesh should be fine enough to sustain the LES content. More research on this should be done.
- The response of the IDDES model to a tripped surface was not discussed. A larger transition zone with respect to the blending function f_{hyb} was observed. The consequences of the results are not investigated and requires further investigation.
- Do the Curle formulation posses some difficulties in the evaluation of the tripped case and is it still a valid approach?

Although it was an initial set-up and experience was missing, the IDDES has shown some encouraging results. However the tripped case could not be seen as completely successful. Therefore results should be treated with care and criticism. More investigation and effort on verification and validation is absolutely required.

6.3 Naca 0012 with blunt trailing edge

Finally, it is important to consider that modern large wind turbine blades are composed by a region in which the airfoils shapes have large blunt trailing edges. This region is located in the transition between the circular sections of the root and the typical aerodynamic sections of the rest of the blade. Concerning the side mirrors of cars, a similar type of geometry is found in the automotive industry. This noise mechanisms are based on the noise emission by von Karman type vortex shedding from the trailing edge. The shedding of vortices from the trailing edge depends on the bluntness, shape of the edge, and Reynolds number. The alternating vortices produce pressure fluctuations in the trailing edge zone as depicted in Figure 6.24 According to Wagner et al. (2007), tonal noise will appear in the noise spectra if the trailing edge thickness of the airfoil is higher than certain cut off value. This cut off value is specific for each airfoil and flow condition. The frequency of the spike originated depends on the flow conditions and the trailing edge thickness to displacement thickness ratio,

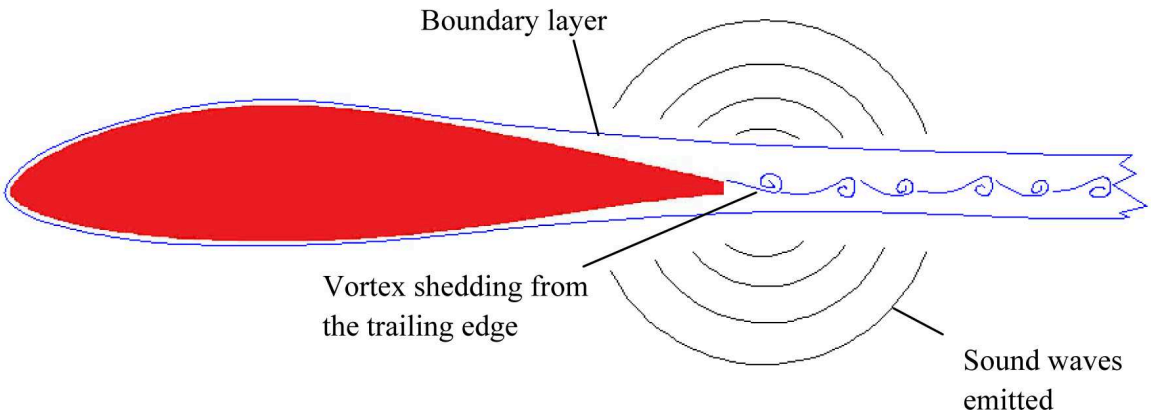

Figure 6.24: Representation of blunt trailing edge noise

h_{te}/δ^*. The smaller the trailing edge thickness to displacement thickness ratio the higher is the shedding frequency. Therefore, if the trailing edge is sharp enough, only broadband noise will be present. This was illustrated for the NACA 0012 under zero degrees (see chapter 5).

The frequency at which the vortices are shed depends on the object shape and flow conditions. The dimensionless Strouhal number shows however to be a constant depending on the object shape only. The Strouhal number for a blunt body is given by:

$$St = \frac{f h_{te}}{U_\infty} \tag{6.1}$$

Where, f is vortex shedding frequency, h_{te} is the trailing edge height and U_∞ the freestream velocity. Normal trailing edges are found by Blake (1986) to have a Strouhal number around 0.164. Blake concluded that vortices will certainly shed when $h_{te}/\delta^* > 0.5$. A Strouhal number of 0.2 0.21 corresponding to a flat plate was found by Parker and Welsh (1983).

Brooks also conducted experiments with a simplified blunt trailing edge. The trailing edge geometries are shown in Figure 6.25. As a result he found that the peak Strouhal number depends on the ratio of the trailing edge height and the boundary layer thickness. This dependency for the NACA 0012 is illustrated in Figure 6.26. For large values of boundary layer thickness ratio one achieves a Strouhal number of 0.145.

For this blunt test case, no further scaling of the SPL to the reference data was elaborated. It was only intended to demonstrate the feasibility of the current turbulence model and the acoustic analogy to cope with the large separation region in the wake. In principle this turbulence model should perform well, since the hybrid RANS-LES methods can cope with separated flows. Nevertheless it was interesting to investigate such problem to show its potential of application to various flows.

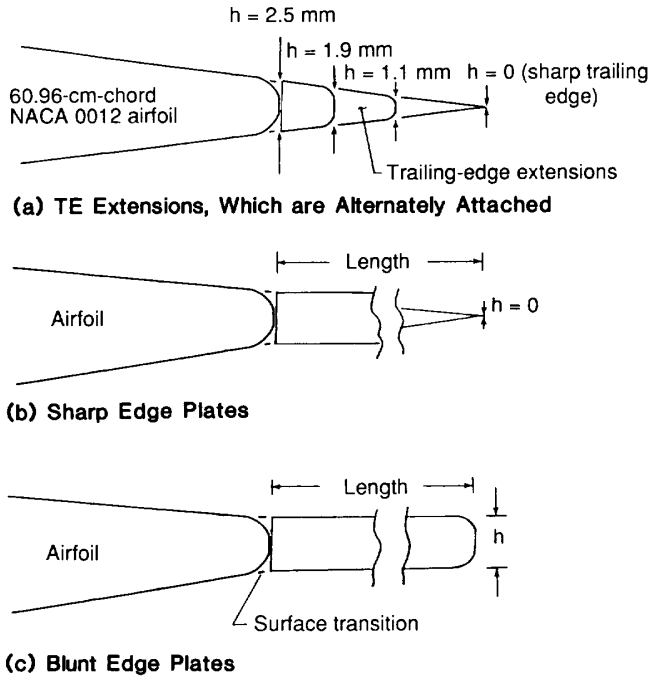

Figure 6.25: Blunt trailing edge geometries used in Brooks et al. (1989) experiment

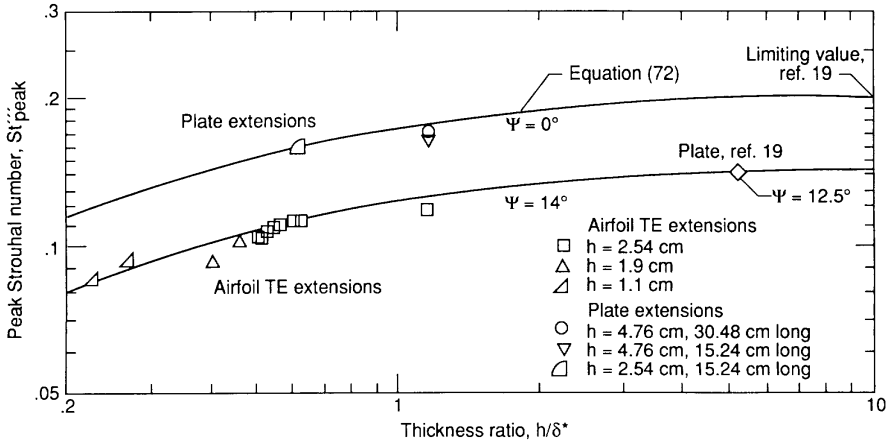

Figure 6.26: Peak Strouhal number dependency versus the thickness ratio h/δ^* (Brooks et al. (1989))

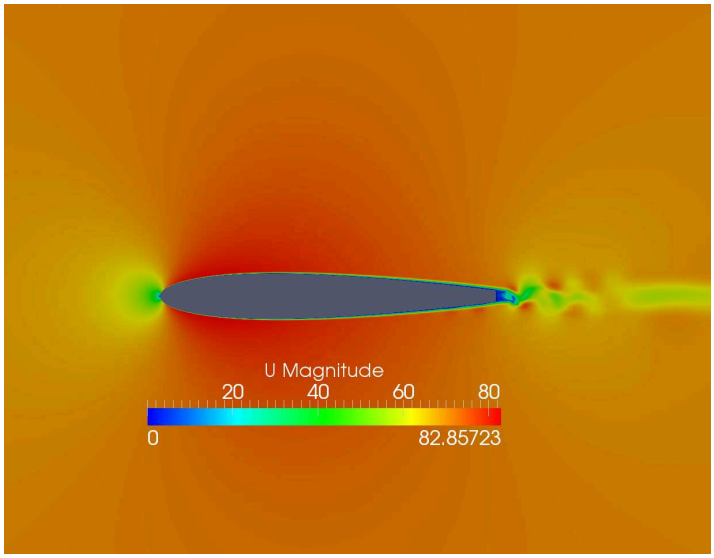

Figure 6.27: Instanteneous velocity of blunt trailing edge showing vortex shedding.

6.3.1 aerodynamics

The blunt TE was generated by removing the last part of the original NACA 0012 profile. The airfoil retains a chord length of 0.9m and has a trailing edge height of 0.03m. As such it was assumed that vortex shedding will certainly occur. The trailing edge is rounded to promote the mesh quality. The mesh near the trailing edge is shown in Appendix F.

The vortex shedding is clearly visible in Figure 6.27, which is a snapshot of the velocity field and is a preliminary indication of a good thickness to height ratio. Figure 6.28 show the pressure fluctuations p'^2 on the airfoil surface near the trailing edge. The red area indicate the region where large fluctuations occur. A blue color corresponds to limited fluctuations. It is observed that near the trailing edge the largest fluctuations are situated. Note that Figure 6.28 corresponds to one single snapshot, and that the location of the peak value will change due to the vortex shedding. Figure 6.29 shows a representation of the turbulent structures in the format of the Q-isosurface. A roll-up along a large part of the suction and pressure side can be observed. Near the trailing edge, the turbulent structures start to break-down as vortex shedding occurs. The iso-surfaces are colored with the mean velocity magnitude and show a separation bubble located at the trailing edge.

6.3.2 acoustics

The acoustics are also calculated for the blunt trailing edge according to equation 4.6. The time serie for the pressure fluctuations at an observer 10 meters above the trailing edge is shown in Figure 6.30. The time series demonstrate some regularities due to the vortex shedding and is rather smooth compared to the time series for the zero and seven degrees. The time series are also used to calculate the noise spectrum, shown in Figure 6.31. The

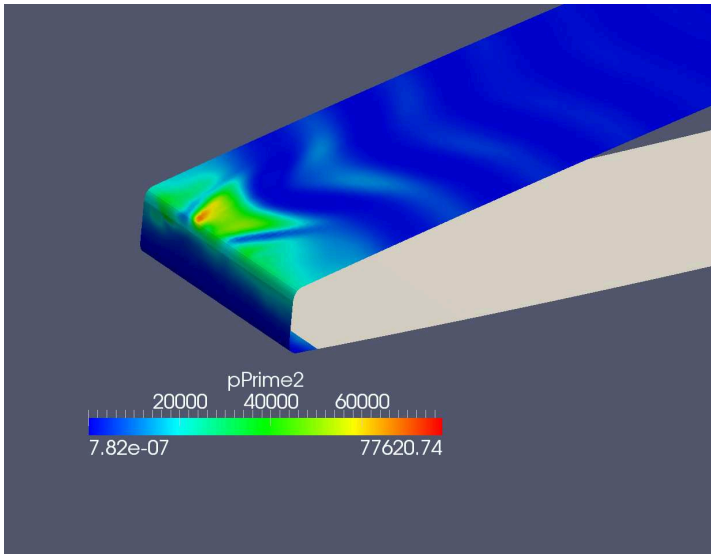

Figure 6.28: Pressure perturbations along the airfoil surface. Red areas near the trailing edge indicate large fluctuations and consequently large contribution to the noise sources.

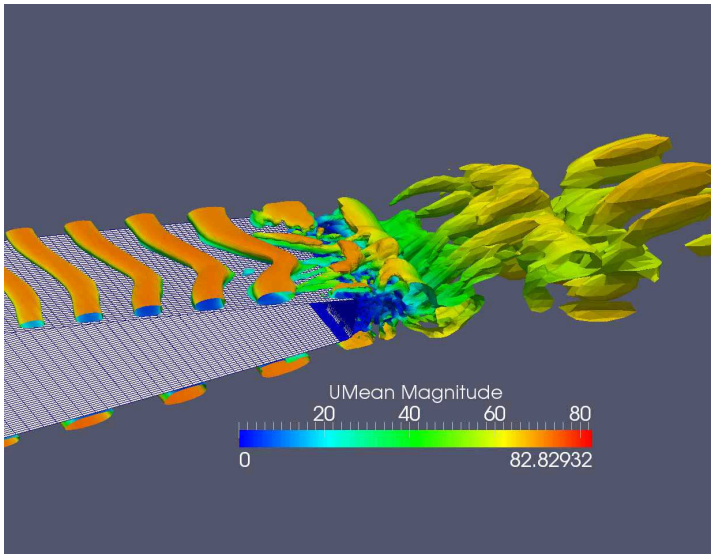

Figure 6.29: Q-isosurface=1E5 colored with velocity magnitude. Turbulent structures breakdown at the trailing edge

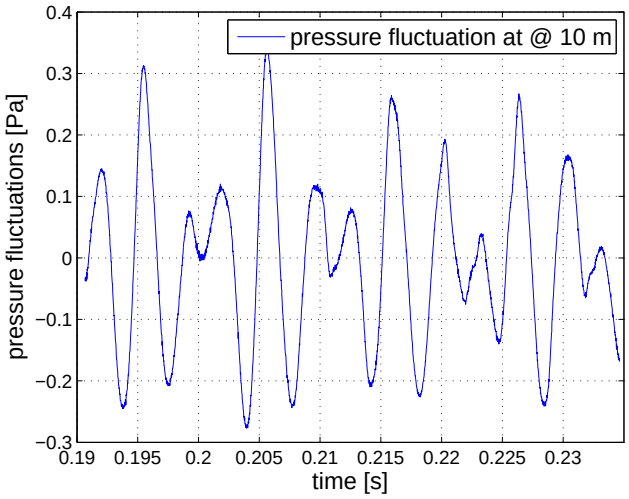

Figure 6.30: The time series for the pressure fluctuations for the blunt trailing edge.

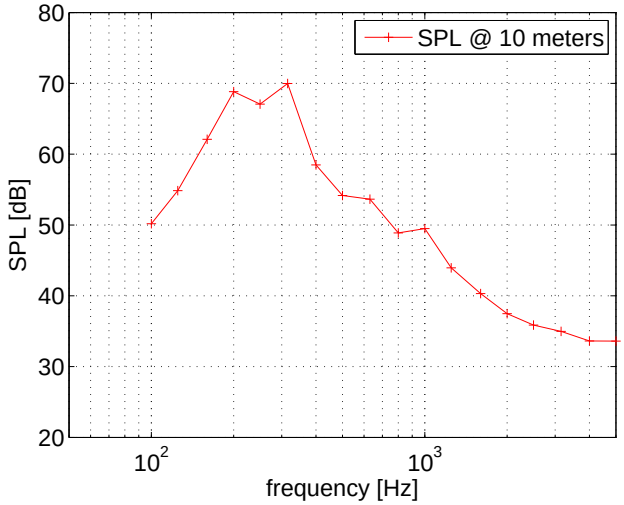

Figure 6.31: Third octave spectra for a blunt trailing edge

noise spectrum associated with the blunt trailing edge is more concentrated around a few frequencies, resulting in tonal noise. For this simulation the frequency at which the maximum SPL can be found is equal to 315Hz. When the scaling of equation 6.1 is applied with $h_{te} = 0.03$ m and a freestream velocity of 70 m/s, one will obtain a Strouhal number of 0.135. This is an acceptable value since 0.14 was found by Brooks et al. (1989) and presented in Figure 6.26. This demonstrates the potential of current method to deal with larger separation zones and its corresponding acoustics. No further scaling of the magnitude of SPL was performed, since no clear data was available. Further work can focus on validation or the design of a blunt trailing edge to reduce the generated noise.

Chapter 7

Conclusions and Recommendations

The main goal of this thesis was to determine the trailing edge noise emanating from an airfoil. The answer to this question and the conclusion found in this thesis is found to be positive in the sense that the potential of the hybrid methods was demonstrated. Nevertheless some issues concerning the simulations still remain. To reach this conclusion a variety of numerical experiments and validations were conducted. In this chapter, the conclusions and recommendations based on the test cases and the problems encountered will be addressed.

7.1 Conclusions

Several possibilities are available to reach the aim of this thesis. Aeroacoustics could generally be calculated in two ways: either with a direct method or with a hybrid approach. The direct method was not considered in this thesis for mainly two reasons. First, the excessive computational cost and second the inherent multi-scale problem in aeroacoustics for low Mach flows. In the hybrid methods the aeroacoustic problem is split in two branches in which the noise sources are computed separately from the far-field propagation.

A hybrid RANS-LES was selected to compute the aerodynamic quantities which are used to identify the noise sources. The propagation in the far-field was provided with the acoustic analogy formulated by Curle.

Several test cases are conducted in this thesis. The main findings with respect to these simulations are:

1. The boundary layer profiles of the flow over a flat plate showed acceptable agreement with reference data. The steady-state RANS simulations with the Spalart-Allmaras turbulence model are comparable to DNS simulations and RANS simulations performed with fluent. This comparison indicates the appropriate behavior near the wall. The

boundary layers of the unsteady IDDES approach showed slight differences with respect to the reference data and as such require further investigation.

2. Both the original S-A DES model and the IDDES were tested on the same computational grids. No turbulent structures were found for the S-A DES model. The S-A DES model encounters difficulties in boundary layer dominated flows, because it excessively damps the resolved turbulence near the wall. For the IDDES approach the transition to the LES mode is more abrupt and boosts the turbulence.

3. Different mesh resolutions were considered for the NACA 0012 with zero angle of attack. Convergence based on the lift coefficient was achieved when considering finer meshes. The aerodynamic quantities and boundary layer profiles revealed unsymmetric behavior between the pressure and suction side, probably due to the different mesh strategies between both sides. The response of the turbulence model(IDDES) to this difference in meshing is unclear and certainly requires further investigation.

4. Moreover the different mesh resolutions indicate that the noise generation amplitude and frequency are connected to resolutions.

5. A grid study based on the SPL showed a good convergence. Validation was established by comparing the sound pressure level to the reference data of Brooks et al. (1989). The coarse meshes overpredict the SPL with around $10dB$. The comparison of the fine grid showed acceptable agreement with the reference.

6. Two configurations were done with seven degrees angle of attack. One in clean configuration, the other with a trip. The clean configuration showed a strong laminar separation bubble at a quarter chord, which disappeared for the tripped case. The boundary layer was more turbulent on the suction side due to presence of the trip. The boundary layer profiles along the pressure side were similar for both cases.

7. Reasonable agreement with reference data for SPL was found for the clean configuration. The tripped profile showed a rather different sound pressure level, both in magnitude and frequency. Analysis of the time series of pressure fluctuations demonstrate a lack of consistency, and as such results should be treated with care.

8. By excluding parts of the profile it was tried to identify the high frequencies. It was suggested that the high frequencies, generating tonal noise were located near the trailing edge.

9. The feasibility of dealing with large separation zones was investigated by the consideration of the NACA 0012. Large pressure fluctuations were found near the trailing edge, resulting in tonal noise corresponding to the Strouhal number found in Brooks et al. (1989).

7.2 Recommendations

This section lists some remarks which were encountered during this thesis work and require more effort. A proposal for further work is included to facilitate the start-up of following

master thesis projects.

1. The current hybrid RANS-LES approaches are rather complex approaches. The identification of modeling errors is very challenging. Here, the transition zone between the blending between the RANS-LES simulations can give rise to modeling errors and is not always clear. Questions that should be answered are: is there a good interaction or communication between the RANS and LES mode and what are the effects on the overall flow field?

2. To identify the modeling errors, more focus should go to validation and verification.

3. Comparison with other softwares or other forms of turbulence modeling is not considered and as such can give valuable information.

4. The results of the boundary layer tripping were questionable. Better treatment of the tripping is required. A grid refinement near the trip can be a first approach.

5. Another important factor for IDDES simulations is meshing. On the one hand the mesh should provide sufficient resolution. On the other hand, the mesh quality should be guaranteed. Improvements in local refinement, without increasing the cell number can be made.

6. Despite the cost savings promised by the hybrid RANS-LES simulations, long calculation times are still the main obstacle. Methods to speed-up calculations or experience with solver settings are very welcome. Especially the solution of the pressure equation contributes most to the computational time. Any improvements here can be beneficial and can contribute to a faster turn-over time.

7. Reference data which can provide a combination of aerodynamic and acoustic data is limited, and therefore validation of numerical simulation is restricted. Therefore, more benchmarks are necessary.

8. Curle's compact acoustic analogy is a simple expression which is based on underlying assumptions. Therefore Curle's formulations is restricted in use. More advanced methods such as LEE or APE can be more accurate.

9. As a closing remark I would like to state that it would be very wisely to start CFD simulations with simple geometries, such as a flat plate, backward facing step or cylinders. These already have complex flow phenomena and they will be useful to learn the basic principles. Moreover they are easier to mesh and count less cell numbers, leading to a faster turn-over time and the possibility to set-up more simulations. Another important feature of these cases is the detailed information and the knowledge which can be used to validate or compare initial simulations. Once experience and confidence is gained, the next step can be taken towards more complex flows.

Bibliography

W. Bechara, C. Bailly, P. Lafon, and S. Candel. Stochastic Approach to Noise Modeling for Free Turbulent Flows. *AIAA journal*, 1994.

W.K. Blake. Mechanics of flow-induced sound and vibration. *Academic Press*, II, 1986.

Boermans. *Lecture notes on aircraft aerodynamics*. TU DELFT, 2009.

T.F. Brooks, M.A. Marcolini, and D.S. Pope. Airfoil Self Noise and Prediction. *NASA Reference Publication*, 1989.

Curle, N. The influence of solid boundaries upon aerodynamic sound. *Proceedings of the Royal Society of London*, 1955.

P.A. Davidson. *Turbulence, An introduction for scientists and engineers*. Oxford University Press, fourth edition, 2007.

W. de Roeck. *Hybrid methodologies for the computational aeroacoustic analysis of confined, subsonic flows*. PhD thesis, Katholieke universitiet van Leuven, 2007.

E. de Villiers. *The Potential of Large Eddy Simulation for the Modelling of Wall Bounded Flows*. PhD thesis, University of London, Imperial College, London, 2006.

R. Ewert and W. Schroder. On the simulation of trailing edge noise with a hybrid LES/APE method. *Journal of Sound and Vibration 270*, 2004.

J.E. Ffowcs Williams and D.L. Hawkings. Sound Generated by turbulence and surfaces in arbitrary motion. *Physical Transactions of the Royal Society of London Series A*, 1969.

M.E Goldstein. *Aeroacoustics*. McGraw-Hill Book comapany, 1976.

B. Greschner, J. Grilliat, M.C. Jacob, and F. Thiele. Measurements and wall modeled LES simulation of trailing edge noise caused by a turbulent layer. *Aeroacoustics*, 2010.

W. Haase. *DESider - A European effort on hybrid RANS-LES modelling*. Springer, first edition, 2009.

M. Herr, C. Appel, J. Dierke, and R. Ewert. Trailing-Edge Noise Data Quality Assessment for CAA Validation. *16th AIAA/CEAS Aeroacoustics Conference*, 2010.

M.S. Howe. *Acoustics of Fluid-Structure Interaction*. Cambridge University Press, 1998.

Issa, R.I. Solution of the implicitly discretised fluid flow equations by operator-splitting. *Journal of Computational Physics*, 1986.

H. Jasak. *Error Analysis and estimation in the finite volume method with applications to fluid flows*. PhD thesis, University of London, Imperial College, London, 1996.

Lighthill, M.J. On sound generated aerodynamically. Part I. General theory. *Proceedings of the Royal Society of London*, 1952.

FR Menter, M. Kuntz, and R. Langtry. Ten years of industrial experience with the SST turbulence model. *Turbulence, heat and mass transfer*, 4:625–632, 2003.

NV Nikitin, F. Nicoud, B. Wasistho, KD Squires, and PR Spalart. An approach to wall modeling in large-eddy simulations. *Physics of Fluids*, 12:1629, 2000.

A.A. Oberai, F. Roknaldin, and Hughes T.J.R. Computation of Trailing-Edge Noise due to turbulent flow over an airfoil. *AIAA*, 40(11), 2002.

S. Oerlemans and P. Migliore. Aeroacoustic Wind tunnel tests of wind turbine airfoils. *American Institute of Aeronautics and Astronautics*, 2004.

S. Oerlemans, P. Sijtsma, and B. Mendez Lopez. Location and quantification of noise sources on a wind turbine. *Journal of Sound and Vibration*, 2006.

OpenCFD. User guide openfoam, http://openfoam.com/docs/user, June 2011.

R. Parker and M.C. Welsh. Effects of sound on ow separation from blunt at plates. *Int. J. Heat and Fluid Flow*, 1983.

U. Piomelli, E. Balaras, H. Pasinato, K.D. Squires, and P.R. Spalart. The inner-outer layer interface in large-eddy simulations with wall-layer models. *International Journal of heat and fluid flow*, 24(4):538–550, 2003.

S.W Rienstra and H. Hirschberg. *Introduction to Acoustics*. Eindhoven University of Technology, 2001.

C.J. Roy. Review of code and solution verification procedures for computational simulation. *Journal of Computational Physics*, 2005.

P. Schlatter and Orlu R. Assesment of direct numerical simulation data of turbulent boundary layers. *Journal of Fluid Mechanics*, 2010.

U. Schumann. Subgrid scale model for finite difference simulations of turbulent flows in plane channels and annuli. *J. Comp. Physics*, 1975.

R. E. Sheldahl and P. C. Klimas. Characteristics of Seven Airfoil Sections Through 180 Degrees Angle of Attack for Use in Aerodynamic Analysis of Vertical Axis Wind Turbines. *report SANDIA national laboratories*, 1981.

M.L. Shur, P.R. Spalart, M.K. Strelets, and A.K. Travin. A hybrid rans-les approach with delayed-des and wall-modelled les capabilities. *International Journal of Heat and Fluid Flow*, 29(6):1638–1649, 2008.

Smagorinsky, J. General Circulation Experiments with the Primitive Equations. *Monthly Weather Review*, 1963.

P.R. Spalart. Detached-Eddy Simulation. *Annu. Rev. Fluid Mechanics*, 2009.

P.R Spalart. Young person's guide to detached-eddy simulation grids. *NASA*, CR 2001-211032, 2001.

P.R. Spalart and S.R. Allmaras. A One-Equation Turbulence Model for Aerdynamic Flows. *AIAA*, 1992.

P.R. Spalart, S. Deck, M.L. Shur, K.D. Squires, M.Kh. Strelets, and A. Travin. A new version of detached-eddy simulation, resistant of ambiguous grid densities. *Theor. Computational Fluid Dynamics*, 2006.

C. Wagner, T. Huttl, and P. Sagaut. *Large-Eddy Simulation for Acoustics.* Cambridge University Press, 2007.

Wesseling, P. Principles of Computational Fluid Dynamics. *Springer-Verslag*, 2001.

J. Wijnen. Master thesis in progress on passive turbulent boundary layer suction as a separation control on a wing-flap combination, 2011.

Appendix A

controlDict

```
/*--------------------------------*- C++ -*----------------------------------*\
| =========                 |                                                 |
| \\      /  F ield         | OpenFOAM: The Open Source CFD Toolbox           |
|  \\    /   O peration     | Version:  1.6                                   |
|   \\  /    A nd           | Web:      www.OpenFOAM.org                      |
|    \\/     M anipulation  |                                                 |
\*---------------------------------------------------------------------------*/
FoamFile
{
    version     2.0;
    format      ascii;
    class       dictionary;
    location    "system";
    object      controlDict;
}
// * * * * * * * * * * * * * * * * * * * * * * * * * * * * * * * * * * * * //

application     pisoFoam;

startFrom       latestTime;

startTime       0;

stopAt          endTime;

endTime         0.0901;

deltaT          0.000002;

writeControl    timeStep;

writeInterval   100;

purgeWrite      10;

writeFormat     ascii;

writePrecision  12;

writeCompression compressed;

timeFormat      general;

timePrecision   12;

runTimeModifiable yes;

 functions
{

/*
  forces
  {
    type forces;
    functionObjectLibs ("libforces.so"); //Lib to load
    patches (airfoil); // change to your patch name
    log true
    rhoName rhoInf;
    rhoInf 1; //Reference density for fluid
```

```
    CofR (0.25 0 0); //Origin for moment calculations
    outputControl   timeStep;
    outputInterval  1;
  }
*/

  forceCoeffs
  {
    // rhoInf - reference density
    // CofR - Centre of rotation
    // dragDir - Direction of drag coefficient
    // liftDir - Direction of lift coefficient
    // pitchAxis - Pitching moment axis
    // magUinf - free stream velocity magnitude
    // lRef - reference length
    // Aref - reference area
    type forceCoeffs;
    functionObjectLibs ("libforces.so");
    patches (wall);
    log true
    pName p;
    Uname U;
    rhoName rhoInf;
    rhoInf 1.225;
    magUInf 70;
    CofR (0.25 0 0);
     // liftDir (0 1 0);
    //dragDir (1 0 0);
    liftDir (-0.121869343 0.9925461526 0);
    dragDir (0.9925461526  0.121869343 0);
    pitchAxis (0 0 -1);
    lRef 1;
    Aref 0.1; //0.360555127546; //1.2652171902;  // 0.632534584;

    outputControl   timeStep;
    outputInterval  100;
  }
/*
probes1
    {
        type            probes;
        functionObjectLibs ( "libsampling.so" );
        enabled         true;
        outputControl   timeStep;
        outputInterval  5;
        probeLocations
        (
            ( 0.98 -0.1 0.05 )
            ( 0.98 -0.09 0.05 )
            ( 0.98 -0.08 0.05 )
            ( 0.98 -0.07 0.05 )
            ( 0.98 -0.06 0.05 )
            ( 0.98 -0.05 0.05 )
            ( 0.98 -0.04 0.05)
        ( 0.98 -0.03 0.05)
        ( 0.98 -0.02 0.05)
        ( 0.98 -0.01 0.05)
            ( 0.98 0 0.05)
            ( 0.98 0.01 0.05)
            ( 0.98 0.02 0.05)
            ( 0.98 0.03 0.05)
            ( 0.98 0.04 0.05)
            ( 0.98 0.05 0.05)
        ( 0.98 0.06 0.05)
            ( 0.98 0.07 0.05)
            ( 0.98 0.08 0.05)
            ( 0.98 0.09 0.05)
            ( 0.98 0.1 0.05)
            ( 1 1 0.05)
            ( 1 1.2 0.05)
            ( 1 1.4 0.05)
            ( 1 1.5 0.05)
            ( 1 1.6 0.05)
            ( 1 1.8 0.05)
            ( 1 1.9 0.05)
            ( 1.1 0 0.05)
            ( 1.2 0 0.05)
            ( 1.3 0 0.05)
            ( 1.4 0 0.05)
            ( 1.5 0 0.05)
            ( 2 0 0.05)


    );
        fields
        (
            p
        U
```

```
        );
    }*/
/*
    fieldAverage1
    {
        type            fieldAverage;
        functionObjectLibs ( "libfieldFunctionObjects.so" );
        enabled         true;
        outputControl   outputTime;
        fields
        (
            U
            {
                mean        on;
                prime2Mean  on;
                base        time;
            }

            p
            {
                mean        on;
                prime2Mean  on;
                base        time;
            }
        );
    }
sampledSurface//probes
    {
        type            surfaces;
        functionObjectLibs ("libsampling.so");
        outputControl   timeStep;
        outputInterval  10;
        surfaceFormat   raw;
        surfaces
        (
            airfoil
            {
                type patch;
                patchName   wall;

            }
        );

        fields
        (
            p
        );
    }


*/
}

// ************************************************************************* //
```

Appendix B

fvSchemes

```
/*--------------------------------*- C++ -*----------------------------------*\
| =========                 |                                                 |
| \\      /  F ield         | OpenFOAM: The Open Source CFD Toolbox           |
|  \\    /   O peration     | Version:  1.6                                   |
|   \\  /    A nd           | Web:      www.OpenFOAM.org                      |
|    \\/     M anipulation  |                                                 |
\*---------------------------------------------------------------------------*/
FoamFile
{
    version     2.0;
    format      ascii;
    class       dictionary;
    location    "system";
    object      fvSchemes;
}
// * * * * * * * * * * * * * * * * * * * * * * * * * * * * * * * * * * * * * //

ddtSchemes
{
    default          backward; //Euler ; //steadyState;
    ddt(nut)         Euler;
    ddt(nuTilda)     Euler;
}

gradSchemes
{
    default          Gauss linear;
    grad(p)          Gauss linear;
    grad(U)          Gauss linear;
}

divSchemes
{
    default          none;
    div(phi,U)       Gauss limitedLinearV 1; //Gauss linearUpwindV Gauss linear; //Gauss
         linearUpwindV cellMDLimited Gauss linear 1;
    //div(phi,nuTilda) Gauss linearUpwind Gauss linear;
    //div(phi,U)       Gauss linearUpwind Gauss linear;       // both copied from pitzdaily
    div(phi,nuTilda) Gauss vanLeer; //Gauss limitedLinear 1;
    div((nuEff*dev(grad(U).T()))) Gauss linear;
 div(phi,k)       Gauss limitedLinear 1;
}

laplacianSchemes
{
    default          none;
    laplacian(nuEff,U) Gauss linear corrected; //limited 0.5; //
    laplacian((1|A(U)),p) Gauss linear corrected; //limited 0.5; //
    laplacian(DkEff,k) Gauss linear corrected; //limited 0.5; //
    laplacian(DnuTildaEff,nuTilda) Gauss linear corrected; //limited 0.5; //
    laplacian(1,p)  Gauss linear corrected; //limited 0.5; //
}

interpolationSchemes
{
    default          linear;
    interpolate(U)   linear;
}
```

```
snGradSchemes
{
    default         corrected; //limited 0.5;//
}

fluxRequired
{
    default         no;
    p               ;
}

// ************************************************************************* //
```

Appendix C

fvSolution

```
/*--------------------------------*- C++ -*----------------------------------*\
| =========                 |                                                 |
| \\      /  F ield         | OpenFOAM: The Open Source CFD Toolbox           |
|  \\    /   O peration     | Version:  1.7.1                                 |
|   \\  /    A nd           | Web:      www.OpenFOAM.com                      |
|    \\/     M anipulation  |                                                 |
\*---------------------------------------------------------------------------*/
FoamFile
{
    version     2.0;
    format      ascii;
    class       dictionary;
    location    "system";
    object      fvSolution;
}
// * * * * * * * * * * * * * * * * * * * * * * * * * * * * * * * * * * * * //

solvers
{
  p
    {
        solver          PCG;
        preconditioner
        {
            preconditioner          GAMG;
            tolerance               1e-9;
            relTol                  1e-2;
            nVcycles                2;
            smoother                GaussSeidel;
            nPreSweeps              2;
            nPostSweeps             2;
//            nFinestSweeps           2;
            cacheAgglomeration      off;
            nCellsInCoarsestLevel   480;    // 20 per processor
            agglomerator            faceAreaPair;
            mergeLevels             1;
        }
//        preconditioner  DIC;
        tolerance       1e-9;
        relTol          1e-2;
    minIter     1;
    maxIter     50;
    }

    pFinal
    {
        solver          PCG;
        preconditioner
        {
            preconditioner          GAMG;
            tolerance               1e-8;
            relTol                  1e-2;
            nVcycles                2;
            smoother                GaussSeidel;
            nPreSweeps              2;
            nPostSweeps             2;
//            nFinestSweeps           2;
            cacheAgglomeration      off;
            nCellsInCoarsestLevel   320;
```

```
            agglomerator            faceAreaPair;
            mergeLevels             1;
        }
//        preconditioner  DIC;
        tolerance       1e-08;
        relTol          1e-02;
    minIter     1;
    maxIter     50;
    }

    U
    {
        solver          PBiCG;
        preconditioner  DILU;
        tolerance       1e-9;
        relTol          1e-01;
    minIter     1;
    }

    nuTilda
    {
        solver          PBiCG;
        preconditioner  DILU;
        tolerance       1e-10;
        relTol          1e-01;
    minIter     1;
    }

}

PISO
{
    nCorrectors     2;
    nNonOrthogonalCorrectors 0; //1; // ook naar 0 naar verloop van simlatie
//    pRefPoint         (5 -4 0.05);
    pRefCell        0;
    pRefValue       0;
}
relaxationFactors
{
    default         0;
    p               0.3;
    U               0.4;//0.7
    nuTilda         0.7;
}

// ************************************************************************* //
```

Appendix D

Curle compact formulation code

```
%% LOAD all recorded pressure data of the surface into workspace
d=dir
time_start=double (0.09)            % time when data should be loaded
delta_t=2e-05;
dd=dir();
end_time = str2num(dd(length(d)).name);
nSamples=round((end_time-time_start)/delta_t)
matrix=zeros(32877,1,nSamples);     % number of points on airfoi

count=1
counter2=1
%% Coordinates of surface are loaded
for i=1:1
    file= dd(i+2).name
    str='/p_airfoil.raw';
    numberfile=str2num(file);
    time(count)=numberfile;
        location=[file str];  % col 1-3 are coordinates 4 is pressure data
        A=importdata(location,' ', 2);
        A=A.data;
        coordinates_surface(:,:)=A(:,1:4);
        count=count+1;
end

%% Pressure data is stored in matrix
matrix=zeros(32877,1,nSamples);
count=1
for i=1:nSamples
    file= dd(i+2).name;
    str='/p_airfoil.raw';
    numberfile=str2num(file);
    time(count)=numberfile;
        location=[file str];
        A=importdata(location,' ', 2);
        A=A.data;
        matrix(:,1,count)=A(:,4);
        count=count+1;

end
%% Unit Normals are loaded
% towards interior of airfoil
normals1= importdata('wall_faceAreas.dat',' ');
[normalstest indexnorm]=sortrows(normals1(:,1));
xnorm=normals1(indexnorm,4)
ynorm=normals1(indexnorm,5)
znorm=normals1(indexnorm,6)
%% Rearranging matrices
[B2 index2]=sortrows(coordinates_surface(:,1));
count=1
re_matrix1=zeros(32877,1,nSamples);
for i=1:nSamples
re_matrix1(:,:,count)=(matrix(index2,:,i));
count=count+1;
end
re_matrix=re_matrix1;
%% Compact Curle
% defining some variables
c0=340;
```

```
d=dir;
delta_t=2e-05;
dt=delta_t;
p_ref=2e-05;
radius=[ 10];
theta=90
rho=1.22
x=radius*cos(theta/180*pi)
y=radius*sin(theta/180*pi)
pt_surface=length(re_matrix(:,1));
count2=1
start_time_index=round((start_time-first_time)/delta_t)
end_time_index=length(re_matrix(1,1,:))
dpdt_surface=zeros(pt_surface,3);
Force=zeros(end_time_index-start_time_index,3);


for j= start_time_index:end_time_index

            dpdt_surface(:,1)=squeeze(re_matrix(:,1,j)).*(xnorm(:,1));
            dpdt_surface(:,2)=squeeze(re_matrix(:,1,j)).*(ynorm(:,1));
            dpdt_surface(:,3)=squeeze(re_matrix(:,1,j)).*(znorm(:,1));
    Force(count2,1)=sum(dpdt_surface(:,1));
    Force(count2,2)=sum(dpdt_surface(:,2));
    Force(count2,3)=sum(dpdt_surface(:,3));
    count2=count2+1;
end
deriv=diff(Force,1,1)./dt;
pprime(:,2)=rho/4/pi/c0/radius(o).^2* (x*deriv(:,1)+y*deriv(:,2))
[p15 f15]=oct3bank(pprime(1:end,2))
semilogx(f15,p15,'b+-')
%% Scaling
mach_sim=0.204
delta_sim=0.011
observer_sim=radius
c_sim=1
span_sim=0.1*c_sim
velocity=70
scaled_sim=p15-50*log10(mach_sim)-10*log10(delta_sim)-10*log10(span_sim)...
    +20*log10(observer_sim)
scaledf_sim=f15*delta_sim/velocity
```

Appendix E

Overview Simulation Runs

	Mesh size	cells suction	cells pressure	cells span	cells TE	$Y_{first\,cell}$	Y^+	Δt	physical time interval (acoustic analogy)	number of samples
flat plate	701594	499 (x-dir.)	74 (y-dir.)	19 (z-dir)	-	1E-05	av:0.33/ max:0.96	4E-06	-	-
coarse (0°)	347620	100	75	15	20	4E-06	avg: 0,08 /max 0,16	4E-06	0.10-0.41	7750
medium coarse (0°)	1061760	200	100	25	20	2E-06	avg: 0,04 /max 0,08	4E-06	0.08-0.42	8500
medium fine (0°)	1907060	240	130	35	30	1.5E-06	avg: 0,03 /max 0,06	4E-06	0.08-0.25	4250
fine (0°)	5938800	370	200	50	40	1E-06	avg: 0,01 /max 0,04	2E-06	0.13-0.25	6000
clean (7°)	5938800	370	200	50	40	1E-06	avg: 0,02 /max 0,07	2E-06	0.08-0.18	5000
tripped (7°)	4671576	460	300	40	40	1E-06	avg: 0,14 /max 6,35	2E-06	0.09-0.155	3250
blunt (0°)	3094350	198	148	50	80	1E-06	avg: 0,009 /max 0,02	2E-06	0.19-0.3	5500

Table E.1: Overview of the simulation runs which are discussed during chapter 5 and chapter 6. Grid characteristics and an overview of the acoustic pressure time series are provided.

Appendix F

Tripped and blunt meshes

Tripped Mesh

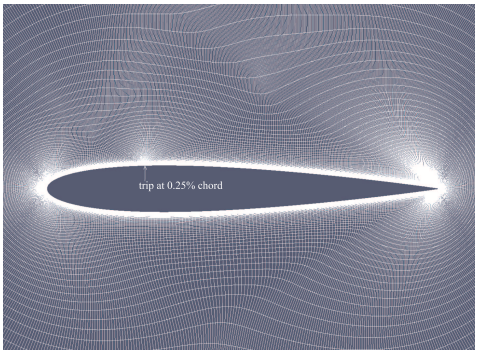

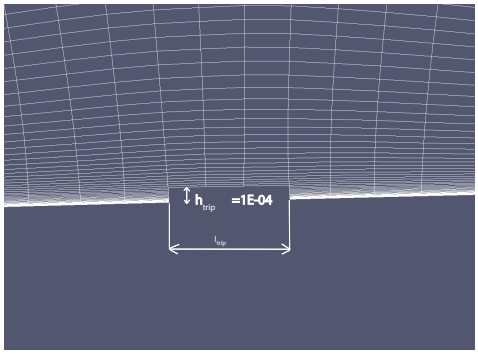

Blunt Mesh

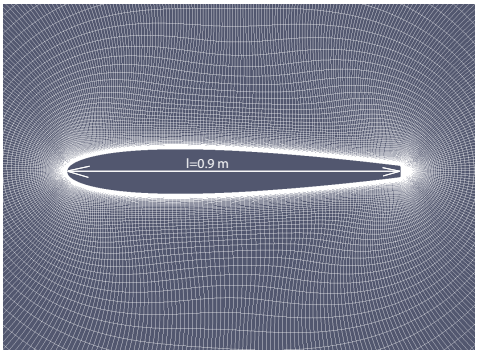

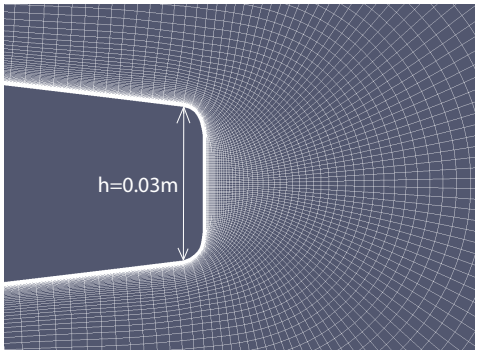

Final page